RICE UNIVERSITY

Adaptive, Intelligent Methods for Real Time Structural Control and Health Monitoring

by

Michael T. Contreras

A Thesis Submitted
in Partial Fulfillment of the
Requirements for the Degree

Doctor of Philosophy

Approved, Thesis Committee:

Satish Nagarajaiah, Chairman
Professor of Civil and Mechanical Engineering

Jamie Padgett
Professor of Civil Engineering

Richard Tapia, University Professor
Professor of Computational and Applied Mathematics

Andrew Meade
Professor of Mechanical Engineering and Material Science

Houston, Texas

August, 2010

ABSTRACT

Adaptive, Intelligent Methods for Real Time Structural Control and Health Monitoring

by

Michael T. Contreras

By framing the structural health monitoring and control problem as being one of enhancing structural system intelligence, novel solutions can be achieved through applications of computational strategies that mimic human learning and attempt to replicate human response to sensory feedback. This thesis proposes several new methods which promote adaptive, intelligent decision making by structural systems relying on sensory feedback and actuator compensation. Four significant contributions can be found in this thesis study. The first method employs an adaptable subclass of Artificial Neural Networks (ANNs), called Radial Basis Function Networks (RBFNs) for robust control in the presence of sensory failure. The second method exploits this computationally efficient network to detect and isolate system faults in real time. The third algorithm utilizes an RBFN to effectively linearize the nonlinear actuator

dynamics of a Magnetorheological (MR) damper, thereby improving control of the semiactive device. Lastly, an open loop observer is implemented experimentally to both detect damage and act as a trigger for control of the newly developed Adaptive Length Pendulum-Smart Tuned Mass Damper (ALP-STMD).

Some limitation of existing algorithms in the field of real time structural health monitoring and control are that they rely heavily on fixed parameter methods, assume standard linear time invariant assumptions, or mandate accurate modeling of system dynamics. By embedding the proposed reasoning and decision making algorithms into the feedback methodology and design, greater generalization and system adaptivity is possible. Specifically, the proposed methods develop novel solutions for adaptive neural control, fault (sensor failure) tolerant control, real time damage detection, adaptive dynamic inversion, and control applications for STMDs.

The neural network adaptive control formulation is successful in rejecting first mode disturbances despite online sensor failure. It is also capable of improving the performance of a baseline H_∞ controller in the presence of sensor failure and earthquake ground motion. The proposed fault tolerant controller is validated on a two degree of freedom shear frame subjected to six earthquake records. Furthermore, this application involves the use of piezoelectric patches as sensors and actuators.

The RBFN algorithm in combination with an open loop observer is capable of both detecting and isolating stiffness degradation and recovery in multi-degree of freedom systems in real time. The method is validated on experimental data taken from online

damage tests using the Semi-Active Independent Variable Stiffness (SAIVS) device. Other validations involve simulations on a two degree of freedom system and a ten degree of freedom system with both independent and coupled damage case scenarios. In all scenarios, the RBFN is capable of identifying the length of time and degree of freedom in which stiffness variation occurred.

A neural network formulation is developed to perform dynamic inversion for semi-active control of an MR damper. The MR damper acts as a base isolator in a scaled two story building. Both the building and damper models were based on tests performed at Rice University. The control performance of the adaptive RBFN dynamic inversion method is compared to both passive-off and passive-on methods of semiactive control for MR dampers.

The last contribution serves to combine both real time structural health monitoring and control in a proof of concept experimental study. An open loop observer is used to trigger an ALP-STMD device in the presence of base excitation and stiffness damage. The stiffness damage is generated from strategically regulating the current applied to Shape Memory Alloy (SMA) braces in a two degree of freedom shear frame. Once damage exceeds a predefined threshold, the ALP-STMD uses a another SMA to adjust its pendulum length to tune in real time to the dominant pulse present in the base excitation.

Acknowledgments

I would like to express my sincere gratitude to my advisor Dr. Satish Nagarajaiah. Prof. Nagarajaiah has been a mentor in all aspects of life, and I thank him for his direction and guidance throughout my Ph.D. studies. He has always believed in me from day one, even in times of self doubt. He has always been an unwavering advocate and a catalyst for the research in this thesis. With his help and support I have enjoyed a myriad of international opportunities very early in my research career. I am indebted to him for his guidance and keen interest in developing the research in this dissertation. I have enjoyed our countless hours of interaction that has helped me mature as a researcher and teacher.

I would also like to thank Prof. Richard Tapia for being one of the greatest examples of a civic scientist. His career path is truly exemplary and worthy of aspiration. I would like to express my thanks to Prof. Andrew Meade for initiating the Co-Op program that I had the opportunity of participating in during my final year of studies at Rice. Additionally, I am grateful to Prof. Jamie Padgett for being a positive influence on my desire to pursue a faculty career.

I have had the pleasure of working in a research group that is sincerely collaborative in nature and shares a bond beyond being simply colleagues. I learned so

much from Dharma Theja, Vishnu Mohan, Chaojun Huang, and Chao Sun. I am grateful for their attentive ears and kind suggestions. Their companionship will truly be missed.

My thesis has been enriched by my interaction with Prof. Sriram Narasimhan, Dr. Bilei Chen, Dr. Ertan Sonmez, and Dr. Sanjay Sahasrabudhe. Although graduated, they took the time out of their busy professional lives to offer advice, suggestions, and sound reviews of my work. I would especially like to thank Prof. Narasimhan for his early help in neural network research.

Finally, I would like to thank my wife, Alison. I have experienced no greater happiness than our marriage together, and she gives me endless strength to be a great researcher, husband, and friend.

Contents

Illustrations

Tables

Chapter 1

INTRODUCTION

1.1 Objective and Scope of This Study

In recent years, the research community across all disciplines has enjoyed greater computational resources than at any other moment in history. Investigators have been able to scale down technology (in some cases to the nanoscale) without fully sacrificing computational power and/or accuracy. These advancements have provided an abundance of integrated sensing and actuation technologies that has become part of everyday life. With the wealth of information, researchers are again looking to biology to inspire the future direction of innovation. Ideas once thought infeasible due to the scarcity of real time data acquisition and the means to process this data are now becoming a reality.

Civil engineering has not been left out of the computational revolution. Out of the desire to prevent engineering disasters and address the aging civil infrastructure, structures are being instrumented with distributed sensors and actuator technologies. Similar to the human body, smart structures are capable of adapting to their environment given sensor feedback. How to make the decisions that govern the inputs to the adaptive process has been a major focus of structural control and health monitoring.

In effect, generating intelligent algorithms for structural smart systems makes them more robust to their environment and safer throughout their design life.

Artificial Neural Networks (ANNs) have proven very efficient in many engineering applications such as function approximation, pattern classification, and control. They were created to mimic the biological neural pathways that enable human learning. Neural networks perform well in a variety of complex problems with the ability to adapt and continually improve performance through learning. Many of the adaptive algorithms proposed in this thesis are based on Radial Basis Function (RBF) neural networks and use resource allocation techniques. The RBF networks are extremely fast and require fewer training samples when compared to other ANN methods such as back propagation. The computational speed combined with accuracy makes these networks extremely well suited for real time applications.

The scope of this study includes the development of fault tolerant controllers, adaptive structural health monitoring strategies for time varying systems, linearization techniques for smart systems, and other topics which are inspired by the adaptive nature of the aforementioned RBF networks. The theories are applied to specific problems and validated by experimental verifications.

The subsequent literature review encompasses material essential for background and theoretical development of the proposed formulations in this thesis. The selected topics in structural control and Structural Health Monitoring are indicative of current research and provide a foundation on which the formulations in this thesis are based.

1.2 Review of Related Structural Control Work

The following are active areas of controls research in smarts structures technology. At the mathematical level, structural control in civil engineering lends itself to a multi-disciplinary approach. The overlapping control themes and parallels to aerospace, electrical, and mechanical engineering are plentiful. In most cases, the feedback methodologies will be identical excepting the system representation of the plant.

1.2.1 Robust Control

Robust control designs a feedback system for the worst case scenario. In systems with the highest levels of uncertainty, robust control seeks to produce the feedback gains that produce a the best level of performance according to some metric: the H_∞ norm is one such metric. It is the ratio of the energy (L_2) norm of the output over the energy (L_2) norm of the input. H_∞ robust control selects the optimal feedback gains such that for a given input, the energy input to the system is minimal. In short, the designer is trying maximize the efficiency of the response by minimizing the system's energy output in a root mean squared sense for an uncertain plant and input (Doyle [1]). Linear Matrix Inequality representation of the H_∞ norm has made robust control design intuitive and suitable for general optimization strategies (Skelton *et al.* [2]).

1.2.2 Intelligent Control

Intelligent control comprises the areas of fuzzy logic and/or neural networks. These methods show great promise in control applications due to their ability to model nonlinear systems, adapt to a wide variance of input, and minimize error functions. There are many applications of intelligent control in the literature; however, few implement these techniques in real time. Both Masri *et al.* [3] and Ghaboussi *et al.* [4] have published extensively on civil engineering applications of neural networks.

1.2.3 Adaptive Control

Adaptive control is the implementation of a time varying controller. The need for time varying controllers may arise from the desire to control harshly nonlinear systems, unstructured input uncertainty, systems with parametric time variation, etc. Many times, controllers cease to perform well when the nominal system for which they were designed for begins to vary with time. Thus, the necessity for an adaptive controller arises to ensure performance. The manner in which the controller evolves in time so as to ensure a desired performance is the problem that adaptive control seeks to solve.

1.2.4 Fault Tolerant Control

Fault tolerant control is a specific subset of adaptive control that deals with compensating for unintended performance of actuators and/or sensors. This problem is

especially relevant for large scale structural systems in which many distributed sensors and actuators are used. Narasimhan *et al.* have proposed a fault tolerant controller and demonstrated its performance for applications involving building structures excited by earthquake ground motions [5] [6]. With respect to piezoelectric applications involving actuator failure, Wang [7] has shown the ability to perform active vibration attenuation on a rocket fairing system using Positive Position Feedback (PPF) control in the presence of online actuator failures.

1.3 Brief Overview of Smart Materials

In an effort to produce integrated smart structural systems, research directions have moved toward the application and development of multifunctional materials. Smart materials can be embedded directly into structures while still maintaining their sensor and actuator capabilities. In structural systems where payload weight drives the overall design and cost, smart materials pose the greatest benefit due to their multifunctional capabilities. Smart materials have also been applied in large scale civil structures as well because their embedded nature can provide structural stability while being aesthetically pleasing. Their implementation can also reduce the weight and size of the civil structure's members, thereby lowering labor and material cost dramatically.

1.3.1 Piezoelectric (PZT) Patches

Song *et al.* [8] have had success in performing active vibration suppression on scaled shear frames using piezoelectric patch actuators and sensors and a state feedback pole placement controller coupled with a state estimator. Favorable results have also been produced with larger scale models in which Kamada *et al.* [9] have used piezoelectric stack actuators to induce bending moment control in the columns of a four-story structural frame, 3.7 m in height and 2000 kg in total weight.

1.3.2 Shape Memory Alloys (SMAs)

The general shape memory phenomenon is the reason behind the excellent damping properties of SMA wires. However, general shape memory effects are difficult to model because many mechanical properties such as yield strength and modulus are very strongly temperature and load path dependent (Duerig and Melton [10]). The sensitivity to temperature is a result of a phase change that occurs when the SMAs crystalline structure changes from martensite (the low temperature phase) to austenite (the high temperature phase). The general trend is counter intuitive with respect to most metals and behaves as follows: at cold temperatures, the SMA develops a twinned martensite crystalline configuration and can undergo large deformations, but as heat is applied it can generally contract and recover its original shape.

There has been a significant amount of work done with Nickel Titanium (NiTi) SMA wires with respect to their superelastic behavior. Humbeeck and Kustov have

shown that as long as the strain amplitude is within a certain reorientation level (below 5%) little hardening occurs and large energy absorption can be realized due to the hysteretic behavior of the SMA wire [11]. The damping capacity or energy storing capability of SMA wires is amplitude dependent. For this reason, SMA wires are suitable for passive damping in high amplitude vibrations such as earthquakes or impact loadings in which higher strain amplitudes are obtained.

1.3.3 Magnetorheological (MR) Dampers

MR dampers achieve their adaptive capabilities due to micron-sized, magnetically charged particles which are dispersed in the oil of a fluid damper. By subjecting the MR fluid to changes in the magnetic field the effective viscosity of the damper oil can be modified due to alignments in the charged MR particles. In the absence of a magnetic field, the MR fluid has low viscosity while in the presence of a magnetic field, the oil increase in viscosity and flow similar to a semi-solid. Material testing of the resistance of the MR fluid itself yields maximum yield stresses of approximately $50 - 100$ kPa [12].

MR dampers have been utilized for seismic response control in several applications for which MR dampers models were generated by Spencer *et al.* [13] and Dyke *et al.* [14]. The material models were generated to exhibit damper behavior similar to that of a Coulomb friction element in parallel with a linear viscous dashpot. If the force exceeds a threshold value, the damper force output saturates. Subsequently,

an MR model behavior that is characterized by the Coulomb friction behavior and the force threshold condition was incorporated by the Bingham viscoplastic model. Finally, a more general model was developed consisting of an arrangement of linear springs, linear viscous dashpots, and a Bouc-Wen hysteresis element. The Bouc-Wen hysteresis MR damper model has become widely accepted as an accurate analytic tool for experimental modeling.

Regarding full scale implementation, several large-scale MR damper have been developed and implemented by Spencer *et al.* [12] for seismic response control. Experimental tests to model and characterize the dynamic behavior of the full-scale dampers have been performed as well. Early implementation involved shaking table tests performed by Dyke *et al.* on a reduced-scale three-story steel structure subjected to earthquake ground motion. The steel structure had a single MR damper located in the first story which was governed by a semiactive control algorithm [15] [16]. The MR damper used in the shaking table tests implemented the analytical model developed by Spencer *et al.* [13]. In the same study, a clipped-optimal control algorithm was applied to semiactively control the MR damper based on acceleration feedback. The structure was also used to produce comparison data for a semiactive control system and two different passive control systems. In general, the disturbance rejection of the structure with the semiactive control system was better than the performance of the structure with a passive control system while producing smaller control forces. Furthermore, it was noted that the further improvement in control performance could

be achieved by developing control algorithms which directly account for the actuator dynamics and control-structure interaction.

1.4 Disturbance Rejection Methods for Smart Structural Systems

Significant attention has been given to the problem of minimizing structural response in the presence of input disturbance to a civil structure. Some of these disturbance events include blasts, earthquakes, wind excitation, etc. Actuator and sensor instrumentation render this type of structure possible. There are several methods of implementation based on feedback control

1.4.1 Active Control Actuators

In order to generate the magnitude of input necessary to control large scale structures, electrohydraulic or electromechanical force actuators apply input to the system based on measured sensor feedback at particular locations in the structure. Sensor placement and feedback design depend on the performance goals of the designed controller and the input excitation. Since energy is actually being input into the system, it is imperative that the selected feedback control algorithm be closed loop stable [17].

Buildings in Japan and China have seen full scale implementation of actively controlled mass dampers [18]. The generation of control forces by electrohydraulic actuators requires large power sources that may reach several megawatts for large

structures [19]. Soong *et al.* [20] [21] [22] and Fujino *et al.* [23] provide a comprehensive overview of active structural control.

1.4.2 Passive Devices

Passive controllers require no power source and are strictly passive and dissipate energy by passive damping mechanisms. Passive control systems operate in a manner similar to the way a passive shock absorber maintains a smooth ride for the passengers of a moving vehicle. They come in variety of forms including the yielding of soft steel, viscoelastic behavior in rubber-like materials, viscous fluid flow through an orifice, and sliding friction mechanisms. The passive resistance system may be distributed throughout the structure at specific points and/or it may located at the base of the system. Base isolated systems benefit from the increase in flexibility between the foundation and the superstructure. The isolators dissipate energy and reduce the structure's peak and root mean square accelerations [24]. Whether distributed or base isolated, the passive system reduces the demand on the structural system by absorbing a significant amount of the disturbance energy [25].

1.4.3 Semiactive Control Devices

Semiactive devices combine the desirable features of both passive and active control systems. Due to their relatively low energy consumption and inherent closed loop bounded stability they offer a viable means of protecting civil engineering structural systems against input disturbances. As energy efficiency has become a major research

motivation in all fields, semiactive devices have received increased attention. Their power consumption is minimal and many devices can operate via battery power, a critical advantage for extreme events in which external power sources may be unreliable.

According to Spencer and Sain, a semiactive control device is one which does not inject mechanical energy into the controlled structural system; however, the device itself has properties that can be modified according to sensor feedback such that the responses of the system are sufficiently reduced [26]. Studies indicate that semiactive systems perform better than passive devices, and their performance rivals that of fully active systems in the presence of wideband dynamic loading conditions [18] [26] [27]. Some examples of semiactive devices devices that have been applied in practice include variable-orifice fluid dampers, variable-stiffness devices, controllable friction devices, smart tuned mass dampers, tuned liquid dampers, controllable fluid dampers, and controllable impact dampers [18]. A special discussion of tuned mass dampers will follow due to their relevance to this thesis.

In recent years, significant attention has been dedicated to studying the effectiveness of Tuned Mass Dampers (TMDs) and multiple tuned mass dampers (MTMD). A TMD is a semiactive device that inherently dissipates energy from a structural system because its material properties correspond to dominant frequencies in a structural system's response. TMDs are analogous to a low frequency "tuning fork" that harmonically resonate when a structural systems modes are excited. As such, TMDs

are very sensitive their frequency tuning ratio even when designed properly. Also, a single TMD which has fixed material properties is only capable of dissipating energy for single dominant frequency of system response. The MTMD overcomes this limitation; however, the MTMD cannot be applied to time varying systems with damage or faults because they cannot be adaptively tuned in real time. In an effort to make TMDs and MTMDs more robust, TMDs with adjustable damping were first examined by Hrovat *et al.* [28].

The work of Hrovat led to the development of a several novel Semiactive Tuned Mass Damper (STMD) which all share the distinct advantage of continuously retuning their frequency parameters in real time, thus making them robust to changes in building stiffness and damping. Nagarajaiah and Varadarajan [29] developed a STMD that was able perform real time tuning through implementation of the Semi-Active Independent Variable Stiffness (SAIVS) device to vary the stiffness parameter of the STMD [Nagarajaiah, U.S. Patent No. 6,098,969]. The patented system has been demonstrated both analytically and experimentally on a small-scale three story structural model. The variation of stiffness of the STMD is made possible by an estimation of instantaneous frequency and a time frequency controller also developed by Nagarajaiah and Varadarajan [29]. Varadarajan and Nagarajaiah have also illustrated the power saving advantages of the STMD device by examining a tall benchmark building in which response reductions achieved were comparable to an active tuned mass damper while consuming considerably less power [30].

Analytical studies on STMDs with variable damping have been performed Abe and Igusa [31]. Experimentally, their have been several additional applications of semiactive technologies. Semiactive impact dampers were developed by Caughey and Karyeaclis [32] and shown to be effective experimentally. Controllable Tuned Sloshing Dampers (CTSD), and Controllable Tuned Liquid Column Dampers (CTLCD) have also been proposed and are implemented in full scale applications. Lou *et al.* proposed a CTSD device which extend a passive TSD in which the length of a sloshing tank can be modified, thus increasing the adaptivity of the device [33]. Also, Abe *et al.* [31] and Yalla *et al.* [34] have developed a semiactive CTLCD device based on a TLCD with an added variable orifice for increased robustness.

Finally, there have been several successful full scale implementations of Adaptive Passive Tuned Mass Dampers (APTMD). APTMDs possess the adaptability of an STMD; however, their adaptation is performed off line usually through adjustments in geometric configuration. They have been successfully implemented in the Citicorp center building (New York City) through the use of nitrogen springs [35] , and the Tokyo Towers through the use of an adaptive radius configuration [36] . An Adaptive Length Pendulum is a particular type of APTMD that is conceptualized to have a swinging mass system whose length can be adjusted to obtain enhanced performance. The aforementioned TMD methodologies lay the foundation for development of the ALP-STMD which will be discussed in further detail in Ch. 6.

1.5 Review of Related Structural Health Monitoring Work

In order to prevent engineering failures and safeguard against operational inconsistencies, the field of Structural Health Monitoring (SHM) proposes monitoring the structural integrity of pivotal locations within a structural system. The merits of such a task are best explained by a short example. Within the aerospace industry, small impacts can cause delamination of composite fibers that can result in an abrupt and catastrophic loss of structural integrity. However, detecting these small cracks is difficult because they cannot be seen with the naked eye. Current methods of crack detection require that the plane be grounded and temporarily out of service which can be very costly for stakeholders. If possible, these monitoring tests should be done during the operational life of the structure and without actually inducing permanent damage to ensure that the structure can remain in service. These are the main goals that drive continued investigation into the field of structural damage detection.

The need to monitor system characteristics and the onset of damage for critical structural and aerospace systems, combined with the ability to collect, transmit and process large quantities of data has precipitated extensive research in the field of SHM. In the early research stages, it was a sufficient goal to simply locate damage within a reasonable accuracy using non-destructive techniques. Rytter has broadly categorized damage identification into four levels and served to both define and push forward the basic goals of the research field: Level 1 - determination that damage is present in a structure; Level 2 - determination of the geometric location of the damage; Level 3 -

quantification of the severity of the damage; and Level 4 - prediction of the remaining service life of the structure [37]. At the present time in the damage/fault detection field, there is an increasing need to not only be able to perform these prerequisite tasks, but to do them in real time. In this case, real time signifies a time period parallel to the change or degradation of the structural properties due to unknown damage.

A majority of current research in the area of SHM and damage detection can be broadly grouped into the limit checking methods and physical/analytical redundancy methods. The *limit checking* process involves comparing the present status of the plant system with preset limits that are manually set. The presence of failure or damage is indicated by the measurement variable exceeding the threshold or limit state. Although the method is straightforward, the limit checking process is difficult to implement because the plant variables may vary widely due to normal input parameters. In this respect, it is difficult to determine the appropriate threshold values without being overly conservative. Also, pinpointing the geometric location of the damage is difficult because damage in a single element may affect many other plant variables thereby disguising the origin of the damage.

The *physical/analytical* redundancy methods for damage detection involve the same logical methodology; however, physical redundancy is used for sensor/actuator failure detection and analytical redundancy is can be used for all fault detection. The physical redundancy method basically places duplicate sensor/actuator hardware at

the critical locations/nodes on a structure. Any discrepancies between sensor measurements or actuator performance triggers some type of decision making scheme to determine if in fact there is a failure. This method becomes obsolete as structures increase in size and complexity of sensor/actuator arrangements. The analytical redundancy method has been extremely popular for the last two decades. A residual signal is generated by comparing the measured signal and the estimated signal generated from a healthy system, usually achieved from an analytical model. After being filtered and analyzed, the residual can be an indicator of damage or a fault in the structural system. Generating a plausible model of a "healthy" system when the structure starts to have many degrees of freedom and possesses high nonlinearity is not straightforward.

1.5.1 Time Domain Methods

Because the methods proposed in this thesis are valid in the time domain (as opposed to the wavelet methods of Basu *et al.* and Nagarajaiah *et al.* [38] [39]) it is necessary to highlight recent work in this area and its wide variety of applications. Real time SHM inherently lends itself toward time domain methods, or in other words making assessments at discrete time intervals. It is different from traditional modal-based diagnostic methods which record large sums of data and then makes offline evaluations of structural integrity. It also produces more readily available results than the intermittent inspection method which is widely used for infrastructure health as-

sessments in the United States. The benefits to implementing real time methods as opposed to offline methods is evidenced by attaining earlier knowledge of imminent failure. Using this information a variety of actions can be taken to mitigate or prevent catastrophic failure and reduce economic loss. The most obvious asset to real time methods is the use of feedback actuation in smart structures to correct, stabilize, or compensate for the losses in structural integrity. Time domain methods have already found applications in aerospace structures, rotating machineries, feedback controlled buildings, national defense, etc.

Recently, significant advancements have been achieved by Dharap *et al.* [40] and Koh *et al.* [41] who have performed real time health monitoring with experimental validations on a NASA eight bay truss structure. Using data from tests involving the SAIVS device, Chen *et al.* were able to detect real time stiffness variation using an iterative linear matrix inequality approach [42] and a eigen structure assignment method [43] respectively. Finally, regarding real time detection of changes in mass and/or stiffness in MDOF and SDOF systems, Koh *et al.* have been successful in implementing a Kronecker Product (KP) method [44].

Real Time Redundancy Based Methods

One family of time domain SHM methods that deserves further exposition because of its relevance to this thesis is the family of real time redundancy based methods. Due to their large requisite computational loads that must occur in real time, most methods

simplify the overall problem and specifically target a particular type of fault or failure to detect. Instrument Fault Detection (IFD) primarily examines the functioning of sensors in a system. Actuator Fault Detection (AFD) monitors the proper operation of all system actuators. Recent work by Koh *et al.* [45] and Li *et al.* [46] have verified real time redundancy based algorithms for both detection of sensor and actuator failure for space truss structures. Lastly, there is Component Fault Detection (CFD) which targets the health of the structural members of the system. Many popular CFD methods, including a methodology proposed in Ch. 6, use a model-based redundancy strategy for signal-based diagnosis in the time domain.

Real time redundancy methods can be further categorized into real time physical redundancy strategies and real time analytical redundancy strategies. Several physical redundancy approaches to SHM have implemented algorithms based on majority voting logic in which a system is equipped with triplicate sensor or actuator redundancy. When a sensor or actuator fails it can be determined unfit from the condition of remaining sets. Of course, this method has serious cost disadvantages as the number of actuators and sensors grows. In order to address this setback, analytical redundancy based strategies were developed in which sensor, actuator, and/or system models are generated to provide online healthy baseline comparisons. These baseline comparisons are often called parity relations and are used to detect, locate, and quantify failures within a structural system. The credibility of the parity relations are often disrupted by several factors: system uncertainty, unmodeled dynamics,

and measurement noise in the input-output data. Often, it is difficult to distinguish with parity based methods between what is a system fault and what is system noise. The main motivation of any real time analytical redundancy strategy is to create a detection scheme that is less sensitive to model errors/system noise and very sensitive to the effects of failures. One particular way to do this is discussed in the following section.

Real Time Filter Based Methods

Because system faults inherently modify dynamics, and in turn the system's time domain response, structural damage detection filters have been applied to observe system changes buried within system output signals. These changes contribute to an error residual which can be produced by a filter that signifies that a fault has occurred. Early attempts at designing such a filter were primarily targeted at detecting failure among the sensors, actuators and structural members. These filters accounted for system uncertainties and noise corrupted measurements while remaining robust with respect to fault detection.

Early theoretical development was done by Beard and Jones in which they implemented model based observers as failure detection filters [47] [48]. With proper choice of filter feedback gains, these first order model based observers produced outputs which could identify and locate system component failures of a closed loop system. A matrix algebra approach was later implemented by Beard [47] and Jones [48]

continued in the direction of a geometrical approach. At this stage, much of their work targeted control system component failure.

It wasn't until the second order version of Beard's failure detection filter was developed by Kranock [49] that analytical redundancy strategies would be applied for structural damage detection. Kranock treated forces resulting from structural damage as inputs to the system and filter output indicated the damage as well as the location of damage in real time. Liberatore *et al.* [50] furthered this work through application by using a fault detection filter to monitor the health of a simply supported beam and pinpoint locations of the failure. In Liberatore's study, fault direction vectors describing predefined damage locations in the structure provided the basis for identification for each of the possible fault locations.

Because the early development of fault detection filter based methods was rooted in control system methodology, the Kalman filter played an important role in the localization and quantification extensions. Because the Kalman filter is an optimal state estimator, given a known model of the system under the influence of some process and measurement noise with known statistics specified in terms of their covariance, it provides a robust model of more complex systems for parity based methods. A filter based method to detect small cracks in a rotor dynamic system was developed by Seibold *et al.* [51] and applied estimation techniques based on a Kalman filter bank. In this filter bank approach, each filter represents a specific crack damage scenario, and by analyzing the whiteness or innovation of the estimation residual the crack

is localized. In a subsequent study, Seibold applied the extended Kalman filter approach with a recursive instrumental variables technique to detect the crack growth in a rotor by merely sensing the measured displacement of the disc [52].

1.5.2 ANN Offline SHM Methods

To date, a majority of applications of ANNs for structural damage detection have been performed offline and for a wide variety of civil systems, both theoretical and experimental. These studies are primarily utilizing the ANN capability for pattern recognition. This purpose has a direct effect on the architecture and learning methodologies implemented by researchers. The design of generic ANN capable of pattern recognition requires the determination of the specific number of nodes and a fixed number of layers comprised of these nodes. Each node of the network is a local processing element capable of a generic function evaluation (defined by the architect) of a weighted input summation that is summed in a way determined by a network topology. Information is passed from one input layer to the subsequent output layer by a series of function evaluations and weighted connections until the final output layer is reached. Biases are often used in the initial input layer to shift the input as desired and help with convergence. More details on ANNs will be elucidated in the following chapter; however, this exposition is given to illustrate the network design decisions that are inherent in selecting a suitable ANN given the SHM objective.

Once the ANN methodology is selected the weights and biases must be deter-

mined so that the ANN can properly recognize healthy data apart from damaged data. This is done in most studies through offline training. It is clear regarding the training that selection of damage parameters, damage scenarios, and a robust system identification are critical for the success. Given the predefined fixed set of weights in the ANN, it is often challenging to acutely map a system's dynamic characteristics in a convenient, unique relationship from input to output. Often these fixed mappings are overdetermined, underdetermined, or grossly computationally expensive non-parametric mappings of input to output. Through the use of extensive offline training, correlation between the change in ANN output to the damage location and level of damage can be obtained. However, it is clear that these successes will be limited by network selection, memory capacity, and availability of training data sets.

Earlier work by Feng and Bahng [53] has used a back propagation neural network with two hidden layers to estimate changes in system stiffness based on measured vibrations of composite reinforced concrete columns. Modal data was used as an input to the neural network and correction coefficients in the stiffness matrix as an output of the neural network to determine both the extent and location of damage in a half scale laboratory model. Moving toward time domain applications, Zhang *et al.* [54] used a multilayer perceptron trained using an error back-propagation algorithm to detect the damaged state in several locations in a both a truss structure and a three story structure. This method is particularly interesting because it implemented independent component analysis on the input time domain vibration data to simplify

the complexity of the network design and consequently output robust results in less computational time. The only drawback is that the independent component analysis step also requires computational resources and complicates the training process.

Full scale applications for offline damage detection methods have been challenging due to the increase in damage scenarios, vibration data, and degrees of freedom. In a study by Zapico *et al.* [55], multilayer perceptrons with the back propagation error algorithm update were used to assess damage in a full scale steel structure with composite slab decks. The training data for this complex system was generated analytically from a simplified finite element model. Damage scenarios were produced at random by simulating this finite element model under a variety of damaged beam conditions. By using only natural frequencies and mode shapes for input, the method was able to detect the extent of floor damage when tested on experimental data. However, the method was not able to detect section or bar damage given the simplified training procedure.

Finally to illustrate the agility of ANNs for a variety of applications, Masri *et al.* [3] have applied neural networks for detection of changes and high fidelity modeling of nonlinear systems. In the study, the authors have used a feedforward ANN with two hidden layers to model a Duffing oscillator in the presence of stochastic excitation of differing magnitude. They presented only error statistics of the ANN error output in this proof of concept study.

Chapter 2

NEURAL NETWORK COMPUTING STRATEGY

This chapter lays the groundwork for understanding the fundamentals and advantages of implementing an Artificial Neural Network (ANN) for structural control and monitoring applications. First, background information on Radial Basis Function (RBF) networks is presented to inform the reader of the particular class of ANNs that has been chosen. In this study, the learning rule and resource allocations techniques are presented in great detail so as to remove any presumptions of a 'black box' method. Finally, the optimal selection of the network's initialization parameters is discussed.

2.1 Background on Radial Basis Function Networks

RBF networks are extremely fast and require relatively small training data sets compared to other neural network methods such as back propagation. They are also less susceptible to problems with non-stationary inputs because of the behavior of the radial basis function hidden units. This makes RBF methods very attractive for real time structural health monitoring and damage detection. The motivation behind the development of RBF networks is biological organisms and processes where the output of neurons is local or tuned to some region of the input space. Basically, the

hidden layer consists of the locally tuned or locally sensitive neurons, and the output layer consists of linear units. In hidden-layer neurons, the neuron response (output) is localized and decreases as a function of the distance of inputs from the neuron's receptive field center. Commonly used basis functions for the hidden layer are Gaussian, multi-quadratic, inverse multi-quadratic and thin-plate spline functions. The output is a linear combination of the hidden layer outputs. The linear weights associated with the output neuron of the network tend to evolve on a different time scale compared with the nonlinear activation functions of the hidden layer neurons. Hence, different layers of an RBF network perform different tasks, and it is reasonable to separate the optimization of the hidden layer and the output layer by using different techniques. Based on this idea, the training of the RBF is usually done using a two-step procedure; the RBF parameters are determined in the first step, and the weights are estimated using algorithms such as linear least square estimation, with the objective to minimize the difference between the desired output and the actual output of the RBF network. There are several methods to determine centers of the RBF with varying degrees of computational efficiencies.

2.2 RBF Network Applications

Yakuwa *et. al* [56], have applied nonlinear RBFN neural networks and time delay neural networks to perform fault detections on automobile transmission gears. Using a time history of acoustic data compiled by a Japanese automobile manufacturer, the

structural RBFN parameters were obtained and the appropriate number of Gaussian basis functions was determined. Using this algorithm the damage to the transmission gears was identified successfully.

Suresh *et. al* [57], have used a combination of Multi Layer Perceptron (MLP) and RBF neural networks to identify both the location and the depth of a crack in a cantilever beam. In order to train the networks, a fracture mechanics based model for a cracked cantilever beam was used. In the combined approach, one neural network was used for estimation of crack location while the other for estimating crack depth. Both networks were used to perform each function. The results of the study demonstrated that the RBF network performs better than the MLP network because the training time was found to be less, and it could be implemented on-line.

With respect to damage detection and dynamic systems, Reddy *et. al* [58], have presented a neural network approach for identifying faults in a helicopter rotor blades using rotating frequencies of the flap (transverse bending), lag (in-plane bending), elastic torsion, and axial modes. A finite element model was generated for the helicopter blade and was used to train the neural network. The study was carried out using the first ten modes of the rotor blade and yielded accurate results for detecting damage.

2.3 Network Resource Allocation for RBF Approximaters

Platt [59] developed a sequential learning algorithm, called the Resource Allocation Network (RAN). In this algorithm, the number of hidden neurons is a function of the complexity of the problem and a new hidden neuron is added if the new data exhibits novelty, as defined by certain conditions. When the novelty conditions are not satisfied, the network parameters are adjusted using a LMS algorithm. This algorithm results in a compact network compared to fixed-size networks, and learns quickly for real-time applications. Kadirkamanathan and Niranjan [60] found that the adaptation of network parameters by LMS in RAN was a weak step. They suggested using an Extended Kalman Filter (EKF) instead of LMS and showed through several examples that the resulting network, RANEKF was even more compact than RAN.

The first RBF network introduced by Powell [61] is a problem of exact interpolation. In exact interpolation, every input vector has to be mapped exactly to a corresponding output vector. However, this method of exact interpolation leads to over-determination and high computational costs. Subsequent works on RBFs, such as one proposed by Broomhead and Lowe [62] and Moody and Darken [63] have addressed some of the issues mentioned earlier. However, in these methods the number of hidden neurons must be decided a priori and problems involving real time applications such as structural health monitoring. In EKF and RANEKF methods, once a hidden neuron is created, it can never be removed. Because of this, RAN and RANEKF could produce networks in which some hidden units although active

initially, may subsequently end up contributing little to the network output. For example, this phenomenon occurs in identification problems of nonlinear systems with changing dynamics resulting in a network with numerous inactive hidden neurons, as the dynamics that caused their creation initially becomes non-existent. Further the pruning can also help avoid the problem of over parameterization, which is a problem when neural networks are employed in control applications [64].

2.4 Extended Minimal Resource Allocation Network (EMRAN)

The Extended Minimal Resource Allocation Network (EMRAN) has been developed to employ the pruning concept. The methodology behind the EMRAN formulation is to dynamically estimate the number of neurons in the hidden layer as a function of the complexity of the input data. This is accomplished through a combination of growing and pruning of hidden layer neurons. These additions make it suitable for online convergence while maintaining a compact network. Applications of the EMRAN formulation for online adaptive sequential learning applications involving building structures have been presented by Narasimhan *et al.* [5] and Contreras *et al.* [65] [66].

In the algorithm illustrated by Fig. 2.1, network output is computed by evaluating the general Gaussian function in the single hidden layer:

$$\phi_j = \exp^{\frac{-\|\mathbf{v}-\mu_j\|^2}{(\sigma_j)^2}} \tag{2.1}$$

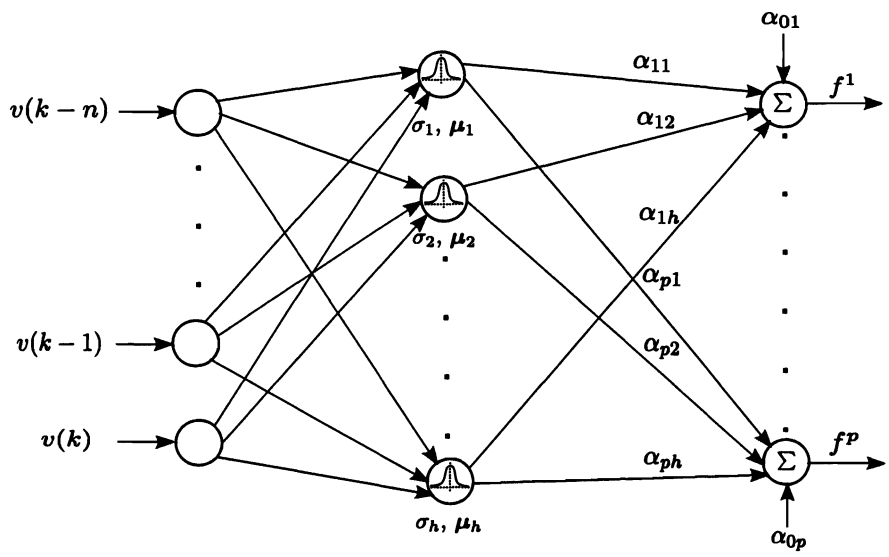

Figure 2.1 : Radial Basis Function Network Topology

and performing the weighted summation of the fully connected output layer:

$$f^i = \sum_{j=1}^{h} \alpha_{ij}\phi_j + \alpha_{0i} \tag{2.2}$$

Then, the following three hidden layer growth criterion Eq. 2.3- 2.5 are calculated at the k^{th} observation:

$$\epsilon_1[k] = max[\epsilon_{max}\gamma^{k-1}, \epsilon_{min}] \tag{2.3}$$

where γ is a decay constant between 0 and 1 representing the scale resolution [59] and ϵ_{max} and ϵ_{min} are determined using optimization procedures discussed in the following section. Error is defined as:

$$\mathbf{e}[k] = \mathbf{f}[k] - \mathbf{f}_d[k] \tag{2.4}$$

where $\mathbf{f}_d$ is the desired output at the k^{th} observation. A performance index is defined

as:

$$J_{rmse} = \sqrt{\frac{\sum_{k=n-S_w+1}^{n} \|\mathbf{e}[k]\|^2}{S_w}} \tag{2.5}$$

where S_w is the length of a given window of samples.

If the following criterion,

$$\|\mathbf{v}[k] - \boldsymbol{\mu}_w[k]\| > \epsilon_1[k] \tag{2.6}$$

$$\|\mathbf{e}[k]\|^2 \geq \epsilon_2 \tag{2.7}$$

$$J_{rmse} \geq \epsilon_3 \tag{2.8}$$

are satisfied for optimized constants ϵ_{max}, γ, ϵ_{min}, ϵ_2, and ϵ_3 then a new neuron is added to the hidden layer with the following three initial properties:

$$\boldsymbol{\alpha}_{j+1}[k] = \mathbf{e}[k-1] \tag{2.9}$$

$$\boldsymbol{\mu}_{j+1}[k] = \mathbf{v}[k] \tag{2.10}$$

$$\sigma_{j+1}[k] = \kappa||\mathbf{v}[k] - \boldsymbol{\mu}_w[k]|| \tag{2.11}$$

where κ is the overlap factor that ensures that the new neuron maintains a sufficiently wide standard deviation to contribute to the output summation for changes in the mean of the input space.

If Eq. 2.6-2.8 are not satisfied, the network parameters of the winner neuron, or neuron that contributes the greatest portion of the output layer summation relative to the other neurons, are updated via the EKF algorithm [60].

By storing the connection weight, center, and width of the winner neuron in $\mathbf{NP}^w$, these parameters can be described at the k^{th} sample by

$$\mathbf{NP}^w[k] = \mathbf{NP}^w[k-1] + \mathbf{K}^w[k]\,\|\mathbf{e}[k-1]\| \tag{2.12}$$

where $\mathbf{K}^w[k]$ is the Kalman gain matrix defined by

$$\mathbf{K}^w[k] = \mathbf{P}^w[k-1]\mathbf{B}^w[k](\mathbf{R}[k] + \mathbf{B}^w[k]^T\mathbf{P}^w[k-1]\mathbf{B}^w[k])^{-1} \tag{2.13}$$

Replacing $\mathbf{NP}^w[k]$ by its vector form, $\mathbf{w}[k]$, the parameter gradient, $\mathbf{B}^w[k] = \nabla_{\mathbf{w}}\mathbf{f}$, can be computed by taking the gradient of $\mathbf{f}$ with respect to vector $\mathbf{w}[k]$ and evaluating at $\mathbf{w}[k-1]$. $\mathbf{R}[k]$ is the variance of the measurement noise, and $\mathbf{P}^w[k]$ is the error of the covariance matrix. $\mathbf{P}^w[k]$ is also updated according to the following

$$\mathbf{P}^w[k] = (\mathbf{I} - \mathbf{K}^w[k]\mathbf{B}^w[k]^T)\mathbf{P}^w[k-1] + q\mathbf{I} \tag{2.14}$$

where q is a scalar signifying the allowed random step in the direction of the gradient vector. If a new hidden neuron is added to the network, the dimensionality of the $\mathbf{P}^w[k]$ is increased by the following expression

$$\mathbf{P}^w[k] = \begin{bmatrix} \mathbf{P}^w[k-1] & \mathbf{0} \\ \mathbf{0} & P_0\mathbf{I} \end{bmatrix} \tag{2.15}$$

where P_0 is a scalar accounting for the new parameter uncertainty.

After evaluating the conditions for adding a neuron, the normalized contribution of each neuron, r^n, for N_w subsequent samples, is calculated to determine the non-contributing neuron for pruning. If $r^n < \delta$, then the neuron is deleted and Eq. 2.12 -2.15 are adjusted accordingly.

2.5 Network Initialization

The EMRAN algorithm requires constants $(\epsilon_{max}, \epsilon_{min}, \epsilon_2, \epsilon_3, \gamma, \kappa, N_w, S_w, \delta, P_0, q)$ to be initialized so that the network is suitable for online stiffness isolation. Selecting the appropriate parameters, involves the optimization of a complicated function which may have many local minima. Due to the large number of variables and the complexity of the function space, a gradient based method was not employed. Instead, a Genetic Algorithm (GA) which was developed to mimic the energy minimization that occurs in the evolutionary process of natural selection was utilized. GAs were developed by Holland in 1975 and they implement techniques such as genetic crossover and mutation to determine future populations of individuals [67]. By representing an individual by a coded string, in this case the EMRAN parameters with fixed bounds on their variance, future generations of the string further optimize those constants.

A GA produces robust populations by maximizing an overall fitness function, which in this case is the negative of the L_2 norm of Eq. 2.4. An initial population size (number of search nodes) are selected and by maximizing the fitness function, the GA produces EMRAN parameters that will allow the RBF network to optimally approximate the system dynamics. Selection of the GA variables was based on those proposed by Narasimhan *et al.* for online learning applications. The genetic mutation, crossover, and selection probabilities were 0.15, 0.6, and 0.08 respectively. To reduce computational time, the maximum number of generations was 500, and the population size initialized to 30 [5].

It is important to note that once the EMRAN parameters are selected by the GA they remain fixed for a given application. The RBF network introduced in this chapter is fairly robust to the initial EMRAN parameters. However, the use of the GA contributes a rigorous determination of those values, thereby ensuring network convergence.

Chapter 3

ADAPTIVE CONTROL IN THE PRESENCE OF SENSOR FAILURE

This chapter presents an adaptive control algorithm capable of compensating for online sensor failure. Online sensor failure is a specific severe fault that affects multi-story smart buildings experiencing a disturbance event. In recent years, Artificial Neural Networks (ANNs) have proven very efficient in adaptive control applications. In this study, the unique application of ANNs involving Radial Basis Functions (RBFs) combined with H_∞ control demonstrates three significant characteristic advantages: (1) real time adaptability, (2) reduced computation time, and (3) most importantly, *no offline training.* The novelty of the proposed controller is elucidated by performing disturbance rejection tests involving a scaled two degree of freedom shear frame subjected to a combined H_∞ and ANN control. The formulation is validated, first, on a traditional lumped mass parameter model of the bench scale frame assuming collocated actuation and sensing on the floors, and second, on a more realistic higher order model of the bench scale frame that accounts for the placement of the piezoelectric sensors and actuators. The proposed controller is shown to enhance the performance of a baseline H_∞ controller in the presence of a sensor failure in either floor.

3.1 Motivation

As smart structures are being instrumented with a greater number of sensors and actuators, the likelihood of online sensor failure increases dramatically. This presents a significant challenge to robust control of these structures. In general, as the degrees of the freedom and the size of the system in consideration increases, more sensors and actuators will be needed to competently control the structure. The smart structural system analyzed in this chapter is a two degree of freedom model structural frame instrumented with piezoelectric sensors and actuators. Piezoelectric sensors and actuators have been used extensively in vibration suppression applications; however, there have been limited studies on civil engineering structures that experience sensor or actuator failure.

3.2 Bench Scale Model

The bench scale structural model considered in this study is constructed from 1/16 in. thick aluminum columns and 1/4 in. thick steel floors assumed to be rigidly fixed by aluminum 'L' brackets in a 3:4 (floor:column) ratio. The system is actuated using two piezoelectric patches located on both sides of the base of the first floor column. Sensors placed on the lower portion of the first and second floors, respectively, measure voltage output due to strain measured at these locations. The sensor and actuator placement is shown in Fig. 3.1. In order to adequately model the system, the modes of the system were excited by a sinesweep input from the base of the system and a

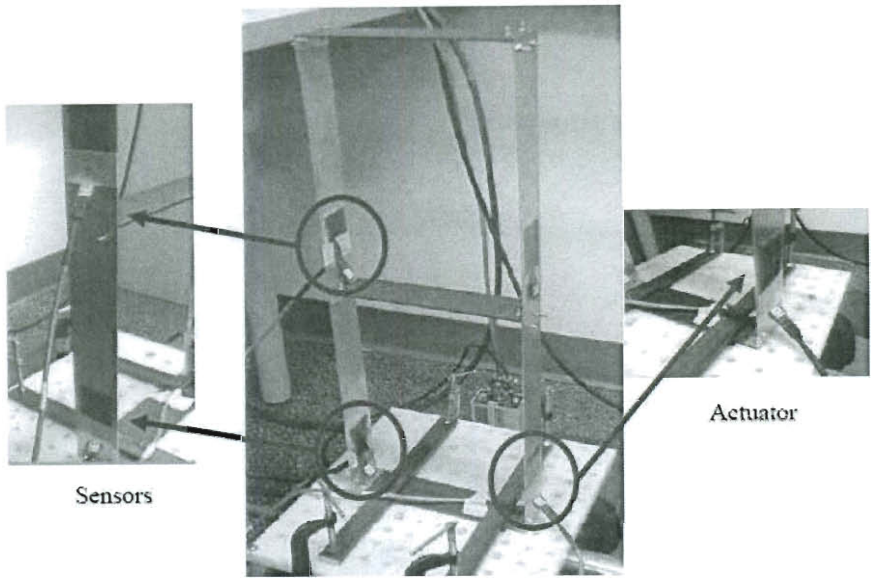

Figure 3.1 : Sensor and Actuator Locations for 2DOF Frame

transfer function was generated from the measured response. Figs. 3.5 and 3.6 show both the measured transfer function data, in the green dotted line, and a polynomial approximation, in red. The transfer function signifying the ratio of second floor response over the base input, and the transfer function signifying the ratio of the first floor response over the base input were generated. Further details regarding system realization of state space matrices is discussed in Section 3.5. The first and second natural frequencies and damping ratios are summarized in Table 3.1.

Table 3.1 : Results of Frame System Identification

$f_i(Hz)$	ζ_i
$f_1 = 2.14$	$\zeta_1 = 1.1\%$
$f_2 = 5.73$	$\zeta_2 = 0.7\%$

Table 3.2 : EMRAN Initialized Parameters

ϵ_{max}	ϵ_{min}	ϵ_2	ϵ_3	γ	κ	N_w	S_w	δ	P_0	q
0.079	0.079	0.0005	0.0005	0.0992	1.6827	185	20	0.008	1.2	0.0002

3.3 Network Algorithm Selection

Radial Basis Functions come from a class of supervised artificial neural networks that have been noted for their computational efficiency. They possess only a single layer of hidden neurons and predefined weight and parameter update rule. The neural network architecture utilized in this study is the Extended Minimal Resource Allocation Network (EMRAN) [68] [69] from Chapter 2. For control applications, this single hidden layer although computationally inexpensive, has to have its parameters initialized prior to operation to avoid poor performance. This initialization is done via the procedures in section 2.5. The following values in Table 3.2 were used to initialize the RBF network prior to the simulations.

3.4 Combined Control Architecture

The control methodology used in this study is composed of a H_∞ feedback controller in combination with a secondary RBF-EMRAN feedback controller, an extension of the control design found in [5] [70]. The sensor output of the system is fed back independently to both controllers and an input from each algorithm is calculated. These inputs are then summed together and sent to the actuators to actively reduce the vibrations induced by excitation. This particular strategy was employed because it best utilizes the strengths of each control algorithm to enhance overall performance.

3.4.1 H_∞ Control Design Using LMI

In order to apply the RBF-EMRAN controller with favorable performance, it is necessary to localize the Gaussian functions of the network to a subspace that can adequately describe baseline behavior of a nominal closed loop stable system. This is done primarily through the GA initialization process in which a closed loop system with H_∞ feedback control and no faulty sensors is used to determine the RBF-EMRAN constants. For the system considered in this chapter which is open loop stable, the implementation of H_∞ control facilitates considerably the performance of the RBF-EMRAN supplemental control input. Without such localization afforded by the application of the H_∞ closed loop behavior, initialization of the neural control may not be possible for such a compact network.

The H_∞ control design in this study was done from a Linear Matrix Inequality

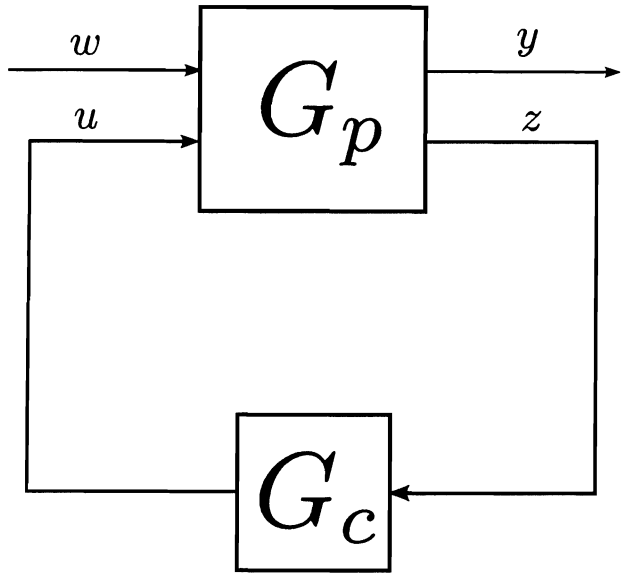

Figure 3.2 : General Feedback Controller

(LMI) perspective. An brief overview of the steps taken to calculate the desired H_∞ control gains is presented herein. Given a general closed loop system (shown in Fig. 3.2) subjected to only an initial disturbance ($\mathbf{w} = \mathbf{0}$) and noise free output feedback ($\mathbf{y} = \mathbf{z}$), the following simplified state space form (3.1a) and (3.1b) for the plant and controller can be written.

$$\begin{aligned}
\dot{\mathbf{x}}_\mathbf{p} &= \mathbf{A_p x_p} + \mathbf{B_p u} + \mathbf{D_p w} = \mathbf{A_p x_p} + \mathbf{B_p u} \\
\mathbf{y} &= \mathbf{C_p x_p} + \mathbf{B_y u} + \mathbf{D_y w} = \mathbf{C_p x_p} + \mathbf{B_y u} \quad \textit{(Plant)} \\
\mathbf{z} &= \mathbf{M_p x_p} + \mathbf{B_z u} + \mathbf{D_z w} = \mathbf{y}
\end{aligned} \tag{3.1a}$$

$$\dot{\mathbf{x}}_\mathbf{c} = \mathbf{A_c x_c} + \mathbf{B_c z} \qquad \textit{(Controller)} \tag{3.1b}$$

$$\mathbf{u} = \mathbf{C_c x_c} + \mathbf{D_c z}$$

Using a Linear Matrix Inequality (LMI) representation, the H_∞ controller gain, or energy to energy norm $\|\mathbf{T_{wy}}\|_\infty$, is less than some value, γ_H, if there exists some $\mathbf{X}$ and $\mathbf{Y}$ such that the following four LMI constraints are satisfied:

$$\begin{bmatrix} \mathbf{B_p} \\ \mathbf{B_y} \end{bmatrix} \begin{bmatrix} \mathbf{A_p X} + \mathbf{X A_p}^T + \mathbf{D_p D_p}^T & \mathbf{X C_p}^T + \mathbf{D_p D_y}^T \\ \mathbf{X C_p}^T + \mathbf{D_p D_y}^T & \mathbf{D_y D_y}^T - \gamma_H^2 \mathbf{I} \end{bmatrix} \begin{bmatrix} \mathbf{B_p} \\ \mathbf{B_y} \end{bmatrix}^{\perp T} < 0 \tag{3.2a}$$

$$\begin{bmatrix} \mathbf{M_p}^T \\ \mathbf{D_z} \end{bmatrix} \begin{bmatrix} \mathbf{Y A_p} + \mathbf{A_p}^T \mathbf{Y} + \mathbf{C_p}^T \mathbf{C_p} & \mathbf{Y D_p} + \mathbf{C_p}^T \mathbf{D_y} \\ \mathbf{Y D_p} + \mathbf{C_p}^T \mathbf{D_y} & \mathbf{D_y}^T \mathbf{D_y} - \gamma_H^2 \mathbf{I} \end{bmatrix} \begin{bmatrix} \mathbf{M_p}^T \\ \mathbf{D_z}^T \end{bmatrix}^{\perp T} < 0 \tag{3.2b}$$

$$\begin{bmatrix} \mathbf{X} & \gamma_H \mathbf{I} \\ \gamma_H \mathbf{I} & \mathbf{Y} \end{bmatrix} \geq 0 \tag{3.2c}$$

$$rank \begin{bmatrix} \mathbf{X} & \gamma_H \mathbf{I} \\ \gamma_H \mathbf{I} & \mathbf{Y} \end{bmatrix} \geq n_p + n_c \tag{3.2d}$$

n_p and n_c are the rank of the plant and the controller respectively. Using $\mathbf{X}$ and $\mathbf{Y}$ that satisfy the proceeding equations and therefore bound the system, the appropriate controller can be calculated from the following LMI constraint for the closed loop stabilization problem:

$$(\mathbf{A} + \mathbf{B G_c M})\mathbf{P} + \mathbf{P}(\mathbf{A} + \mathbf{B G_c M})^T < 0 \tag{3.3}$$

where

$$\mathbf{X} - \mathbf{Y}^{-1} = \mathbf{P_{12}}\mathbf{P_{22}}^{-1}\mathbf{P_{12}}^{T}$$

and

$$\mathbf{A} = \begin{bmatrix} \mathbf{A_p} & 0 \\ 0 & 0 \end{bmatrix} \quad \mathbf{B} = \begin{bmatrix} \mathbf{B_p} & 0 \\ 0 & \mathbf{I} \end{bmatrix} \quad \mathbf{M} = \begin{bmatrix} \mathbf{M_p} & 0 \\ 0 & \mathbf{I} \end{bmatrix} \quad \mathbf{G}_c = \begin{bmatrix} \mathbf{D_c} & \mathbf{C_c} \\ \mathbf{B_c} & \mathbf{A_c} \end{bmatrix}$$

The optimal full order controller gains are calculated by selecting $\mathbf{X}$ and $\mathbf{Y}$ such that γ_H is a minimum, and then using those values to calculate $\mathbf{G}_c$.

3.4.2 Neural-Aided Controller

It is well known that H_∞ control techniques have demonstrated robust control in the presence of uncertainties or perturbations. Given a specific control formulation, optimal performance can be ensured despite uncertainty. However, sensor failures pose a significant challenge to H_∞ control algorithms because a sensor failure effectively reduces the rank of the observability matrix. The reduced rank mandates that a new optimal H_∞ controller be designed, one that is a reduced order controller which relies on reduced feedback. If this does not occur during a real time sensor failure, the nominal H_∞ controller is now *suboptimal.* The imposition of the RBF-EMRAN supplementary control algorithm is to enhance the performance of the now suboptimal controller. The final control design architecture is shown by the block diagram in Fig. 3.3.

It should also be noted that the overall combined control architecture is Bounded Input Bounded Output (BIBO) stable. BIBO stability is a well known characteristic

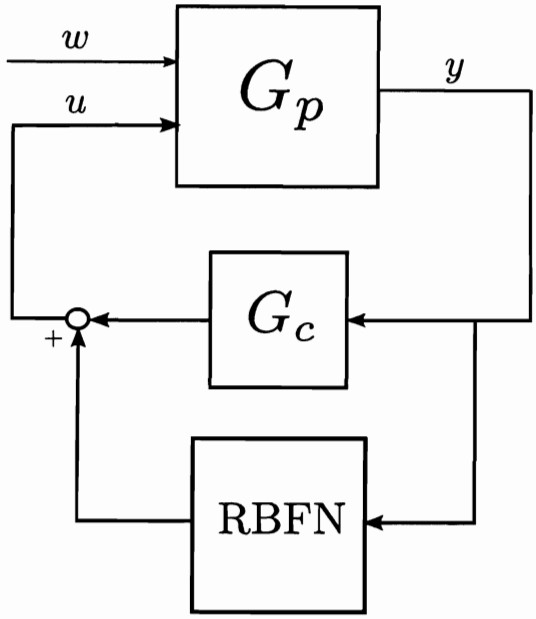

Figure 3.3 : Adaptive Control Architecture

ensured by H_∞ control. Because the contribution to the control input by the RBF-EMRAN is a linear combination of Gaussian basis functions (see Eq. 2.1), which by their definition are bounded between 0 and 1, the RBF-EMRAN contribution to control input will be bounded as well. Since the summation of two bounded quantities is still bounded, the proposed formulation still maintains the essential characteristic of BIBO stability.

3.5 Adaptive Neural-Aided Controller Validations

The bench scale laboratory model possesses a nonstandard configuration of sensors and one actuator. Due to the irregular configuration, it must be demonstrated first

that the adaptive neural-aided controller can be validated on a traditional base excited model having actuators and sensors collocated at each floor. Once this is done, the method is extended to a model that accounts for the piezoelectric sensors and actuator present in the bench scale model.

3.5.1 Realization Representing Collocated Sensing and Actuation

For a bench scale model that is instrumented with active actuators at each floor, it can be represented by the shear frame model depicted in Figure 3.4. This model can accurately be represented by assuming a banded stiffness matrix, $\mathbf{K}$, a diagonal mass matrix, $\mathbf{M}$, and a banded Rayleigh damping matrix, $\mathbf{C}^{damp}$. Using the sinesweep tests results from Table 3.1 and the aforementioned assumptions regarding the form of the matrices, the following values were calculated:

$$\mathbf{K} = \begin{bmatrix} 309.20 & -151.42 \\ -151.42 & 151.42 \end{bmatrix} \quad \mathbf{M} = \begin{bmatrix} 0.33 & 0 \\ 0 & 0.30 \end{bmatrix} \quad \mathbf{C}^{damp} = \begin{bmatrix} 0.05 & -0.01 \\ -0.01 & 0.01 \end{bmatrix} \tag{3.4}$$

assuming the forms:

$$\mathbf{K} = \begin{bmatrix} k_1 + k_2 & -k_2 \\ -k_2 & k_2 \end{bmatrix} \quad \mathbf{M} = \begin{bmatrix} m_1 & 0 \\ 0 & m_2 \end{bmatrix} \quad \mathbf{C}^{damp} = \begin{bmatrix} c_1 + c_2 & -c_2 \\ -c_2 & c_2 \end{bmatrix} \tag{3.5}$$

Once $\mathbf{M}$, $\mathbf{C}^{damp}$ and $\mathbf{K}$ are calculated, the controllable canonical state space representation with output accelerations for a two degree of freedom system can be

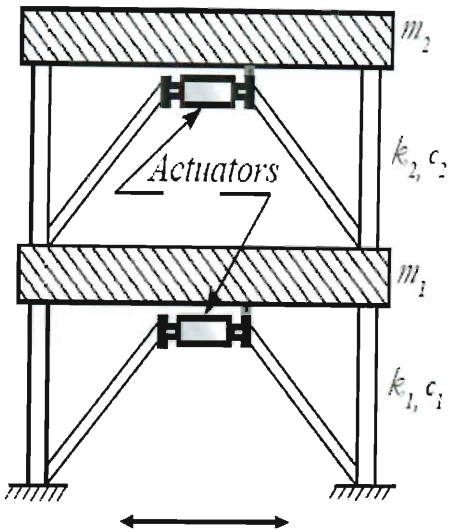

Figure 3.4 : Shear Frame Model Depicted with Actuation in Each Floor

constructed by Eq. 3.3.

$$\dot{\mathbf{x}}_{\mathbf{p}4\times1}(t) = \mathbf{A}_{\mathbf{p}_{4\times4}}\mathbf{x}_{\mathbf{p}_{4\times1}}(t) + \mathbf{B}_{\mathbf{p}_{4\times1}}u(t) \tag{3.3}$$

$$\mathbf{y}_{\mathbf{p}_{2\times1}}(t) = \mathbf{C}_{\mathbf{p}_{2\times4}}\mathbf{x}_{4\times1}(t) + \mathbf{B}_{\mathbf{y}_{2\times1}}u(t)$$

The state variable, $\mathbf{x}_{\mathbf{p}_{4\times1}}$, consists of relative displacement, $\mathbf{x}_{\mathbf{p}_{2\times1}} = \mathbf{x}_{2\times1}$, and relative velocity, $\dot{\mathbf{x}}_{2\times1}$, for all degrees of freedom. $u(t)$ is the input acceleration and $\mathbf{A}_\mathbf{p}$, $\mathbf{B}_\mathbf{p}$, $\mathbf{C}_\mathbf{p}$, and $\mathbf{B}_\mathbf{y}$ are state space matrices defined as follows:

$$\mathbf{A}_{\mathbf{p}_{4\times4}} = \begin{bmatrix} \mathbf{0}_{2\times2} & \mathbf{I}_{2\times2} \\ -\mathbf{M}_{2\times2}^{-1}\mathbf{K}_{2\times2} & -\mathbf{M}_{2\times2}^{-1}\mathbf{C}_{2\times2}^{damp} \end{bmatrix}$$

$$\mathbf{B}_{\mathbf{p}_{4\times1}} = \begin{bmatrix} \mathbf{0}_{2\times1} \\ \mathbf{\Gamma}_{2\times1} \end{bmatrix}$$

$$\mathbf{C}_{\mathbf{p}_{2\times4}} = \begin{bmatrix} -\mathbf{M}_{2\times2}^{-1}\mathbf{K}_{2\times2} & -\mathbf{M}_{2\times2}^{-1}\mathbf{C}_{2\times2}^{damp} \end{bmatrix}$$

and

$$\mathbf{B}_{\mathbf{y}_{2\times1}} = \begin{bmatrix} \mathbf{\Gamma}_{2\times1} \end{bmatrix}$$

where $\mathbf{\Gamma}$ is a vector of unity influence coefficients.

3.5.2 Performance in the Presence of Earthquake Input

The system in Fig. 3.4 is subjected to base excitation from six different earthquake records. The Kobe [Fault Normal (FN) and Fault Parallel (FP)], Newhall (FN and FP), and Erzincan (FN and FP) records were used to excite the system. Since the original full scale earthquake acceleration records were obtained, the records had to be scaled to properly simulate the excitation experienced by a 1:12 scale model ($l_r = \frac{1}{12}$). Table 3.3 show the relevant scaling parameters necessary to complete the simulations.

Table 3.3 : Time Step Scaling

	Full Scale	Scale Factor	Model Scale
Δt	0.005	$\sqrt{l_r} \rightarrow \frac{1}{\sqrt{12}}$	0.0014

Three different fault cases were examined: (1) no sensor failure, (2) sensor failure in floor one, and (3) sensor failure in floor two. The first case is the healthy baseline

case which serves as a nominal benchmark. In order to compare the performance of the responses from all excitations, five performance metrics were selected. $\overline{F}_{bs}$ signifies the total base shear on the frame. $\ddot{\overline{x}}_{fl}$ and $\overline{x}_{max}$ are the maximum floor acceleration and maximum floor displacement experienced in either floor, respectively. Finally, $\overline{x}^{2fl}_{rms}$ and $\ddot{\overline{x}}^{2fl}_{rms}$ are the second floor root mean squared displacements and accelerations, respectively.

No Sensor Failure

The graphical display of the effect of the controllers for the no sensor failure case is shown through the time history responses for displacement and acceleration at each floor illustrated in Fig. 3.8 for the Newhall (FP) quake . It can be seen that the Neuro-H_∞ controller reduces the magnitude of the responses far better that the baseline H_∞ controller and the open loop response. It should also be noted that the Neuro-H_∞ control performance improves as function of time due to the RBFN adapting real time to the system behavior. The results with respect to the five performance measures for all the excitations are summarized in Table 3.4 with the results for the H_∞ controller shown in parenthesis. In almost every instance, the Neuro-H_∞ outperforms the H_∞ baseline controller.

Sensor Failures

Next, the control formulation was verified for the sensor failure scenarios. During each earthquake record either sensor 1 or sensor 2 was failed at a particular time

Table 3.4 : Neuro-H_∞ Performance Measures: No Sensor Failure

Quake	Dir.	$\overline{F}_{bs}$	$\overline{\ddot{x}}_{fl}$	$\overline{x}_{max}$	$\overline{x}^{2fl}_{rms}$	$\overline{\ddot{x}}^{2fl}_{rms}$
Newhall	FN	3.41 (4.34)	1.04 (1.27)	2.23 (2.50)	1.13 (1.69)	0.22 (0.37)
	FP	2.02 (2.57)	0.46 (0.51)	0.96 (1.00)	0.68 (1.01)	0.13 (0.21)
Kobe	FN	4.42 (5.19)	1.20 (1.40)	2.54 (2.76)	1.36 (1.69)	0.27 (0.37)
	FP	1.93 (3.06)	0.62 (0.77)	1.39 (1.37)	0.68 (1.02)	0.15 (0.27)
Erzincan	FN	3.82 (4.83)	0.72 (0.95)	1.73 (1.85)	1.54 (2.27)	0.23 (0.45)
	FP	2.16 (3.10)	0.63 (0.81)	1.37 (1.55)	1.17 (1.00)	0.20 (0.27)

NOTE: Quantities in parenthesis are the measures produced with stand-alone H_∞ controller.

instant. There was a sensor failure at time $t = 1.3$ *sec*, $t = 2.2$ *sec*, and $t = 0.8$ *sec*, for the Newhall, Kobe, and Erzincan records, respectively. A graphical depiction of the sensor failures during each ground excitation is shown in Fig. 3.7.

Illustrative results are displayed for the case where the sensor in floor 1 is failed. Fig. 3.9 shows the displacements and accelerations in each floor for both Neuro-H_∞ and H_∞ feedback control. Despite the failure of the sensor in floor 1, Fig. 3.9 demonstrates that the Neuro-H_∞ controller successfully reduces the vibration more effectively than the H_∞ controller in the presence of the Erzincan (FN) earthquake. In Fig. 3.10, the control force applied to each floor is depicted along with the amount of hidden layer neurons as function of time. It should be noted that the largest increase in neurons occurs following the onset of the sensor failure in floor 1. The

Table 3.5 : Neuro-H_∞ Performance Measures: Failure in Sensor 1

Quake	Dir.	$\overline{F}_{bs}$	$\overline{\ddot{x}}_{fl}$	$\overline{x}_{max}$	$\overline{x}^{2fl}_{rms}$	$\overline{\ddot{x}}^{2fl}_{rms}$
Newhall	FN	0.82 (1.01)	0.86 (1.01)	0.92 (1.01)	0.66 (1.10)	0.63 (1.10)
	FP	0.89 (1.05)	0.94 (1.03)	1.00 (1.04)	0.73 (1.16)	0.68 (1.15)
Kobe	FN	0.86 (1.02)	0.88 (1.03)	0.94 (1.03)	0.79 (1.13)	0.77 (1.12)
	FP	0.89 (1.04)	0.99 (1.03)	0.98 (1.08)	0.76 (1.14)	0.68 (1.13)
Erzincan	FN	0.87 (1.03)	0.87 (1.03)	1.02 (1.03)	0.78 (1.13)	0.68 (1.12)
	FP	0.90 (1.05)	0.89 (1.05)	1.01 (1.07)	1.08 (1.09)	0.85 (1.10)

NOTE: Quantities in parenthesis are the measures produced with stand-alone H_∞ controller. All values are normalized by stand-alone H_∞ controller without a sensor failure.

increase in neurons is a demonstrative effect that the RBFN is adapting to changes to the nominal system. The results with respect to the five performance measures for all excitations are tabulated in Table 3.5 with all values being normalized by the H_∞ performance measures for a no sensor failure case. In every instance, the Neuro-H_∞ outperforms the H_∞ baseline controller.

Finally, results are shown for the case where the sensor in floor 2 is failed. Fig. 3.11 shows the displacement and acceleration responses in each floor for both Neuro-H_∞ and H_∞ feedback control. Fig. 3.11 illustrates that the Neuro-H_∞ controller reduces vibrations more effectively than the H_∞ controller in the presence of the Kobe (FP) earthquake. In Fig. 3.12, the control force applied to each floor is depicted along with the amount of hidden layer neurons as function of time. It is worth noting that the

Table 3.6 : Neuro-H_∞ Performance Measures: Failure in Sensor 2

Quake	Dir.	$\overline{F}_{bs}$	$\ddot{\overline{x}}_{fl}$	$\overline{x}_{max}$	$\overline{x}^{2fl}_{rms}$	$\ddot{\overline{x}}^{2fl}_{rms}$
Newhall	FN	0.82 (1.03)	0.91 (1.01)	0.91 (1.02)	0.91 (1.25)	0.84 (1.21)
	FP	0.96 (1.08)	1.11 (1.06)	1.13 (1.08)	1.04 (1.32)	0.95 (1.29)
Kobe	FN	0.97 (1.05)	1.01 (1.04)	1.02 (1.04)	1.04 (1.26)	1.00 (1.22)
	FP	0.83 (1.07)	0.91 (1.02)	1.03 (1.09)	1.12 (1.27)	0.91 (1.17)
Erzincan	FN	0.93 (1.05)	1.02 (1.05)	1.02 (1.05)	0.95 (1.25)	0.90 (1.25)
	FP	0.89 (1.09)	0.86 (1.06)	0.89 (1.10)	0.96 (1.18)	0.79 (1.11)

NOTE: Quantities in parenthesis are the measures produced with stand-alone H_∞ controller. All values are normalized by stand-alone H_∞ controller without a sensor failure.

control force input from each actuator adapts to compensate for the sensor failure. In Fig. 3.12 (top), the RBFN network is responsible for increasing the magnitude of the Neuro-H_∞ control force from actuator 1 in comparison to the H_∞ control input, while the Neuro-H_∞ force in actuator 2, shown in Fig. 3.12 (middle), relatively mimics the H_∞ control input. This adaption is a result of the loss of feedback from the sensor in floor 2, and the neuro-controller's attempt to maintain good performance. The results with respect to the five performance measures for all excitations are tabulated in Table 3.6 with all values being normalized by the H_∞ performance measures for a no sensor failure case. In all but two instances, the Neuro-H_∞ outperforms the H_∞ baseline controller.

3.5.3 Realization Accounting for Placement of Piezoelectric Actuator and Sensors

As a precursor, the previous simulations were performed using an idealization of the bench scale model. Recalling that the model used in this study is configured with amplified voltage actuation from a piezoelectric patch at the base of the structure and measures strain output from the piezoelectric patches at the base of floors 1 and 2 respectively, it is necessary to generate a new model capable of capturing this behavior. More complex system realization techniques were utilized to represent the dynamics of the real system, thereby enhancing the performance of the proposed control methodology.

Since a black box state space form is desired for the preliminary H_∞ control design, a Prediction-Error Minimization (PEM) method is employed. Given the high fidelity data produced by the piezoelectric sensors, the $\mathbf{K}_e$ matrix which is meant to model error contributions to the state of the system is set to zero. The PEM algorithm was used to produce an 8^{th} order model of the system and realize linear state space matrices: $\mathbf{A}_p, \mathbf{B}_p, \mathbf{C}_p$, and $\mathbf{D}_p$ that could be used for control design. Frequency response functions produced from the 8^{th} order model are shown in Figs. 3.13 and 3.14 and agree quite well with the frequency response functions displayed in Figs. 3.5 and 3.6.

Table 3.7 : Effect of Controllers on Damping Ratio (%)

	No Failure	S_1 *Failed* ($t = 5.5$ *sec*)	S_2 *Failed* ($t = 5.5$ *sec*)
H_∞	5.02	5.28	4.52
Neuro-H_∞	6.62	7.07	5.41
$\frac{\text{Neuro-}H_\infty}{H_\infty}$	1.32	1.34	1.20

3.5.4 Performance in the Presence of First Mode Disturbance

The shear frame is excited by a sine wave at the first mode natural frequency for the first 5 seconds of the simulations. For the healthy case, after 5 seconds free vibration ensues and the control input is applied. For both first and second floor sensor failure scenarios, a complete failure (zero sensor output) is induced independently at $t = 5.5$ seconds in either the first or second floor depending on the failure case. The time domain results for the failure scenarios are presented graphically in Fig. 3.15 and 3.17, and Power Spectral Density (PSD) plots are shown in Fig. 3.16 and 3.18. The location of the actuator contributes to the excellent control performance in the first mode, even when the sensor has completely failed. Also illustrated by Figs. 3.15 and 3.17, following the failure time of $t = 5.5$ seconds, the H_∞ controller is not very effective; however, the fault tolerant RBF-EMRAN formulation is effective. The healthy and sensor failure results with respect to the damping ratio, ζ, and frequency, f, are summarized in Table 3.7 and 3.8.

Table 3.8 : Effect of Controllers on Natural Frequency (Hz)

	No Failure	S_1 *Failed* ($t = 5.5$ *sec*)	S_2 *Failed* ($t = 5.5$ *sec*)
H_∞	2.17	2.20	2.11
Neuro-H_∞	1.90	1.98	1.98
$\frac{\text{Neuro-}H_\infty}{H_\infty}$	0.88	0.90	0.94

3.6 Summary

Using a lumped mass matrix, banded stiffness matrix, and banded damping matrix assumptions, a model was constructed for a two degree of freedom structure with collocated sensing and actuation. The Neuro-H_∞ controller has better performance for disturbance rejection than the baseline H_∞ controller with respect to the five selected performance measures. When the sensors are completely healthy the Neuro-H_∞ controller is capable of bettering performance up to a maximum of approximately 37% when compared to the baseline H_∞ controller. When the sensors are damaged, approximately 41% is the maximum improvement seen when implementing the Neuro-H_∞ control formulation.

Given the unique placement of sensors and small amount of noise present in the input/output voltage data for the laboratory bench scale specimen, the low order system identification model that is obtained is well suited for experimental implementation. In all healthy and sensor failure cases, the Neuro-H_∞ controller has better first mode

disturbance rejection than a baseline H_∞ controller with respect to energy dissipation (PSD plots) and damping ratio (Table 3.7). The Neuro-H_∞ controller was responsible for upwards of 20% improvement in first mode damping ratio, while only moderate improvements were made in damping ratio of the second mode.

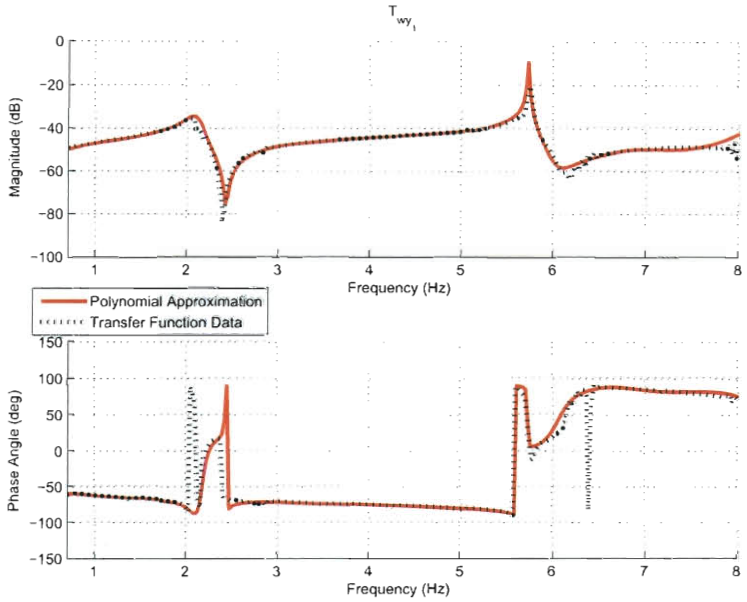

Figure 3.5 : Transfer Function Characterizing the Ratio of the 1^{st} Story Output over Base Input: Data (in green) and Polynomial Approx. (in red)

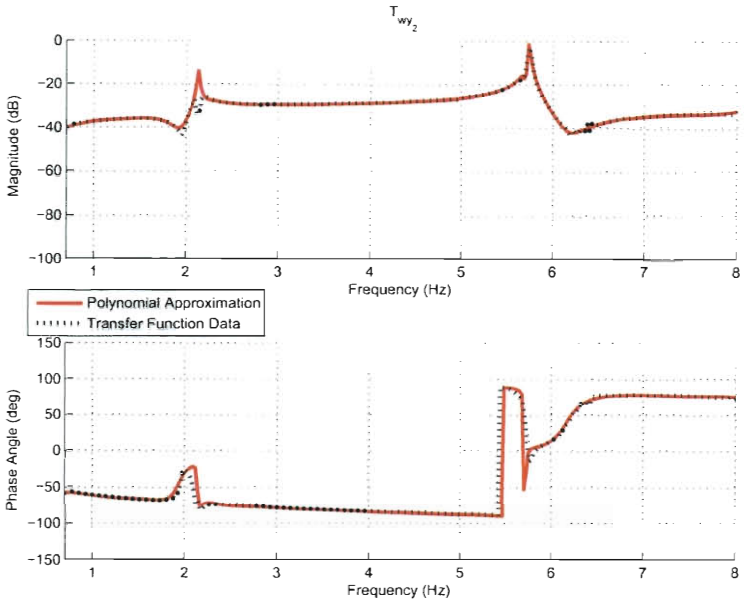

Figure 3.6 : Transfer Function Characterizing the Ratio of the 2^{nd} Story Output over Base Input: Data (in green) and Polynomial Approx. (in red)

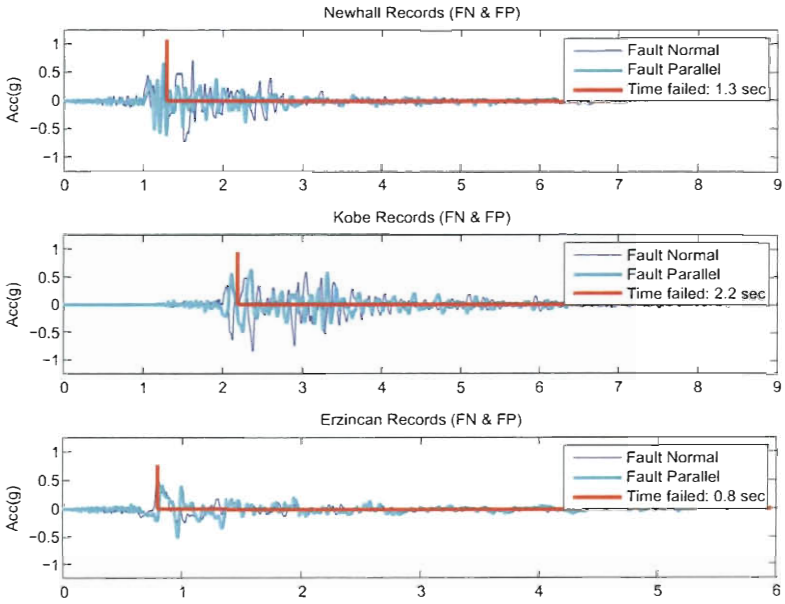

Figure 3.7 : Sensor Failures During Each Quake Record

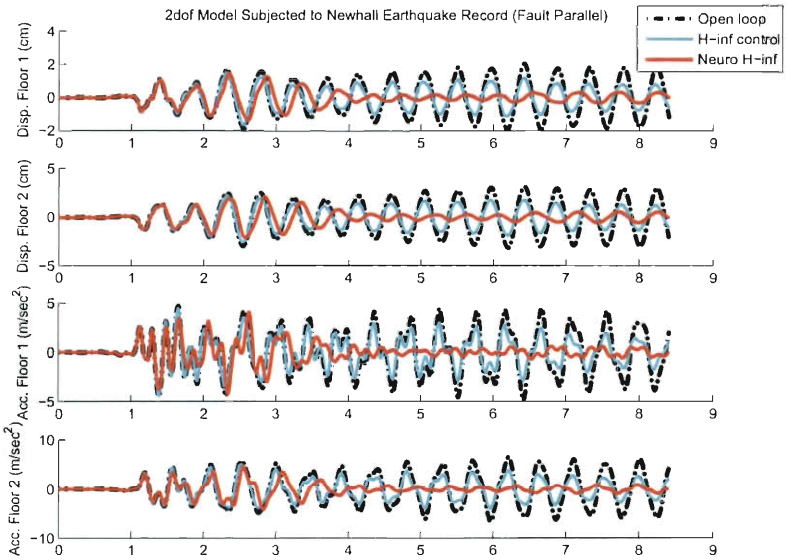

Figure 3.8 : No Sensor Failure: Newhall Earthquake (Fault Parallel)

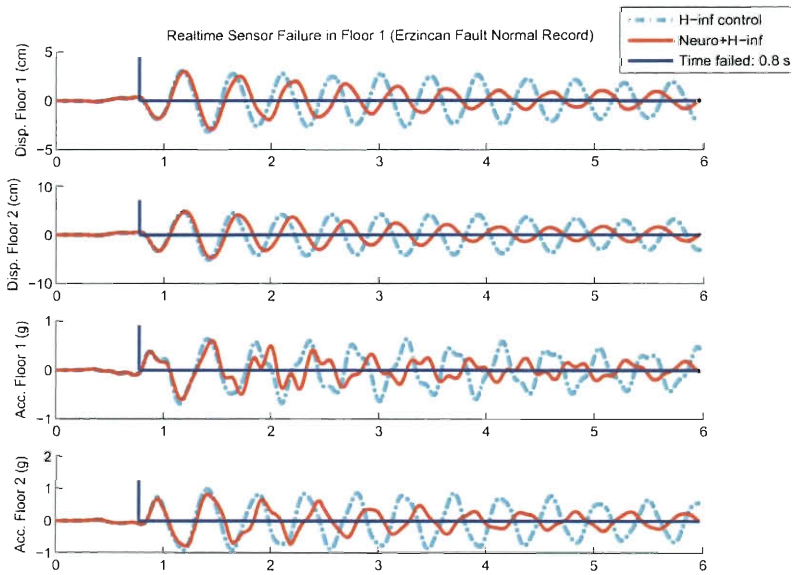

Figure 3.9 : Response during 1^{st} Floor Sensor Failure: Erzincan Earthquake (Fault Normal)

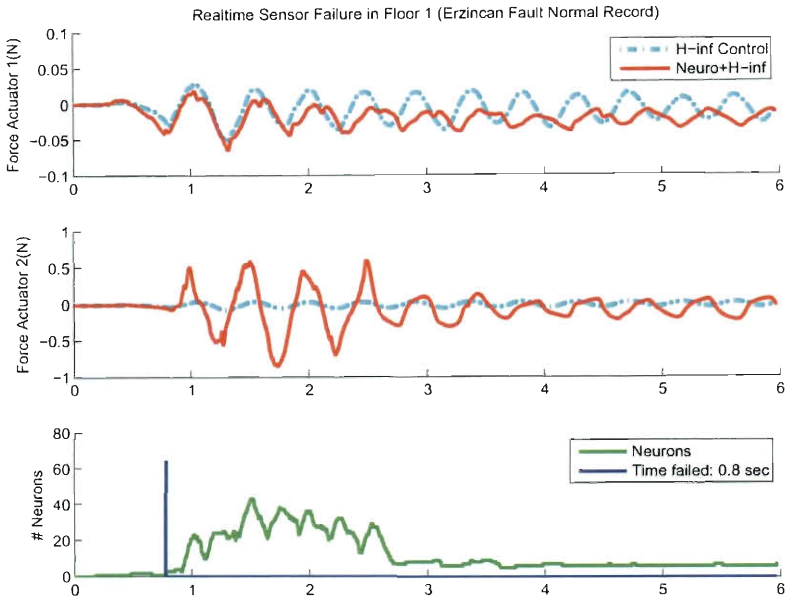

Figure 3.10 : Control Force Input during 1^{st} Floor Sensor Failure: Erzincan Earthquake (Fault Normal)

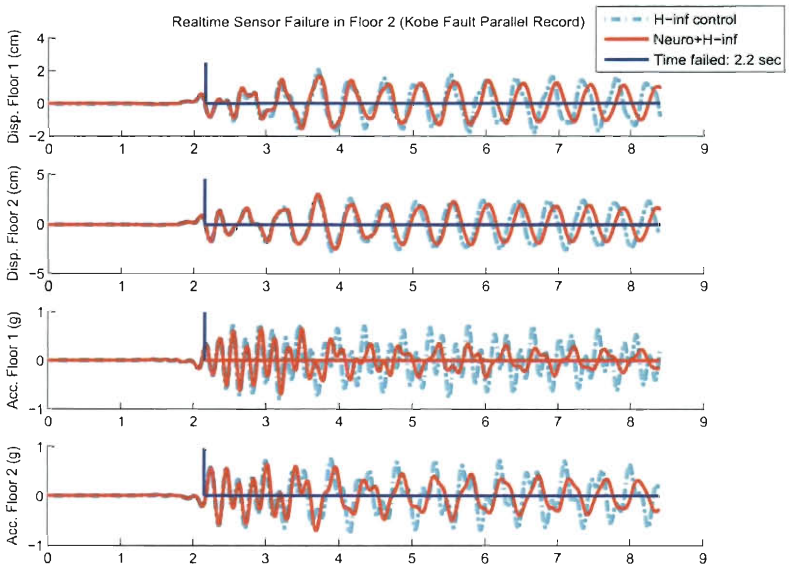

Figure 3.11 : Response during 2^{nd} Floor Sensor Failure: Kobe Earthquake (Fault Parallel)

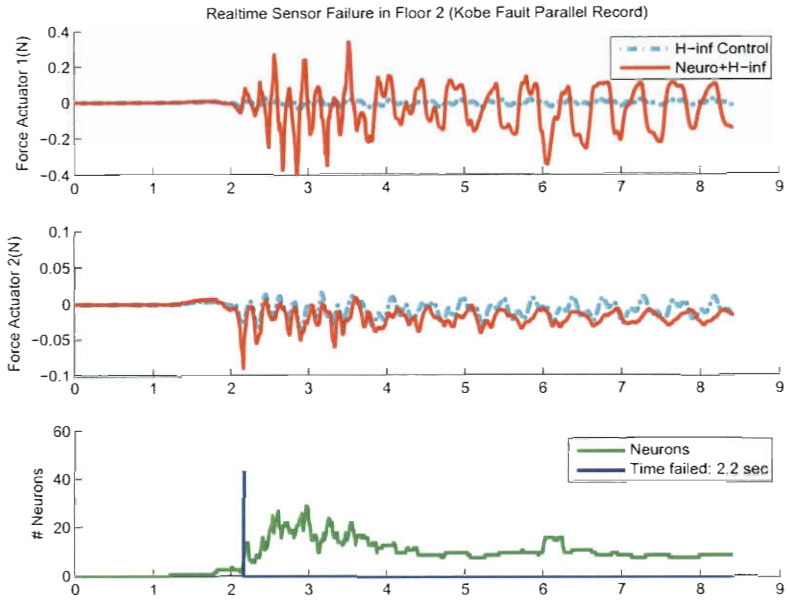

Figure 3.12 : Control Force Input during 2^{nd} Floor Sensor Failure: Kobe Earthquake (Fault Parallel)

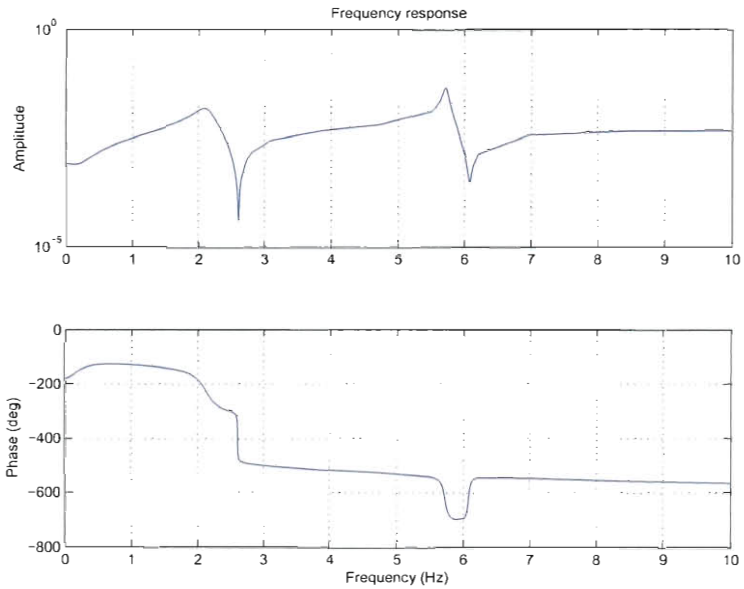

Figure 3.13 : Transfer Function Characterizing the Ratio of the 1^{st} Story Output over Base Input for 8^{th} Order Model

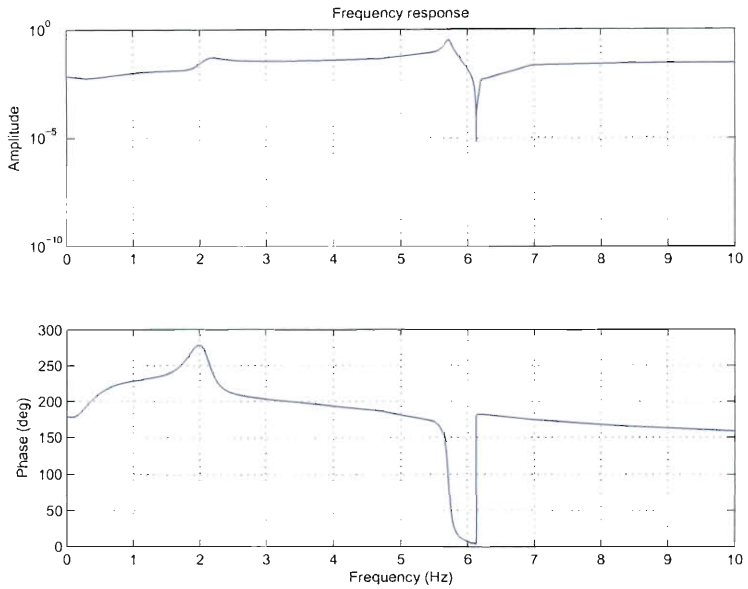

Figure 3.14 : Transfer Function Characterizing the Ratio of the 2^{nd} Story Output over Base Input for 8^{th} Order Model

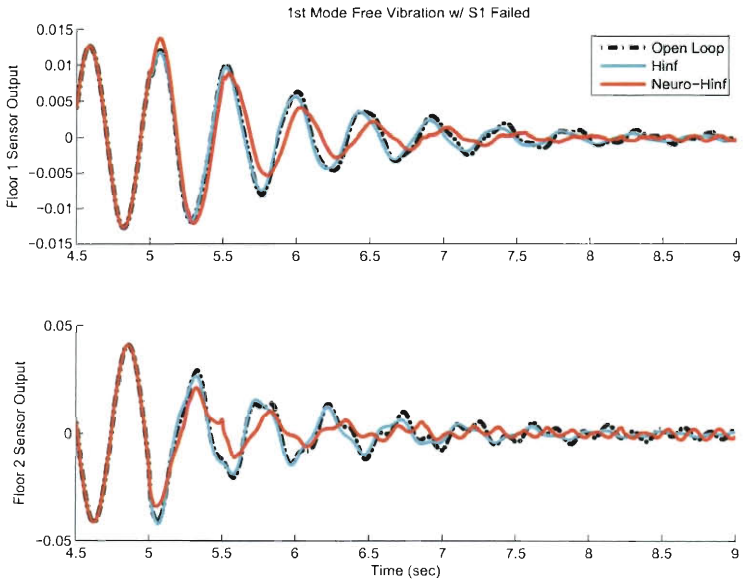

Figure 3.15 : Time Domain Control Performance during Sensor 1 Failure

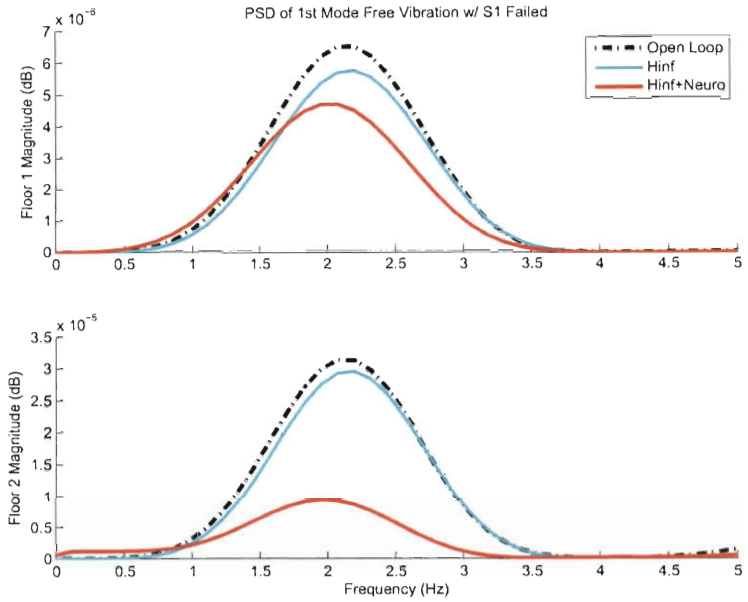

Figure 3.16 : PSD Comparison during Sensor 1 Failure

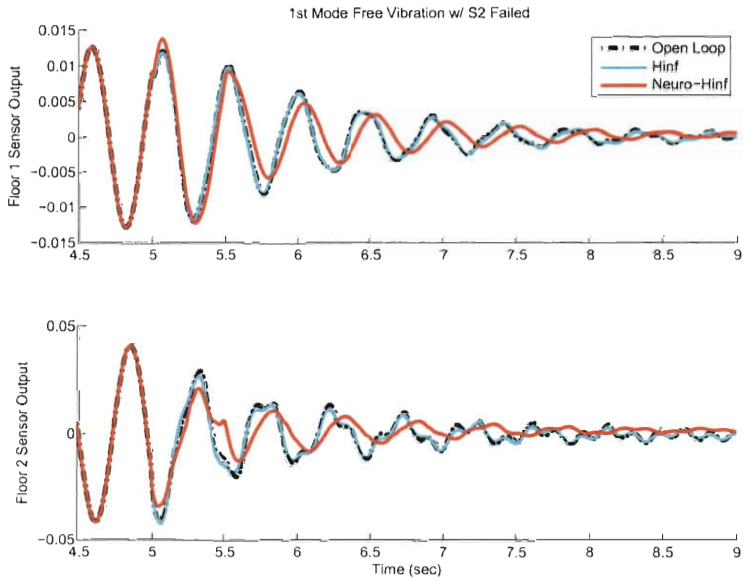

Figure 3.17 : Time Domain Control Performance during Sensor 2 Failure

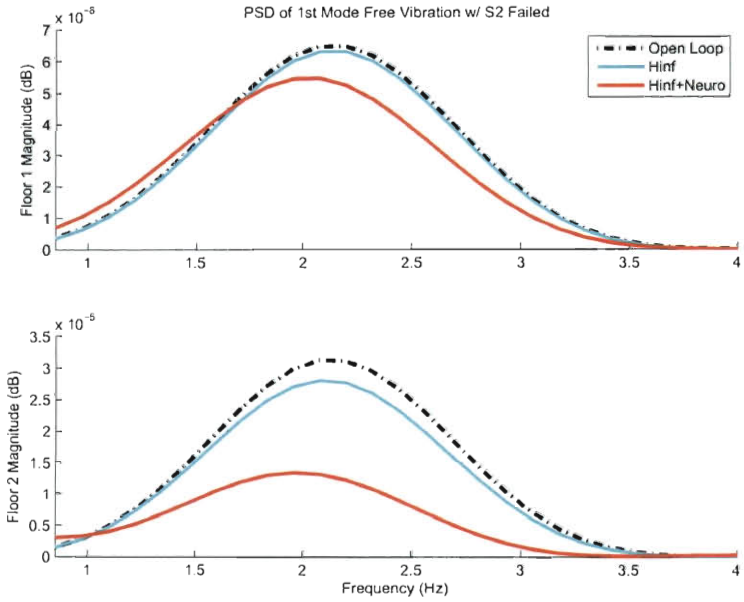

Figure 3.18 : PSD Comparison during Sensor 2 Failure

Chapter 4

REAL TIME DETECTION OF STIFFNESS CHANGE USING A RADIAL BASIS FUNCTION AUGMENTED OBSERVER FORMULATION

In the previous chapter, the proposed control formulation *minimized* an error function produced by comparing a zero response and the output of the structural system. In this chapter a novel formulation has been developed to *track* an error function produced by comparing a healthy response and the output of an altered structural system. The concept of error tracking is an analytical redundancy strategy of structural health monitoring that can be implemented in real time. The foundational concepts of such methods have been introduced in section 1.2.4.

The proposed algorithm is suitable for online applications because it maintains good pattern recognition capabilities while possessing a computationally compact network topology. This study employs the computational efficiency of single layer Radial Basis Function (RBF) approximaters to create a subspace capable of *isolating* faults in multi-degree of freedom systems which involve coupled and uncoupled stiffness changes in real time. The RBF network transforms displacement time history of the varying plant into a decoupled output space which is then compared to a baseline

healthy observer which undergoes the same decoupling transformation. The online comparison of the output of both the time varying plant and the healthy observer in a decoupled subspace comprises the observer based error function.

4.1 Motivation

Many multi-degree of freedom structures, in particular buildings, undergo changes in their system parameters throughout their design life. The more drastic parameter changes may require immediate attention. The motivation to instantly detect structural stiffness changes via an error function has been the impetus for the development of this formulation. The error function is shown to not only detect the existence of faults, but isolate these faults in real time in the presence of base excitation. The method is validated for systems that experience earthquake induced damage, as well as an experimental system using the Semi-Active Independent Variable Stiffness (SAIVS) device which is capable of varying system stiffness in real time. By simply observing the displacement time history responses, the RBF augmented observer formulation is capable identifying changes in the stiffness at each degree of freedom.

The task of detecting real time stiffness change belongs to a subclass of problems dealing with fault detection and isolation (FDI). System stiffness variation can be regarded as a fault, and detection of that variation, representing structural damage, is critical to users or occupants. For systems which have many different types of

faults, it is necessary to attempt the more challenging task of fault isolation, which determines the type of fault. Observer based formulations are a particular type of analytical redundancy strategy that have a longstanding history of demonstrating the capability to perform FDI in real time. In reference to the work of White [71], Massoumnia [72], Douglas [73], Liberatore [50], and very recently Chen and Nagarajaiah [74] [43] [42], most current research focuses on novel techniques to select a feedback detection filter matrix that attempts to decouple the closed loop observer *error* residual; however, few studies implement open loop observer formulations which strive to decouple the system *output* before creating an error residual. By using an interaction matrix formulation, input error functions, input-output inverse models, and time segmented least squares to decouple time history signals, Koh *et al.* [45] [41], Dharap *et al.* [40] [75], Li *et al.* [69] and Nagarajaiah *et al.* [76] were able to perform real time damage detection within an open loop observer framework. The work presented in this paper seeks to unprecedentally combine open loop observer methods with RBF networks to (1) alleviate the requirements associated with the design of a feedback detection filter matrix and (2) extend the previous signal decoupling capabilities for open loop systems by further generalizing the framework for subspace isolation. The main idea of the proposed work is to achieve separation in a transformed function subspace, rather than directly in the signal space. This transformation is achieved using the function approximation capabilities of Artificial Neural Networks (ANN).

4.2 Network Learning Architecture

In the architecture illustrated in Fig. 4.1, the general RBFN topology in Fig. 2.1 has been modified for the real time FDI application. For clarity, relevant equations from

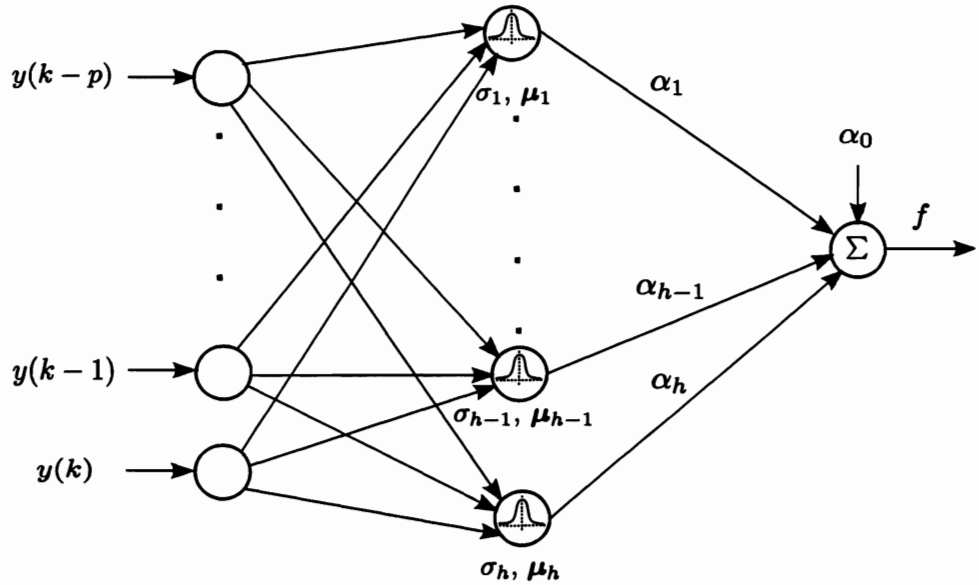

Figure 4.1 : Radial Basis Function Network Topology

Ch. 2 are rewritten for the modified topology. Again, network output is computed by first evaluating a general Gaussian function at each neuron in the single hidden layer:

$$\phi_j = \exp^{\frac{-\left\|y-\mu_j\right\|^2}{(\sigma_j)^2}} \tag{4.1}$$

followed by a the weighted summation of the fully connected output layer creating a scalar output:

$$f = \alpha_0 + \sum_{j=1}^{h} \alpha_j \phi_j \tag{4.2}$$

Then, the following three hidden layer growth criterion Eq. 4.3- 4.5 are calculated at the k^{th} observation:

$$\epsilon_1[k] = max[\epsilon_{max}\gamma^{k-1}, \epsilon_{min}] \tag{4.3}$$

where γ is a decay constant between 0 and 1 representing the scale resolution [59] and ϵ_{max} and ϵ_{min} are determined using optimization procedures discussed in the following section. Error is defined as:

$$e[k] = f[k] - f_d[k] \tag{4.4}$$

where, f_d is the desired output for the k^{th} observation. A performance index is defined as:

$$J_{rmse} = \sqrt{\frac{\sum_{k=n-S_w+1}^{n} e[k]^2}{S_w}} \tag{4.5}$$

where, S_w is the length of a given window of samples.

If the following criterion,

$$\|\mathbf{y}[k] - \boldsymbol{\mu}_w[k]\| > \epsilon_1[k] \tag{4.6}$$

$$e[k]^2 \geq \epsilon_2 \tag{4.7}$$

$$J_{rmse} \geq \epsilon_3 \tag{4.8}$$

are satisfied for optimized constants ϵ_{max}, γ, ϵ_{min}, ϵ_2, and ϵ_3 then a new neuron is added to the hidden layer with the following three initial properties:

$$\alpha_{j+1}[k] = e[k-1] \tag{4.9}$$

$$\boldsymbol{\mu}_{j+1}[k] = \mathbf{y}[k] \tag{4.10}$$

$$\sigma_{j+1}[k] = \kappa||\mathbf{y}[k] - \boldsymbol{\mu}_w[k]|| \tag{4.11}$$

where κ is the overlap factor that ensures that the new neuron maintains a sufficiently wide standard deviation to contribute to the output summation for changes in the mean of the input space.

If Eq. 4.6 - 4.8 are not satisfied, the network parameters of the winner neuron, or neuron that contributes the greatest portion of the output layer summation relative to the other neurons, are updated via the EKF algorithm [60].

By storing the connection weight, center, and width of the winner neuron in $\mathbf{NP}^w$, these parameters can be described at the k^{th} sample by

$$\mathbf{NP}^w[k] = \mathbf{NP}^w[k-1] + \mathbf{K}^w[k]e[k-1] \tag{4.12}$$

The remaining equations related to the EKF algorithm are as before in Eq. 2.13-Eq. 2.15.

Regarding initialization, the EMRAN parameters for the network were selected using the GA optimization scheme discussed in Section 2.5. Since the output is scalar, the fitness function maximized is, $-(e[k]^2)$, to ensure an error close to zero. The values produced by the GA optimization can be found in Table 4.1.

Table 4.1 : EMRAN Initialized Parameters

ϵ_{max}	ϵ_{min}	ϵ_2	ϵ_3	γ	κ	N_w	S_w	δ	P_0	q
0.9699	0.1147	0.0328	0.0024	0.1911	0.6587	5.0	5.0	0.15	17.8613	25.0

4.3 RBF Augmented Observer Formulation

Two factors that hinder the application of open loop observers for FDI are (1) their susceptibility to produce unbounded residuals and (2) the necessary creation of separable fault detection subspaces for the system output [77]. RBF networks resolve these two shortcomings, and by augmenting an open loop observer in the configuration proposed in Fig. 4.2, they are suitable for online application. Details are provided in this section to help elucidate why RBF networks are effective in generating separable subspaces. It will be shown through numerical simulations and experimental observations that the proposed methodology is effective in isolating the location and the onset of faults.

4.3.1 Damage Detection via Bounded Error Residual

By implementing the proposed formulation, the output of a faulty system and the output of a healthy observer are both transformed to a nonlinear radial basis function subspace. It is the error residual produced by comparing these two quantities in real time that is capable of detecting damage. The following subsection will go through some of the key assumptions necessary for detecting damage. Since the damage

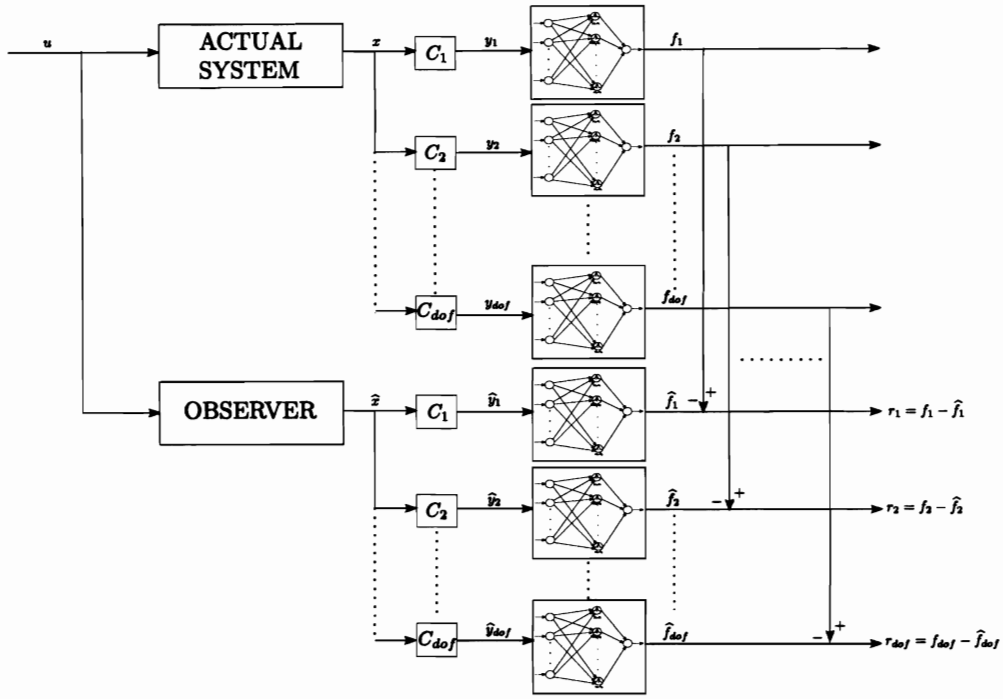

Figure 4.2 : RBFN Augmented Observer Formulation

detection relies heavily on the error function producing either *zero* or *nonzero finite* output, it is important to ensure under no circumstances does its output *tend toward infinity.* Topics related to bounding of the error function and limitation on system type will be addressed.

Suppose some faulty dynamic system can be characterized by the following Linear Time Invariant (LTI) state space representation where $\mathbf{x} \in \mathcal{X}$, $\mathbf{y} \in \mathcal{Y}$, $\mathbf{u} \in \mathcal{U}$ with

$n = \dim(\mathcal{X})$, $m = \dim(\mathcal{Y})$, and $r = \dim(\mathcal{U})$.

$$\dot{\mathbf{x}}(t) = \mathbf{A}\mathbf{x}(t) + \mathbf{B}\mathbf{u}(t) + \sum_{i=1}^{q_n} \mathbf{F}_i m_i(t) \tag{4.13}$$

$$\mathbf{y}(t) = \mathbf{C}\mathbf{x}(t)$$

$\mathbf{A}$ is an $n \times n$ system state transmission matrix, $\mathbf{B}$ is an $n \times r$ input influence matrix, and $\mathbf{C}$ is an $m \times n$ output influence matrix. It was shown by Beard [47], that by defining, $\mathbf{F}_i$ as an $n \times 1$ fault direction vector, and $m_i(t)$ as the i^{th} arbitrary scalar function of time ($i = 1, 2, ..., q$) for q different faults, actuator, sensor, and structural faults can be described when $m_i(t) \neq 0$ [47].

Assuming an accurate observer of the healthy system can be created (*ie.* $\widehat{\mathbf{A}} = \mathbf{A}$, $\widehat{\mathbf{B}} = \mathbf{B}$, and $\widehat{\mathbf{C}} = \mathbf{C}$), the following expression for $\widehat{\mathbf{x}} \in \mathcal{X}^n$ and $\widehat{\mathbf{y}} \in \mathcal{Y}^m$ describes the estimated state for identical bounded input, $\mathbf{u}(t)$, without the effect of faults.

$$\dot{\widehat{\mathbf{x}}}(t) = \mathbf{A}\widehat{\mathbf{x}}(t) + \mathbf{B}\mathbf{u}(t) \tag{4.14}$$

$$\widehat{\mathbf{y}}(t) = \mathbf{C}\widehat{\mathbf{x}}(t)$$

Recall (Fig. 4.2) that the proposed formulation uses a scalar output, y_{dof}, for each degree of freedom produced by $\mathbf{C}_{dof}$. Consider a particular degree of freedom's output ($y = y_{dof}$ produced by $\mathbf{C} = \mathbf{C}_{dof}$) of the faulty system in which the observer will produce corresponding output $\widehat{y} = \widehat{y}_{dof}$. By storing $p + 1$ points of data, a vector $\mathbf{y} \in \Re^{p+1}$ and $\widehat{\mathbf{y}} \in \Re^{p+1}$ for the k^{th} instant can be created.

$$\mathbf{y} = [y(k-p)... \; y(k-1) \; y(k)]' = [\mathbf{C}\mathbf{x}(k-p)... \; \mathbf{C}\mathbf{x}(k-1) \; \mathbf{C}\mathbf{x}(k)]' \tag{4.15}$$

$$\widehat{\mathbf{y}} = [\widehat{y}(k-p)... \ \widehat{y}(k-1) \ \widehat{y}(k)]' = [\mathbf{C}\widehat{\mathbf{x}}(k-p)... \ \mathbf{C}\widehat{\mathbf{x}}(k-1) \ \mathbf{C}\widehat{\mathbf{x}}(k)]' \tag{4.16}$$

The RBFN hidden layer then performs a basis transformation on $\mathbf{y}$ and $\widehat{\mathbf{y}}$ described by Eq. 4.1, for a function $\Phi : \mathbf{y} \rightarrow \boldsymbol{\phi}$, where $\boldsymbol{\phi} \in \Re^h$. The total network output can be described by function composition, $(f \circ \Phi)(\mathbf{y}) : \Re^{p+1} \rightarrow \Re^1$, adapted from Eq. 4.2 and shown below for f and $\widehat{f}$,

$$f = \alpha_0 + \sum_{j=1}^{h} \alpha_j \phi_j(\mathbf{y}) \tag{4.17}$$

$$\widehat{f} = \alpha_0 + \sum_{j=1}^{h} \alpha_j \phi_j(\widehat{\mathbf{y}}) \tag{4.18}$$

Due to the properties of unscaled Gaussian functions with fixed centers and standards of deviation (see Eq. 4.1), the following will hold true.

$$0 < \phi_j(\mathbf{y}) \leq 1 \ \ \forall \ \ \mathbf{y} \in \Re^{p+1} \tag{4.19}$$

From Eq. 4.19, it follows that f and $\widehat{f}$ remain in some ball of radius, $\beta_1, \beta_2 \in \beta$. This is conveyed by the following expressions:

$$\left| \alpha_0 + \sum_{j=1}^{h} \alpha_j \phi_j(\mathbf{y}) \right| \leq \beta_1 \ \ \forall \ \ \mathbf{y} \in \Re^{p+1} \tag{4.20}$$

and,

$$\left| \alpha_0 + \sum_{j=1}^{h} \alpha_j \phi_j(\widehat{\mathbf{y}}) \right| \leq \beta_2 \ \ \forall \ \ \mathbf{y} \in \Re^{p+1} \tag{4.21}$$

since $(f \circ \Phi)(\mathbf{y})$ is invariant to input from $\widehat{\mathbf{y}}$, the error residual, r, shown in Eq. 4.22 is also bounded.

$$|r| = \left| f - \widehat{f} \right| \leq \beta \ \ \forall \ \ \mathbf{y} \in \Re^{p+1} \tag{4.22}$$

Now that the error residual has been shown to be bounded, it is only plausible that it produces either *zero values*, or *nonzero finite values.* The bounded condition on the residual is necessary, but not sufficient for fault detection. The formulation requires a further assumption that the state transition matrix, $\mathbf{A}$, be stable. For the structural systems presented in this paper this is true; however, there exist systems which are input to state stable, or stabilizable by input, of which this formulation is not capable of detecting damage. Reasons as to why the system must be stable are elucidated further in the next section.

4.3.2 Fault Isolation using the Error Residual

The solutions for both the faulty system and the observer are as follows:

$$\mathbf{x}(t) = e^{\mathbf{A}t\mathbf{x}(0)} + \int_0^t e^{\mathbf{A}(t-\tau)}\mathbf{B}\mathbf{u}(\tau)d\tau - \sum_{i=1}^{q_n}\int_0^t e^{\mathbf{A}(t-\tau)}\mathbf{F}_i m_i(\tau)d\tau \tag{4.23}$$

$$\widehat{\mathbf{x}}(t) = e^{\mathbf{A}t}\widehat{\mathbf{x}}(0) + \int_0^t e^{\mathbf{A}(t-\tau)}\mathbf{B}\mathbf{u}(\tau)d\tau \tag{4.24}$$

It can be seen for the systems considered in this study (stable $\mathbf{A}$ and bounded, scalar $u(t)$) the transient terms, $e^{\mathbf{A}t}\mathbf{x}(0)$ and $e^{\mathbf{A}t}\widehat{\mathbf{x}}(0)$ will tend to zero and the remaining terms tend toward constant values, provided by their Taylor expansions, yielding expressions Eq. 4.25 and Eq. 4.26. It should be noted that the following derivation is also valid for systems with modeled noise. For simplicity, it is not included here, but the end result still holds true. For the details regarding the treatment of noise for FDI, readers are referred to the work of Douglas on robust H_∞ bounded detection

filters [73].

$$\mathbf{x} = \left[\psi_0 \mathbf{A}^0\mathbf{B} + \psi_1 \mathbf{A}^1\mathbf{B} + \psi_2 \mathbf{A}^2\mathbf{B} + \ldots\right] - \sum_{i=1}^{q_n} \left[\Gamma_{i0}\mathbf{A}^0\mathbf{F}_i + \Gamma_{i1}\mathbf{A}^1\mathbf{F}_i + \Gamma_{i2}\mathbf{A}^2\mathbf{F}_i + \ldots\right] \tag{4.25}$$

$$\widehat{\mathbf{x}} = \left[\psi_0 \mathbf{A}^0\mathbf{B} + \psi_1 \mathbf{A}^1\mathbf{B} + \psi_2 \mathbf{A}^2\mathbf{B} + \ldots\right] \tag{4.26}$$

where in Eq. 4.25 and Eq. 4.26, ψ_l and Γ_{il}, are defined by,

$$\psi_l = \int_0^t \frac{(t-\tau)^l}{l!} u(\tau) d\tau \tag{4.27}$$

$$\Gamma_{il} = \int_0^t \frac{(t-\tau)^l}{l!} m_i(\tau) d\tau \tag{4.28}$$

The solutions in Eq. 4.25 and Eq. 4.26 only differ by the contribution of the fault term and can be rewritten as follows,

$$\mathbf{x} = \boldsymbol{\Delta}_B - \boldsymbol{\Delta}_F \tag{4.29}$$

$$\widehat{\mathbf{x}} = \boldsymbol{\Delta}_B \tag{4.30}$$

where

$$\boldsymbol{\Delta}_B = \sum_{l=1}^{\infty} \psi_l \mathbf{A}^l\mathbf{B} \tag{4.31}$$

and

$$\boldsymbol{\Delta}_F = \sum_{i=1}^{q_n} \boldsymbol{\delta}_{F_i} = \sum_{i=1}^{q_n} \sum_{l=1}^{\infty} \Gamma_{il}\mathbf{A}^l\mathbf{F}_i \tag{4.32}$$

By plugging in the Eq. 4.29 and Eq. 4.30 into Eq. 4.13 and Eq. 4.14, the output of a particular degree of freedom ($y = y_{dof}$ produced by $\mathbf{C} = \mathbf{C}_{dof}$) for both the system and the observer can be written by the expressions below, respectively.

$$y = \mathbf{C}(\boldsymbol{\Delta}_B - \boldsymbol{\Delta}_F) \tag{4.33}$$

$$\widehat{y} = \mathbf{C}(\mathbf{\Delta}_B) \tag{4.34}$$

The network input vector for both the faulty system and the observer are constructed according to Eq. 4.15 and Eq. 4.16 and propagated through the Gaussian function as shown below. For simplicity of illustration, scalar, μ_j, is assumed.

$$\phi_j = \exp\left[\frac{-||\mathbf{C}\mathbf{\Delta}_B - \mathbf{C}\mathbf{\Delta}_F - \mu_j||^2}{\sigma_j^2}\right] \tag{4.35}$$

$$\widehat{\phi}_j = \exp\left[\frac{-||\mathbf{C}\mathbf{\Delta}_B - \mu_j||^2}{\sigma_j^2}\right] \tag{4.36}$$

By assuming the following expression regarding μ_j,

$$\mu_j = \mu_B - c_{F_m} \tag{4.37}$$

where μ_B is defined to be some scalar center capable of localizing the input space, and c_{F_m} is a center capable of distancing appropriately perturbations of the $\mathbf{F}_m^{th}$ fault relative to all faults, $\mathbf{F}_i$. Eq. 4.35 and Eq. 4.36 can be simplified for systems which are adequately tuned to the input, (ie. $\mathbf{C}\mathbf{\Delta}_B - \mu_B = 0$).

$$\phi_j = \exp\left[\frac{-||c_{F_m} - \mathbf{C}\mathbf{\Delta}_F||^2}{\sigma_j^2}\right] \tag{4.38}$$

$$\widehat{\phi}_j = \exp\left[\frac{-||c_{F_m}||^2}{\sigma_j^2}\right] \tag{4.39}$$

Eq. 4.38 can be expressed as a summation of $\mathbf{F}_i$ fault terms with P_i faulty magnitude scaling, by the following:

$$\phi_j = \exp\left[\frac{-||c_{F_m} - P_1\mathbf{C}\boldsymbol{\delta}_{F_1} - P_2\mathbf{C}\boldsymbol{\delta}_{F_2} - ...||^2}{\sigma_j^2}\right] \tag{4.40}$$

It is desired that Eq. 4.40 express only damaged values ($0 < \phi_j < 1$) in the presence of the $\mathbf{F}_{m^{th}}$ fault. For this to be true the substitution, $\sigma_j = \sigma_{F_m}$, is made. Next, c_{F_m} and σ_{F_m} must be selected such that the following condition is fulfilled:

$$\frac{c_{F_m} - P_m \mathbf{C}\boldsymbol{\delta}_{F_m}}{\sigma_{F_m}} >>> \frac{P_i \mathbf{C}\boldsymbol{\delta}_{F_i}}{\sigma_{F_m}} \quad \forall \ i \neq m \tag{4.41}$$

where $\frac{P_i \mathbf{C}\boldsymbol{\delta}_{F_i}}{\sigma_{F_m}}$ is sufficiently small. If Eq. 4.37 and Eq. 4.41 are true, the proposed detection filter is valid for fault, $\mathbf{F}_m$, even if there exists the presence of faults $\mathbf{F}_i$ because $r_j = \alpha_j(\phi_j - \widehat{\phi}_j) \rightarrow 0, \ \mathbf{F}_m \rightarrow \mathbf{0}$.

Therefore, the solution to the fault isolation problem given the proposed RBFN augmented observer formulation lies in adequately tuning the centers, $\boldsymbol{\mu}_j$, and standards of deviation, σ_j, of h number of basis functions such that the $\mathbf{F}_m^{th}$ faulty contribution to the error residual can be separated from all remaining faults that may or may not exist in the system. It is a further proposition of this study that this desired level of tuning and separation can be accomplished by a generalized training scheme described in detail in the following subsection.

Specifically regarding tuning, due the excellent localization properties of RBF networks with adequate training data sets, it is possible to isolate faults that are sufficiently distinct. This statement is verified using both numerical and experimental results. Further, theoretical justification for separation capability of the RBFs is provided by Cover's theorem on the separability of patterns [78]. In Cover's theorem on the separability of patterns, he was able to prove that a pattern classification problem cast in a nonlinear space of higher dimension is more likely to be separable

than in a low dimensional space [78]. It is illustrated by the following validations that given an adequate training set, and maximum dimensionality of the RBF hidden layer, separation is not only possible, but robust toward a variety of inputs and damage scenarios.

4.3.3 Training the Network for Fault Isolation

As shown previously, the fault isolation characteristic of the RBFN relies heavily on the selection of RBF parameters. The training scheme presented in this section has been shown to (1) be general enough to apply to a wide class of problems and (2) adequately tune the RBF parameters such that they can isolate coupled and uncoupled damage.

In order to create the necessary mapping from displacement to separable fault detection space, the neural network has to be trained offline using perturbations of the of a system model. The systems in this study are subjected to varying levels of damage by changing the stiffness in each DOF. Corresponding displacement data is generated. The training input to the RBF network is comprised of $p + 1$ preceding displacement values in each DOF at a certain instant k. The desired training output is the value of the stiffness term known *a priori* that corresponds to those $p + 1$ displacements.

The learning process in a single iteration of training is as follows (see Fig. 4.3). First, $p+1$ displacements preceding and including instant, k, comprise input vector, $\mathbf{y}$,

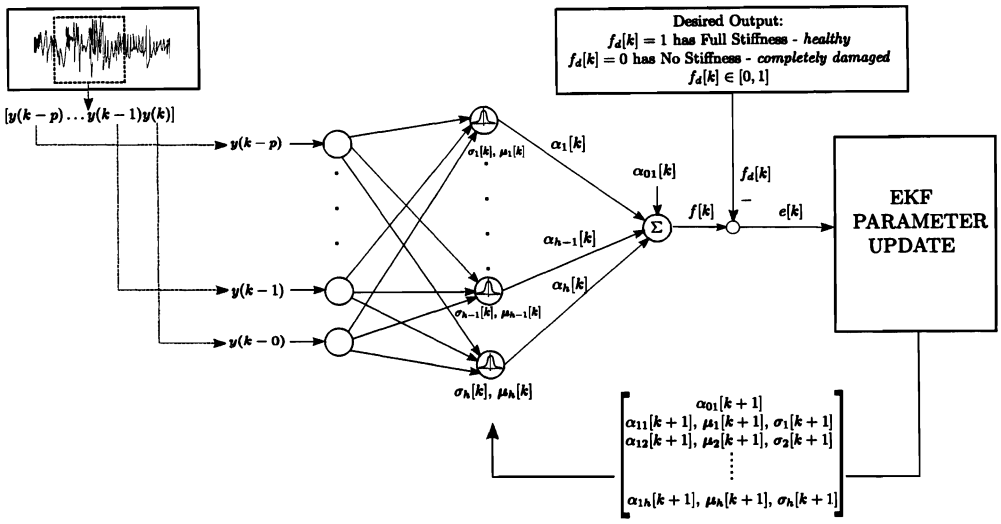

Figure 4.3 : Single Iteration of Recursive Training Scheme

and $\mathbf{y}$ is fed into the RBF network. Based on the size of the network's hidden layer and value of the weights, the RBF network then computes an output. Next, the computed output is compared to the desired output which varies between 0 - no stiffness - and 1 -full stiffness. If the error between network output and desired training output is large the tuning parameters are updated optimally using the EKF algorithm shown in Eq. 4.12 - Eq. 2.15. The training process moves to another arbitrary instant, k, and performs the same computations. At that instant, if the error between computed and desired output is sufficiently small, then the weights and parameters cease to be updated. The RBF network is now ready to be implemented for testing.

It should be noted that during this training process, it is not necessary for the exact testing damage case to be shown to the network. The main motivation for the

training process is that after seeing a general variety of damage scenarios, the RBFN can adequately classify in real time a test pattern similar, but not exactly the same, to those patterns seen during training.

4.4 Simulation Using Earthquake Input

Before verifying the formulation experimentally, the method is first implemented analytically on a two degree of freedom mass-spring-damper system shown in Fig. 4.4 and a ten degree of freedom mass-spring-damper system shown in Fig. 4.5. Both models were subjected to coupled fault scenarios in the presence of the Mexico City (1985 EW) and Jiji (NS) quake cases and uncoupled fault scenarios in the presence of the Mexico City (1985 EW) and Jiji (NS) quake cases. The results in both cases are presented in subsequent sections. During certain pulses of the quake excitations, both systems experience a fault scenario signified by a decrease in stiffness in selected degrees of freedom. The formulation is shown to detect both coupled and uncoupled stiffness changes in the simulations.

Throughout the remainder of this chapter the state space representation for a general multi degree of freedom system subjected to input excitation and whose output is displacements at each DOF is implemented (described below by Eq. 4.42).

$$\dot{\mathbf{x}}_{2n\times 1}(t) = \mathbf{A}_{2n\times 2n}\mathbf{x}_{2n\times 1}(t) + \mathbf{B}_{2n\times 1}u(t) \tag{4.42}$$

$$\mathbf{y}_{n\times 1}(t) = \mathbf{C}_{n\times 2n}\mathbf{x}_{2n\times 1}(t)$$

The state variable, $\mathbf{x}_{2n\times 1}$, consists of relative displacement, $\mathbf{x}_{n\times 1}$, and relative velocity, $\dot{\mathbf{x}}_{n\times 1}$, for all degrees of freedom. $u(t)$ is the input acceleration and $\mathbf{A}$, $\mathbf{B}$, and $\mathbf{C}$ are state space matrices defined as follows:

$$\mathbf{A}_{2n\times 2n} = \begin{bmatrix} \mathbf{0}_{n\times n} & \mathbf{I}_{n\times n} \\ -\mathbf{M}_{n\times n}^{-1}\mathbf{K}_{n\times n} & -\mathbf{M}_{n\times n}^{-1}\mathbf{C}_{n\times n}^{damp} \end{bmatrix}$$

$$\mathbf{B}_{2n\times 1} = \begin{bmatrix} \mathbf{0}_{n\times 1} \\ \mathbf{\Gamma}_{n\times 1} \end{bmatrix}$$

and

$$\mathbf{C}_{n\times 2n} = \begin{bmatrix} \mathbf{I}_{n\times n} & \mathbf{0}_{n\times n} \end{bmatrix}$$

where $\mathbf{M}$, $\mathbf{C}^{damp}$ and $\mathbf{K}$ are matrices for mass, damping, and stiffness respectively. $\mathbf{\Gamma}$ is a vector of unity influence coefficients corresponding to the degrees of freedom in which the system is receiving input acceleration.

It is commonly known that the linear time invariant state space representation in Eq. 4.42 can describe a general mass-spring-damper structure or shear type building of arbitrary, n, degrees of freedom. By setting $n = 2$ and $n = 10$ respectively, the proper dimension of the simulation models displayed in Fig. 4.4 and Fig. 4.5 are set and their time history responses to input can be simulated. The state space models are used to represent both the actual system and the healthy observer in both the $n = 2$ and $n = 10$ validations. Damage is induced by varying the stiffness values of the appropriate DOF in matrix, $\mathbf{K}$, during select time intervals and simulating the time varying response.

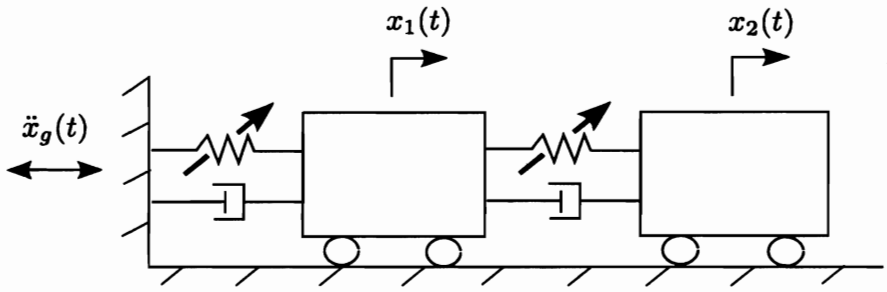

Figure 4.4 : Two Degree of Freedom System with Variable Stiffness

4.4.1 Results for 2-DOF Mass-Spring-Damper System

The effectiveness of the RBF algorithm is demonstrated using a 2-DOF system subjected to the earthquake cases mentioned previously. The 2-DOF system in Fig. 4.4 has the modal parameters found in the Table 4.2. This model is used to generate proper training time histories that validate the FDI capabilities of the RBFN formulation. The network is trained as described in section 4.3. During training, a sinusoidal excitation is used to drive the system while the stiffness in each degree of freedom is damaged an incremental amount. The frequencies of the training excitation are based on the dominant frequencies of excitation that the system will experience during testing. These dominant frequencies are determined before hand from site specific response spectra for earthquake excitations and Fourier spectrum for harmonic excitations. The resulting displacement response serves as training input to the network and the incremental damage as desired output. The sinusoidal excitation, damage scenarios, and resulting response used to train the network in the

case of the Mexico City verification are shown in Fig. 4.7 and 4.8. The sinusoidal excitation - again, determined from site specific response spectra, damage scenarios, and resulting response used to train the network for the Jiji verification are shown in Fig. 4.9 and 4.10.

Table 4.2 : Two DOF System Properties

$\omega(rad/sec)$	$\zeta(\%)$
$\omega_1 = 7.67$	$\zeta_1 = 1.8$
$\omega_2 = 19.92$	$\zeta_2 = 10.2$

After training, the weights are set. The test damage scenarios are meant to mimic damage in a building with stiffness losses occurring at designated time instances corresponding to larger pulses within the quake record. Regarding the selection of the dimension of the input vector, it is selected such that $\mathbf{y} \in \Re^{11}$ at instant k for $p = 10$ and is consistent for both training and testing. The simulation sampling rate is 1000 Hz. The following illustrative results are taken from the coupled damage scenario verifications. Uncoupled damage scenario results were omitted due to space.

The excitations and damages scenarios for the 2-DOF system subjected to the Mexico city case are shown in Fig. 4.11. In DOF 1, the system remains healthy until 86 seconds when it experiences a 10% stiffness loss. In DOF 2, the system experiences an 8% stiffness loss at 46 seconds. The error functions track the onset and existence of damage in each DOF accurately as evidenced by the error functions shown in

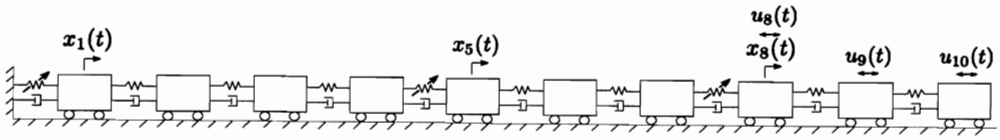

Figure 4.5 : Ten Degree of Freedom System with Variable Stiffness

Fig. 4.12.

The excitations and damages scenarios for the 2-DOF system subjected to the Jiji quake case are shown in Fig. 4.13. In DOF 1, the system remains healthy until 50 seconds when it experiences a 10% stiffness loss. In DOF 2, the system experiences a 15% damage at 35 seconds. The RBFN formulation is capable of identifying and isolating the previously described damage scenario as evidenced by the error functions shown in Fig. 4.14.

4.4.2 Results for 10-DOF Mass-Spring-Damper System with Non-Collocated Input and Output

To validate the proposed formulation further, a 10-DOF system is examined. Much differently than the 2-DOF simulation, input was induced at only three of 10 DOFs (8, 9, and 10), and data is only being observed at another three of the 10 DOFs (1, 5, and 8). The input/output configuration and the damaged DOFs are depicted in Fig. 4.5 and the modal parameters of the healthy system are shown in Table 4.3. Verifying the RBFN on a larger 10-DOF model with non-collocated input and output demonstrates that the proposed formulation is viable for systems without input actuation and

Table 4.3 : Ten DOF System Properties

$\omega(rad/sec)$	$\zeta(\%)$
$\omega_1 = 1.12$	$\zeta_1 = 0.15$
$\omega_2 = 3.19$	$\zeta_2 = 0.09$
$\omega_3 = 6.00$	$\zeta_3 = 0.10$
$\omega_4 = 21.30$	$\zeta_4 = 0.27$
$\omega_5 = 31.12$	$\zeta_5 = 0.39$
$\omega_6 = 41.86$	$\zeta_6 = 0.53$
$\omega_7 = 51.45$	$\zeta_7 = 0.65$
$\omega_8 = 54.44$	$\zeta_8 = 0.68$
$\omega_9 = 72.78$	$\zeta_9 = 0.91$
$\omega_{10} = 127.00$	$\zeta_{10} = 1.59$

sensing at the same locations. The 10-DOF model was subjected to coupled fault scenarios in the presence of the Mexico City (1985 EW) and Jiji (NS) quake cases and uncoupled fault scenarios in the presence of the Mexico City (1985 EW) and Jiji (NS) quake cases; however, due to space limitations only the coupled in time damage scenarios for the Mexico City quake are shown, Fig. 4.17 (left), and the uncoupled in time damage scenarios for the Mexico City quake case are shown, Fig. 4.18 (left).

Once again, the network is trained per section 4.3. The same training input excitations implemented in the previous section 5.1 are applied to DOFs 8, 9, and 10.

During the forced vibration training each degree of freedom is damaged an incremental amount, and the desired stiffness output for the Mexico City training case is shown in Fig. 4.15 for only the damaged DOFs: DOFs 1, 5, and 8. The training input to the network for the Mexico City training case is also shown in Fig.4.16 for damaged degrees of freedom. The dimensionality of the input vector given in 5.1 is also maintained.

In Fig. 4.17 (left), the 10-DOF system is damaged during overlapping time intervals (the coupled damage scenario) 10% during 80-120 seconds, 40% during 60-100 seconds, and 20% during 40-80 seconds for DOFs 1,5, and 8 respectively. The error function is capable of detecting and isolating the damage interval as illustrated by the nonzero error functions shown in Fig. 4.17 (right). In Fig. 4.18 (left), the 10-DOF system is damaged during time intervals which are not overlapping (the uncoupled damage scenario): 10% during 80-100 seconds, 30% during 40-60 seconds, and 20% during 100-120 seconds for DOFs 1,5, and 8 respectively. Again, the RBFN formulation does produce relatively greater nonzero error functions, shown in Fig. 4.18 (right), that corresponds to the aforementioned damage intervals.

4.5 SAIVS Experimental Validation

The ability of the SAIVS device to vary stiffness in real time creates a unique opportunity for experimental validation of online SHM algorithms. The proposed method is validated using the the experimental data involving coupled stiffness variation. Both

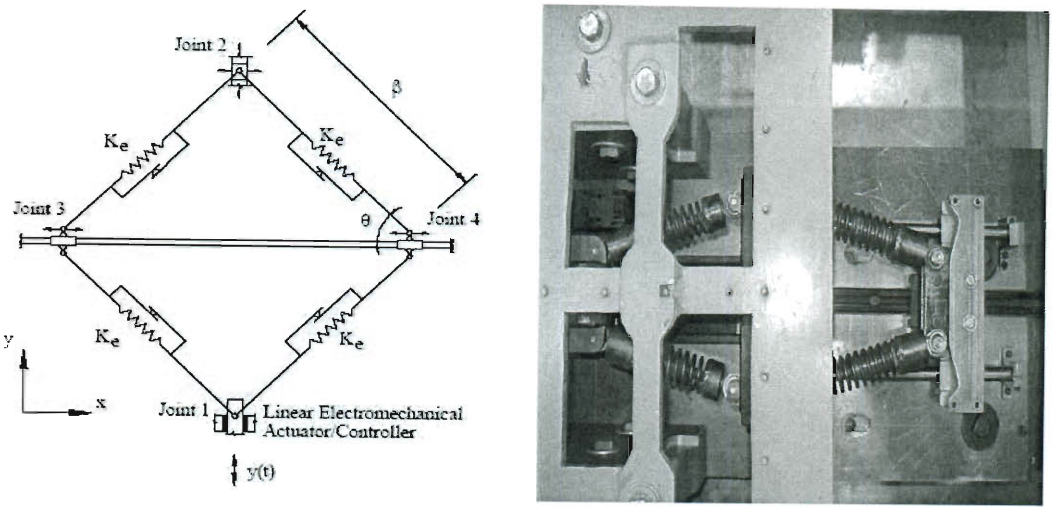

Figure 4.6 : SAIVS Device Design and Implementation

stiffness degradation as well as stiffness recovery are evaluated. A brief overview of the SAIVS device and the testing procedure follows.

4.5.1 Overview of SAIVS Device

The SAIVS device was developed by Nagarajaiah and Mate [79] and has been studied in numerous applications since 1998. A schematic diagram of the device is shown in Fig. 4.6. The device can smoothly vary stiffness in the x direction due to its rhombus configuration of springs. To prevent buckling of the springs their motion is guided by two cross bars, one connecting joint 3 and joint 4 to allow translation in the x-direction, and the other connecting joint 1 and joint 2 to allow translation in the y-direction. The device has two limit states controlled by the angle, θ, of the rhombus shown in the Fig. 4.6 schematic. If the x-direction of the device is placed parallel

to the axis of motion, when $\theta = 90°$ the rhombus produces the weakest limit state of least combined spring stiffness. However, when $\theta = 0°$ the rhombus produces the strongest limit state of maximum combined stiffness. By varying θ between these 2 limit states, stiffness is varied in real time.

Recently, the SAIVS device has been employed in several applications involving seismic disturbance rejection. It has been used by Nagarajaiah and Varadarajan to develop a semi-active tuned mass damper [30]. Also, Narasimhan and Nagarajaiah have successfully coupled the device with a base isolation system in buildings and shown it successful in reducing earthquake induced vibrations [80]. Finally, Nagarajaiah and Saharabudhe have verified a new smart sliding structure that implements the SAIVS device both numerically and experimentally [81]. The SAIVS device application in this study extends the parameter varying capability to structural health monitoring.

4.5.2 Setup and Stiffness Variation

One of the most attractive elements of the proposed formulation is its ability to detect coupled parameter variation. The 2DOF experiment conducted at Rice University by Dharap [75] performs coupled parameter variation and records displacement (using a Linear Variable Differential Transformer, LVDT) in each degree of freedom. The values for mass, m_1 and m_2 are 242.13 Kg and 9.77 Kg, respectively. The initial values for stiffness, $k_1(t_0)$ and $k_2(t_0)$, are considered to be healthy values of 15 KN/m

Table 4.4 : Real Time Stiffness Variation for Experimental Setup

	$0-15$ sec	$15-35$ sec	$35-55$ sec	$55-75$ sec
$k_1(t)$ (KN/m)	15	7.8	15	15
$k_2(t)$ (KN/m)	3.7	5.8	5.8	3.7

and 3.7 KN/m, respectively. A diagonal mass matrix was formed and the traditional tridiagonal stiffness matrix was created using the aforementioned values. Rayleigh damping was used to model the experimental damping and approximated by the relationship, $\mathbf{C}^{damp} = 0.3\mathbf{M} + 0.025\mathbf{K}$. By using the SAIVS device in each degree of freedom to switch between limit states, the stiffnesses are varied in real time according to Table 4.4 and Fig. 4.23 (left).

4.5.3 Results and Discussion

The analytical model of the experimental setup is described by Eq. 4.42 for $n = 2$. The stiffness output is shown in Fig. 4.19 (2nd and 3rd from top), and the desired input training data shown in Fig. 4.20 is used to train the network. Since the testing harmonic excitation is known a priori, site specific response spectra is not needed as in the case of earthquake input. The input used to create the training displacement data is a 1.5 Hz sinusoidal input and is also shown in Fig. 4.19 (top). The dimension of the training input vector is chosen to be in $\Re^{101}$ so that it is of sufficient size for both training and testing.

The effects of the network adding and pruning neurons is shown in Fig. 4.21 during training. The number of hidden layer neurons oscillates in the initial learning iterations. As training continues, the number of hidden neurons ceases to fluctuate. For display purposes, the hidden neurons are plotted for every instant of observation. Training was minimized due to the computational efficiency of the network and the training input being monotonic. The experimental data from the coupled damage test is shown in Fig. 4.22.

Illustrated by a comparison of Fig. 4.23 (left) and Fig. 4.23 (right), the damage error function accurately detects and isolates the stiffness variation. Also, there are some instances where a small magnitude error residual exists when it should strictly be zero. The inability to identify a perfect system model and measurement noise contribute to the magnitude of this error. As with most formulations, to ensure robust FDI it is important that this baseline deviation is small relative to the error function.

It should also be noted, that this error residual in Fig. 4.23 is unique with respect to the previous validations in this study because its magnitude is primarily negative. It has been shown in section 4.2 that the sign of the error function is somewhat arbitrary as long as $r_j \rightarrow 0$, for $\mathbf{F}_m \rightarrow \mathbf{0}$. It should also be noted that the magnitude of r_j is scaled by the weights, α_j. Proper scaling of α_j may pose a possible extension to future fault quantification applications.

4.6 Summary

A novel health monitoring formulation capable of isolating coupled and uncoupled stiffness variation, damage and recovery, has been proposed. It was also illustrated that for the generalized training procedure described in this study, coupled and uncoupled damage cases could be sufficiently detected and isolated. Some of the merits of the formulation include real time detection and generalized offline training. The algorithm has been validated for systems experiencing damage during earthquake excitations, larger systems with non-collocated input and output with damage in only a few members, and experimental data from stiffness variation tests in the presence of harmonic excitation performed using the SAIVS device at Rice University. The developed method has significant potential as evident from the numerical and experimental validations.

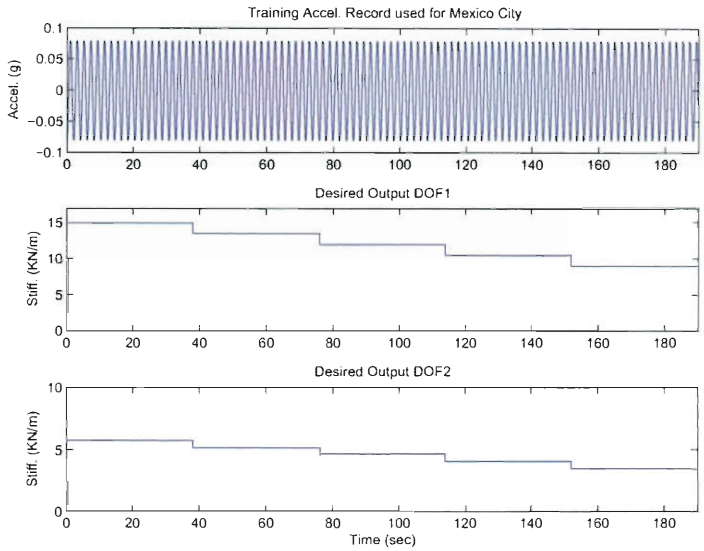

Figure 4.7 : Training Acc. and Desired Stiffnesses Output for Mexico City

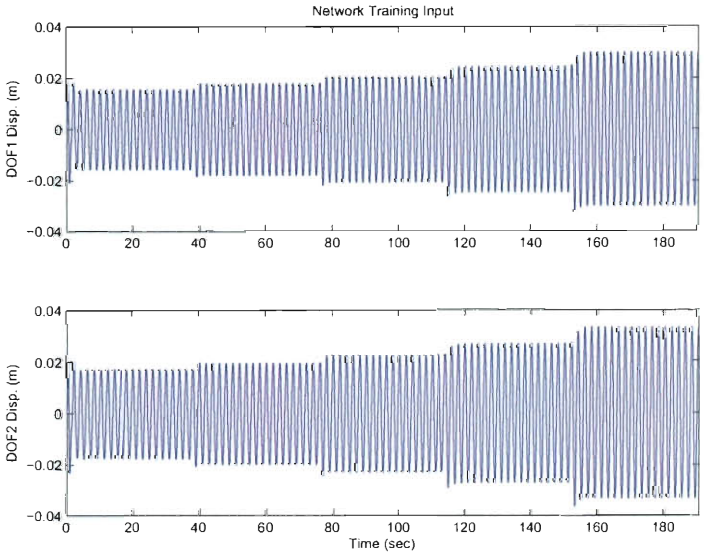

Figure 4.8 : Network Training Input Produced by Acc. in Fig. 4.7 (top)

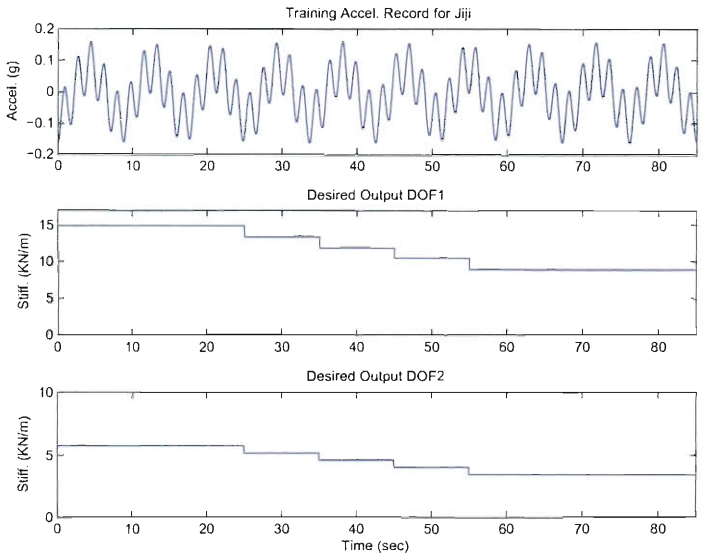

Figure 4.9 : Training Acc. and Desired Stiffnesses Output for Jiji

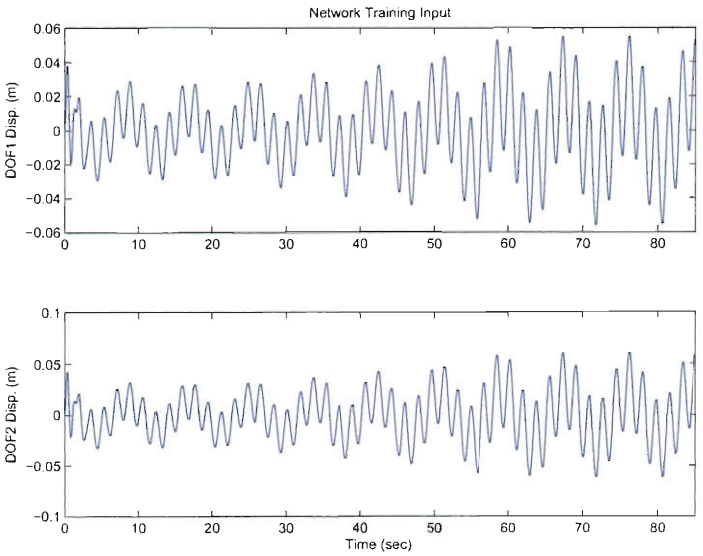

Figure 4.10 : Network Training Input Produced by Acc. in Fig. 4.9 (top)

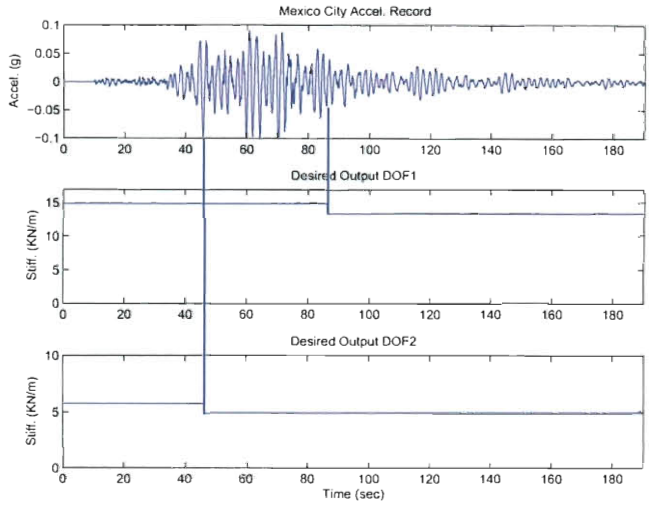

Figure 4.11 : Mexico City Earthquake Record with Coupled Real Time Stiffness Loss

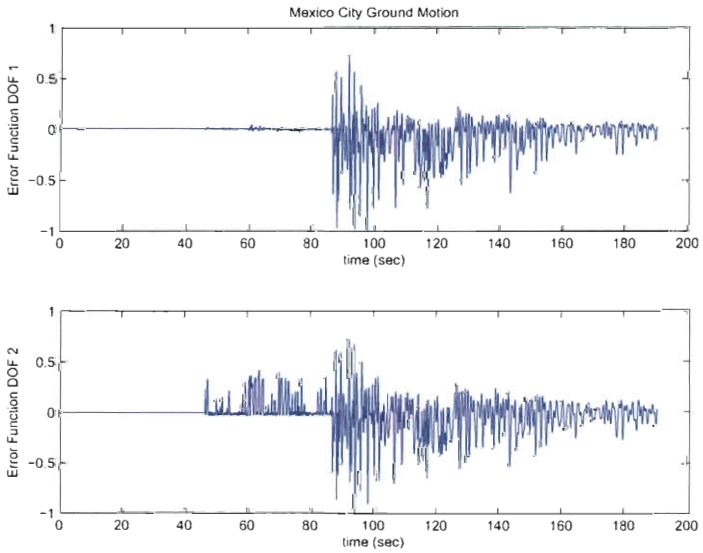

Figure 4.12 : Augmented RBFN Detection Filter Error Function for Mexico City Case

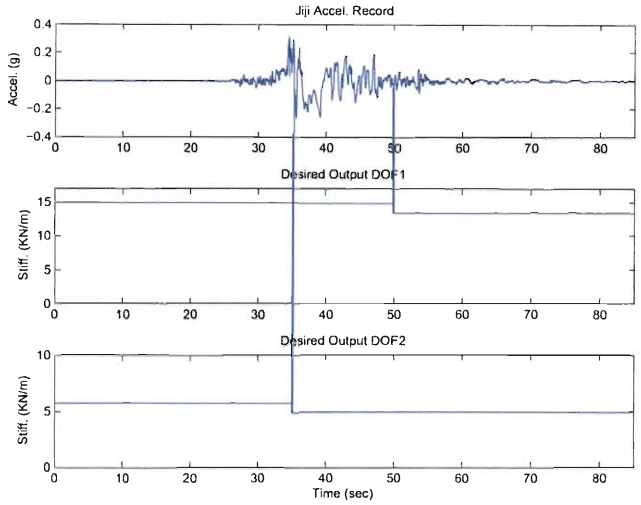

Figure 4.13 : Jiji Earthquake Record with Coupled Real Time Stiffness Loss

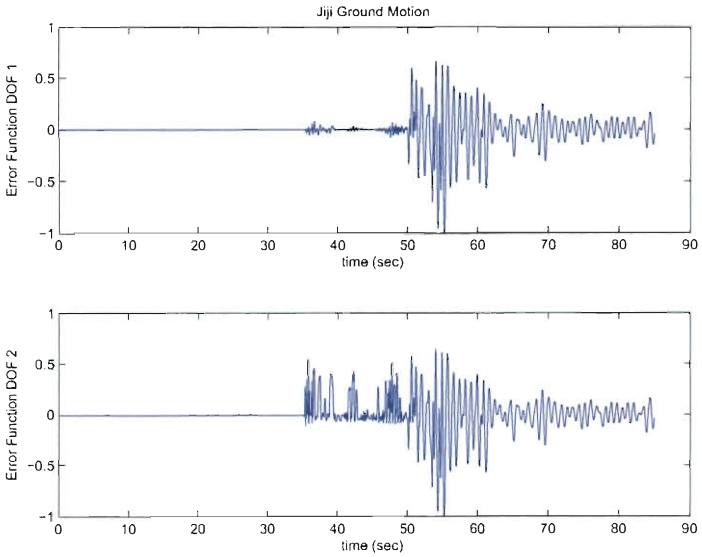

Figure 4.14 : Augmented RBFN Detection Filter Error Function for Jiji Case

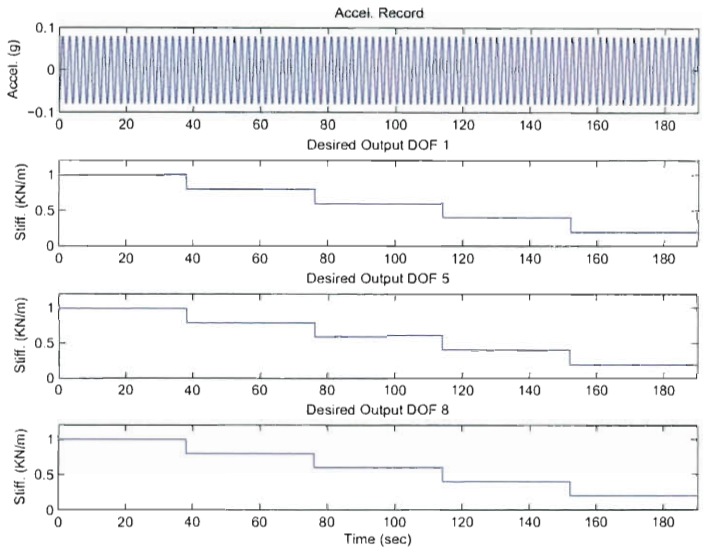

Figure 4.15 : Training Acc. and Stiffnesss Change in 10-DOF Structure for Mexico City Case

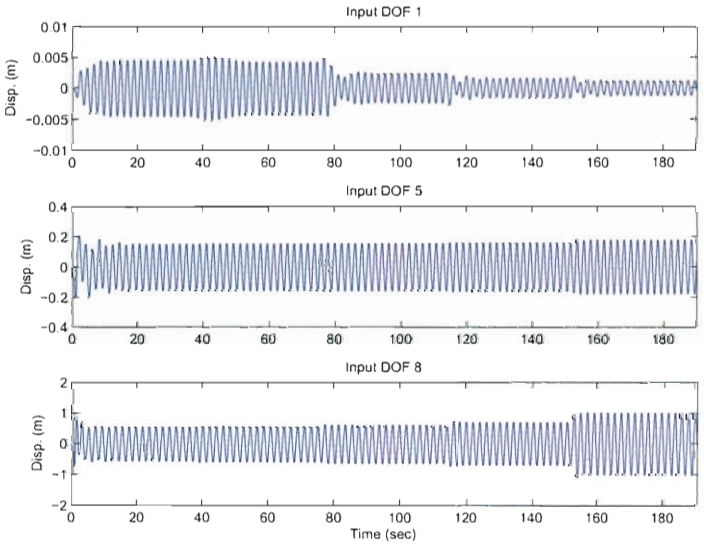

Figure 4.16 : Network Training Input at Selected DOFs Produced by Acc. in Fig. 4.15 (top)

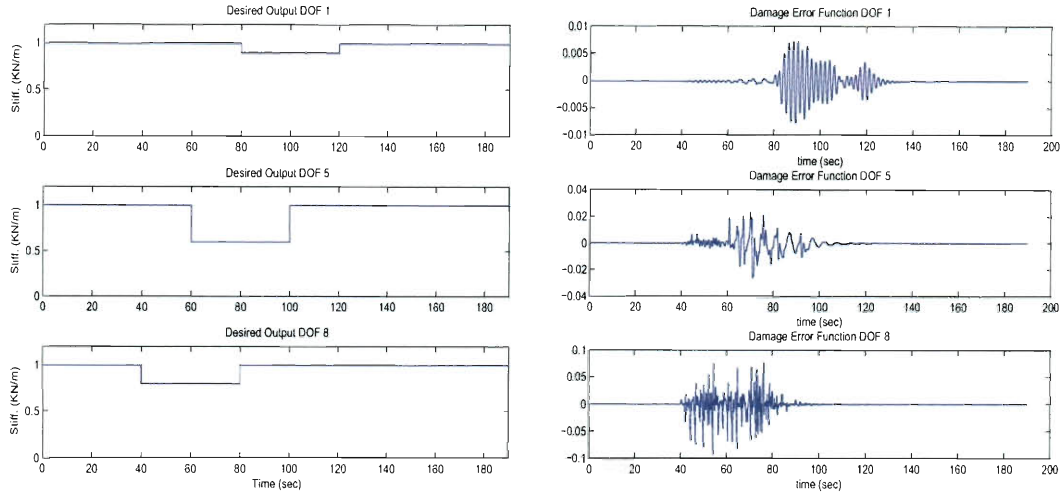

Figure 4.17 : Coupled Stiffness Change (left) and Error Function Detection (right) for Mexico City Case

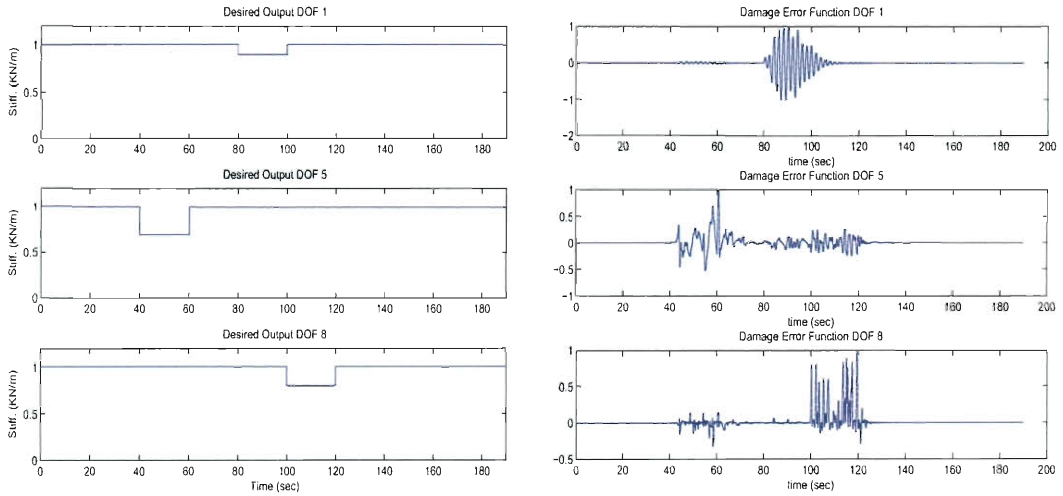

Figure 4.18 : Uncoupled Stiffness Change (left) and Error Function Detection (right) for Mexico City Case

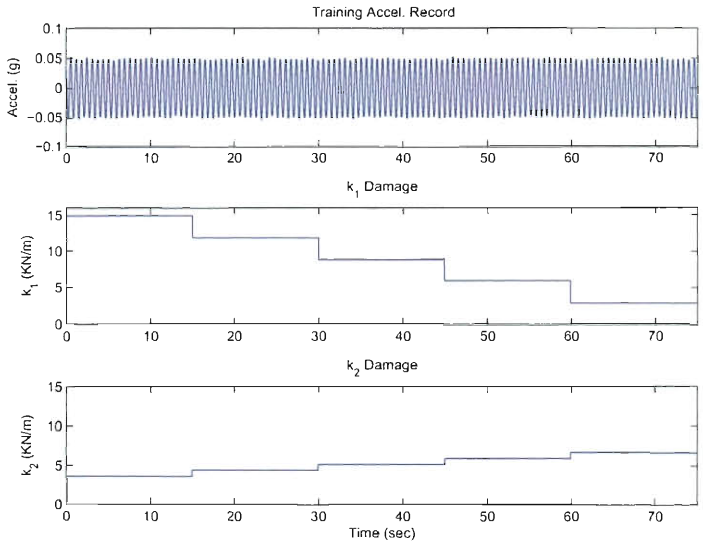

Figure 4.19 : Training Acc. and Desired Stiffnesses Output for Experimental Validation

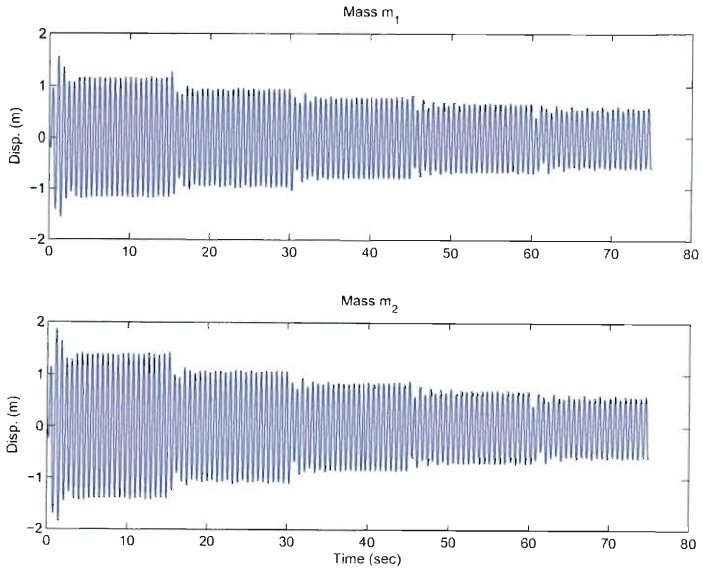

Figure 4.20 : Network Training Input Produced by Acc. in Fig. 4.19 (top)

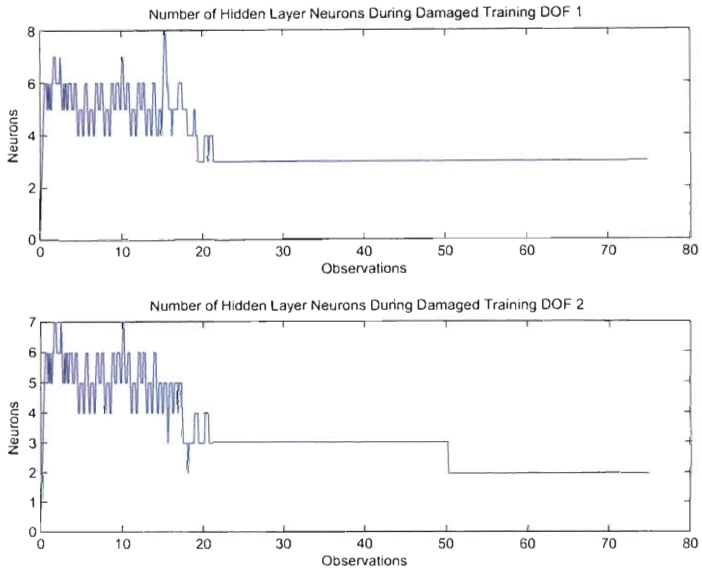

Figure 4.21 : Neuron Growth and Pruning during Training

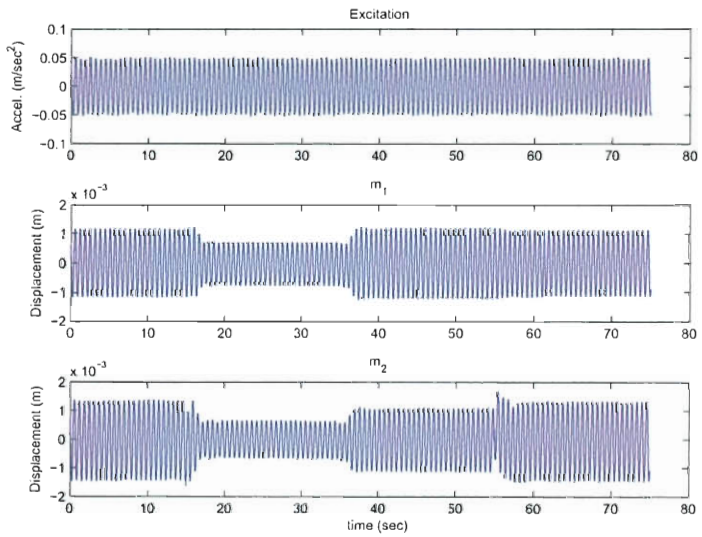

Figure 4.22 : Testing Excitation and Response Displacements of Mass m_1 and m_2

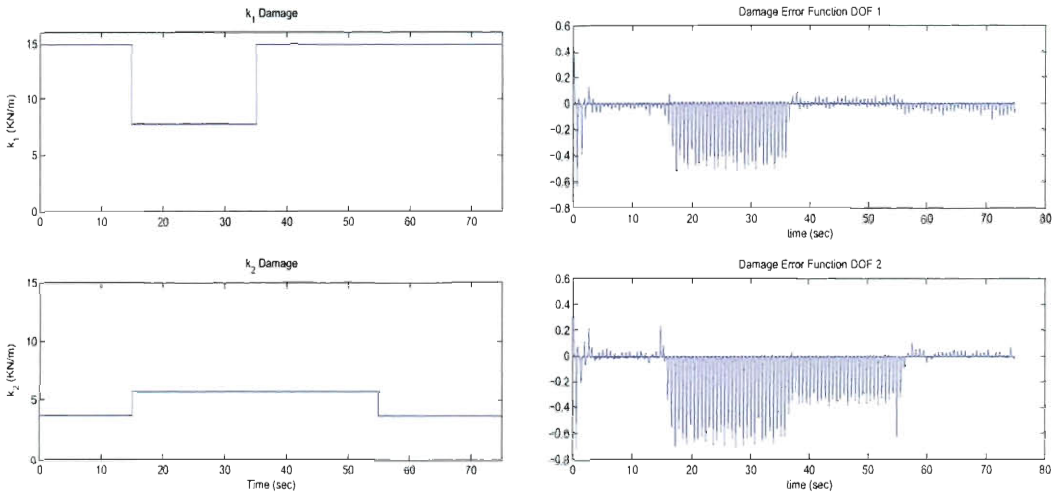

Figure 4.23 : Coupled Stiffness Change (left) and Error Function Detection (right)

Chapter 5

ADAPTIVE DYNAMIC INVERSION USING RADIAL BASIS FUNCTION NETWORKS

Previously, the pattern recognition capabilities of a RBFN were utilized to perform FDI in real time. In this chapter, the pattern recognition capabilities of a RBFN will be used to model the behavior of a Magnetorheological (MR) damper in real time to improve the feedback control performance of the semi-active device. As mentioned in Ch. 1, a MR damper exhibits a nonlinear relationship between voltage input to the device and the actuator force that is delivered by the MR damper. When a Bouc-Wen hysteresis model is used to describe the voltage-force relationship, there does not exist a closed form inverse model which maps a particular force to an input voltage. The RBFN is used to generate the inverse model such that the a closed loop system with MR damper force feedback is effectively linearized.

5.1 Motivation

Because MR dampers induce hysteretic nonlinearity into a system, feedback control algorithms for disturbance rejection in civil systems are often limited to switching/thresholding methods. By implementing a RBFN into the feedback control loop to effectively linearize the MR actuator dynamics, the application of standard Linear

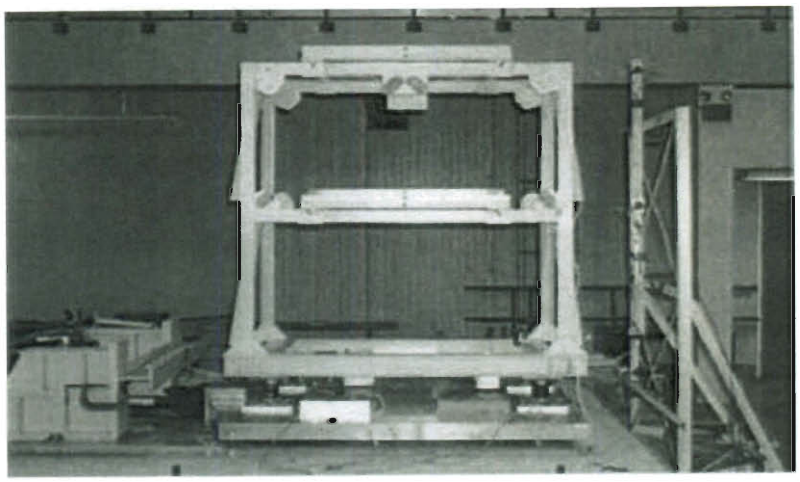

Figure 5.1 : Two Story Scaled Structure with MR Damper Acting as Base Isolator

Time Invariant (LTI) feedback control algorithms is rendered possible. The RBFN strives to represent an inverse model of the actuator at every time step. It does this by training itself in real time to reduce the tracking error between a desired controller force, calculated from LTI methods, and the actual MR damper force supplied to the system. This results in a semiactive control formulation for an MR damper that can smoothly track a commanded control force, as opposed to conventional switching/thresholding methodologies.

The formulation is validated on a two story scaled building system, that is base isolated with an MR damper in the ground floor. The structural system and MR damper model were originally modeled and tested by Sahasrabudhe [82] and shown in Fig. 5.1. A Bouc-Wen hysteresis model of an MR damper captures the nonlinear behavior present in the device and demonstrates the advantages of the RBFN lin-

earization formulation in the simulations. The performance of the system with the RBFN adaptive linearization is compared to the system with passive-off and passive-on controllers. It is evident that the RBFN is necessary and enhances performance with respect to existing passive-off and passive-on control formulations.

5.2 Network Architecture for Inverse Modeling

Recalling that neural networks are well suited for pattern recognition and input-output mapping applications, it follows that they would be instrumental in the generating an inverse model of an MR damper. The application of the RBFN algorithm, introduced in Ch. 2, enables this construction and adaptation of such a model in real time. The real time adaptation reduces the need for offline training. The RBFN inverse model is also robust to a wide range of input excitations to the system and can adapt its level of performance.

Regarding initialization, the EMRAN parameters for the network were selected using the GA optimization scheme discussed in Section 2.5. Since the output is scalar, the fitness function maximized is, $-e^2 = -(f - \widehat{f})^2$, to ensure that the error between the desired control force, f, and the MR damper force, $\widehat{f}$, are close to zero. The values produced by the GA optimization can be found in Table 5.1.

Table 5.1 : EMRAN Initialized Parameters

ϵ_{max}	ϵ_{min}	ϵ_2	ϵ_3	γ	κ	N_w	S_w	δ	P_0	q
0.75	0.01	0.0005	0.0005	0.992	0.6827	45	187	0.08	1.1	0.0005

5.3 Semiactive Control using Dynamic Inversion

Since the early 90s, Dynamic Inversion (DI) control strategies have been explored in the field of aerospace engineering [83] [84]. The theoretical motivation involves linearizing the feedback tacking error to compensate for nonlinear dynamics present in a system [85]. Several application have included tracking angle of attack of both the F-18 [86] and X-38 aircrafts [87]. Recently, Ali has applied an optimal DI strategy for semiactive control of bridges [88] and active vibration control of beams [89]. The proposed algorithm in this chapter extends the previous work to include an adaptive framework that does not have fixed error gains. The RBFN provides a method to enhance, in real time, semiactive control performance of buildings instrumented with MR dampers.

5.3.1 Modeling of Scaled Structure and MR Damper

The structural model used for the simulations in this study is based on a 1:5 scale building shown in Fig. 5.1. The MR actuator is placed between the base shaking table and the ground floor of the structure to act as a base isolator. Restoring springs of 720 N/cm (410.55 lbf/in) were also attached from the shaking table to the ground

floor. The beams and columns in the floors are of dimensions $6.35 \times 6.35 \times 0.47$ cm $(2.5 \times 2.5 \times 0.185$ $in)$, and the base beams are standard $W4 \times 13$ sizing. The weight of each floor is 5.8 kN (1300 lbf), however the weight of the base is 5.44 kN (1220 lbf). The span of each floor is 1.47 m (57.9 in) and has a height of 0.74 m (29.1 in). The mass, $\mathbf{M}$ (lbf), stiffness, $\mathbf{K}$ (lbf/in), and damping, $\mathbf{C}^{damp}$ $(\frac{lbf-sec}{in})$, matrices of the base isolated structure were found by Sahasrabudhe [82] to be:

$$\mathbf{K} = \begin{bmatrix} 47517 & -37517 & 0 \\ -37517 & 63868 & -26351 \\ 0 & -26351 & 26351 \end{bmatrix} \quad \mathbf{C}^{damp} = \begin{bmatrix} 11.81 & -10.38 & 0 \\ -10.38 & 20.76 & -10.38 \\ 0 & -10.38 & 10.38 \end{bmatrix} \tag{5.1}$$

and

$$\mathbf{M} = \begin{bmatrix} 1220 & 0 & 0 \\ 0 & 1400 & 0 \\ 0 & 0 & 1400 \end{bmatrix} \tag{5.2}$$

Once $\mathbf{M}$, $\mathbf{C}^{damp}$ and $\mathbf{K}$ are obtained, the open loop response can be simulated from the controllable canonical state space representation with full state feedback shown below in Eq. 5.3.

$$\dot{\mathbf{x}}_{6\times1}(t) = \mathbf{A}_{6\times6}\mathbf{x}_{6\times1}(t) + \mathbf{B}_{6\times1}u(t) \tag{5.3}$$

$$\mathbf{y}_{6\times1}(t) = \mathbf{C}_{6\times6}\mathbf{x}_{6\times1}(t)$$

The state variable, $\mathbf{x}_{6\times1} = [\mathbf{x}_{3\times1} \quad \dot{\mathbf{x}}_{3\times1}]^T$, consists of relative displacement, $\mathbf{x}_{3\times1} = [x_b \quad x_1 \quad x_2]^T$, and relative velocity, $\dot{\mathbf{x}}_{3\times1} = [\dot{x}_b \quad \dot{x}_1 \quad \dot{x}_2]^T$, for the base, first floor, and second floor of the structure respectively. $u(t)$ is the input acceleration and $\mathbf{A}$, $\mathbf{B}$, $\mathbf{C}$, and are state space matrices defined as follows:

$$\mathbf{A}_{6\times6} = \begin{bmatrix} \mathbf{0}_{3\times3} & \mathbf{I}_{3\times3} \\ -\mathbf{M}_{3\times3}^{-1}\mathbf{K}_{3\times3} & -\mathbf{M}_{3\times3}^{-1}\mathbf{C}_{3\times3}^{damp} \end{bmatrix}$$

$$\mathbf{B}_{6\times1} = \begin{bmatrix} \mathbf{0}_{3\times1} \\ \mathbf{\Gamma}_{3\times1} \end{bmatrix}$$

and

$$\mathbf{C}_{6\times6} = [\mathbf{I}_{6\times6}]$$

where $\mathbf{\Gamma}$ is a vector of unity influence coefficients.

Because the structure is of scaled form and the input acceleration records acquired were from recorded, full scale earthquakes, the time history input is scaled according to Table 5.2. The time step of the earthquake acceleration records is modified for a 1:5 scale model ($l_r = \frac{1}{5}$).

Table 5.2 : Time Step Scaling

	Full Scale	Scale Factor	Model Scale
Δt	0.005	$\sqrt{l_r} \rightarrow \frac{1}{\sqrt{5}}$	0.002

The MR Damper modeled in this study was produced by Lord Corporation, in Cary, North Carolina. The damping action is produced by passing fluid through an

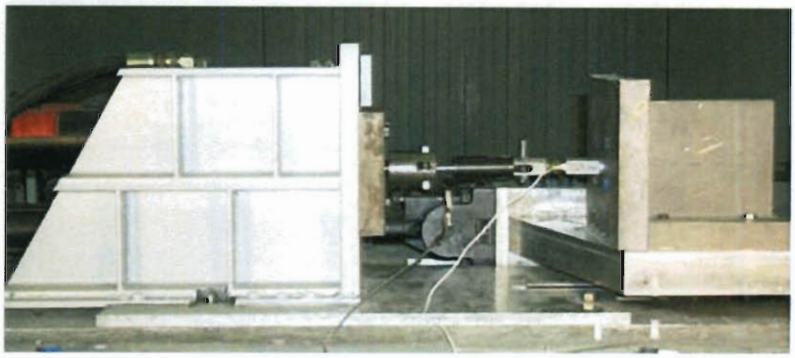

Figure 5.2 : MR Damper Setup for Modeling

annular orifice. As the viscosity of the fluid changes, so too does the force delivered by the actuator. The response time of the MR fluid to applied voltage is 25 milliseconds, and this is later accounted for by including first order voltage dynamics in the model. The same MR damper and a similar model on which the one in this chapter is based has been tested and implemented in [90]. A picture of the test setup for modeling the Lord Corporation damper is shown in Fig. 5.2.

Using the test data, a Bouc-Wen model based on the one proposed by Sahasrabudhe [91] is implemented to capture the hysteresis behavior present in the MR damper. The model has been modified and scaled to have a peak force output of 3.8 kN (853 lbf) at 0 $Volts$ to approximately 14 kN (3,143 lbf) at 5 $Volts$. The force output by the MR damper is described by the following equation:

$$F_{MR} = C_{MR}\dot{x}_b + \alpha z \tag{5.3}$$

where α and C_{MR} are given as:

$$\alpha = \alpha_a + \alpha_b \tag{5.4}$$

$$C_{MR} = C_a + C_b \tag{5.5}$$

where $\alpha_a = 1.8725 \times 10^4\ N/cm$, $C_a = 4.40\ \frac{N-sec}{cm}$ and

$$\alpha_b = \alpha_1 v_c \tag{5.6}$$

$$C_b == C_1 v_c \tag{5.7}$$

$$\dot{v}_c = -\eta(v_c - v_a) \tag{5.8}$$

where $\alpha_1 = 9.9616 \times 10^3\ \frac{N}{cm-V}$, $C_1 = 4.40\ \frac{N-sec}{cm-V}$, $\eta = 50\ sec^{-1}$, v_a is the voltage supplied to the current driver of the MR damper, and v_c is the voltage supplied by the current driver to the MR damper itself. Eq. 5.8 describes the first order voltage dynamics which affect the control force produced by the damper. The only remaining unknown from Eq. 5.3 is the Bouc-Wen hysteresis variable, z. This is obtained by solving the following differential equation:

$$\dot{z} = -\gamma \left|\dot{x}_b\right| z \left|z\right|^{n-1} - \beta \dot{x}_b \left|z\right|^n + A\dot{x}_b \tag{5.9}$$

where x_b is the relative displacement of the damper from the ground floor of the structure to the shaking table and $n = 1$. The constant A which has a value of 12 and is associated with the yield displacement. Constants γ and β both have values of 30 cm^{-1}. The complete model is integrated and the MR damper response to sinusoidal stroke motions is calculated using standard Runge-Kutta methods. Typical

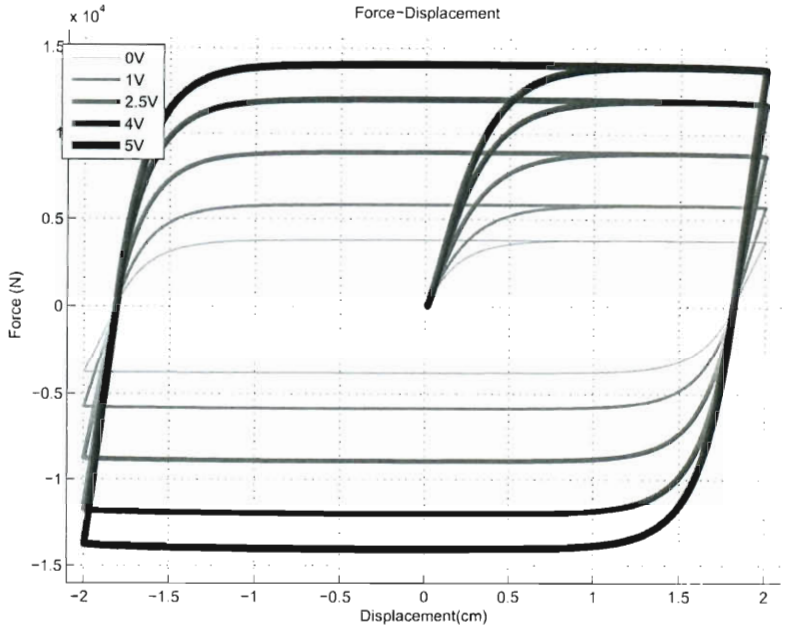

Figure 5.3 : MR Model Typical Force-Displacement Loops

simulation results for the model output for varying levels of voltage can be found in Fig. 5.3 and Fig. 5.4.

5.3.2 Controller Design

The controller design scheme uses and inverse adaptive model of the MR damper actuator to effectively linearize its dynamics. The RBFN algorithm introduced in Ch. 2 is implemented as the inverse model and learns in real time through a process of adaptive system identification. A desired control force, f, is computed using linear theory, in this case an H_2/LQR optimal controller is calculated. This force, f, is compared in real time to the actual force, $\widehat{f}$, produced by the MR damper. The

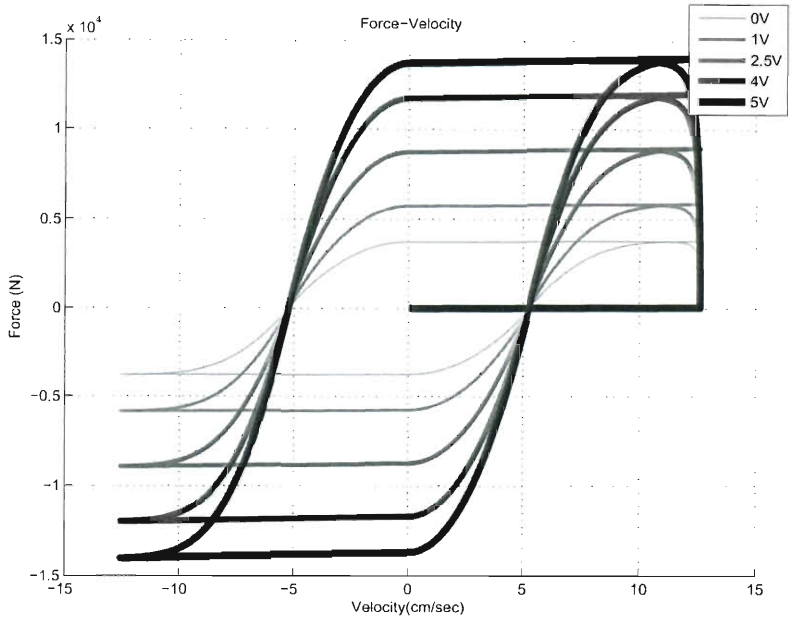

Figure 5.4 : MR Model Typical Force-Velocity Loops

error between the two forces, $e = f - \widehat{f}$, is fed back to the RBFN. By attempting to drive the error to zero, the RBFN filters out the nonlinear dynamics present in the state response. A block diagram of the control algorithm implemented is presented in Fig. 5.5.

For the system presented in Section 5.3.1 full state feedback is assumed. Because this assumption is made, the H_2/LQR control gains can be made arbitrarily large such that the system response goes to zero arbitrarily fast for high gain selections. To avoid this, the input and state weight values were scaled by $R = 1 \times 10^4$ and $Q = 2 \times 10^{-4}$, respectively so that the controller gains derived would not be high gain. High gain controllers combined with the RBFN-DI formulation produced numerically

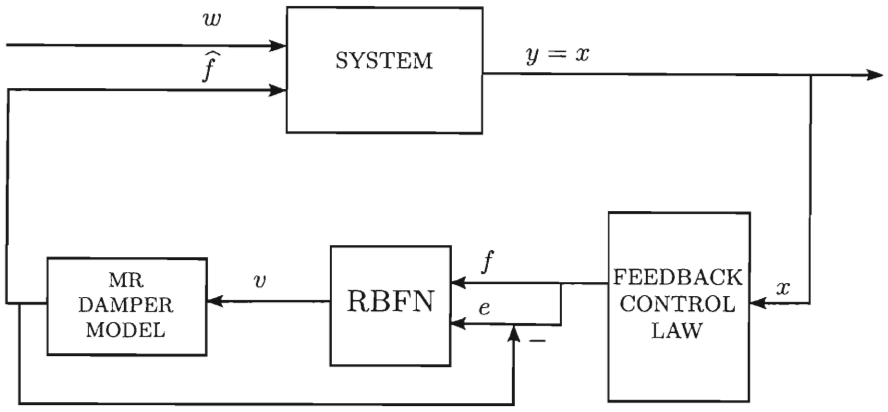

Figure 5.5 : Control Design with RBFN Dynamic Inversion

inconsistent results in most cases. Also, by designing a lower gain controller, the force supplied to the base of the structure was within the range of forces that the MR damper is capable of delivering.

5.4 Results for Impulse Excitation

The experimentally modeled system is subjected to a base impulse of sufficient magnitude to engage the nonlinear behavior of the MR damper. The formulation is implemented to vary the voltage sent to the damper in a continuous manner while tracking the H_2/LQR control force. The effect of the controller can be seen in the time history displacement of the second floor and the base as illustrated in Fig. 5.6 and Fig. 5.7. Since a lower gain controller was designed, the RBFN-DI method shows only moderate improvements when compared to the open loop system with respect to both RMS displacement and peak floor displacement. Recall that the focus of

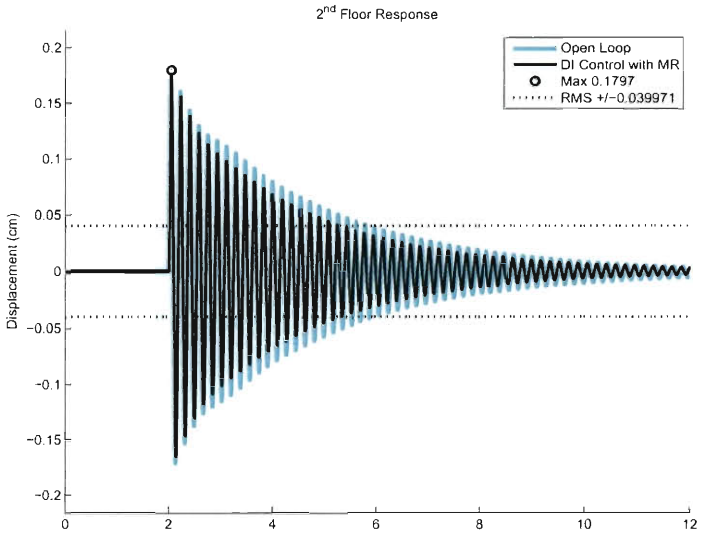

Figure 5.6 : Open and Closed Loop 2^{nd} Floor Response for Impulse Excitation

this exercise involving impulse excitation is to display the tracking capability of the method. Seeking larger reductions in the time history response will be paramount when applying the RBFN-DI method for quake response in the next section.

The tracking error is reduced as time continues. The results for the tracking performance are displayed by comparing the control force required by the H_2/LQR, and the actual control force delivered to the system by the MR damper in Fig. 5.8. The error between the two signals is plotted in Fig. 5.8 (bottom) as a function of time. It is clear that as time continues the error goes to zero as the force produced by the RBFN-DI method drives the MR damper control force to the desired H_2/LQR input.

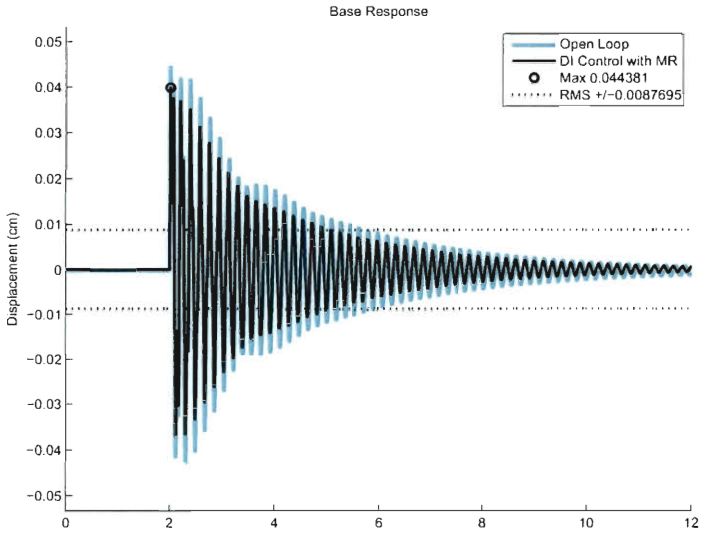

Figure 5.7 : Open and Closed Loop Response for Impulse Excitation

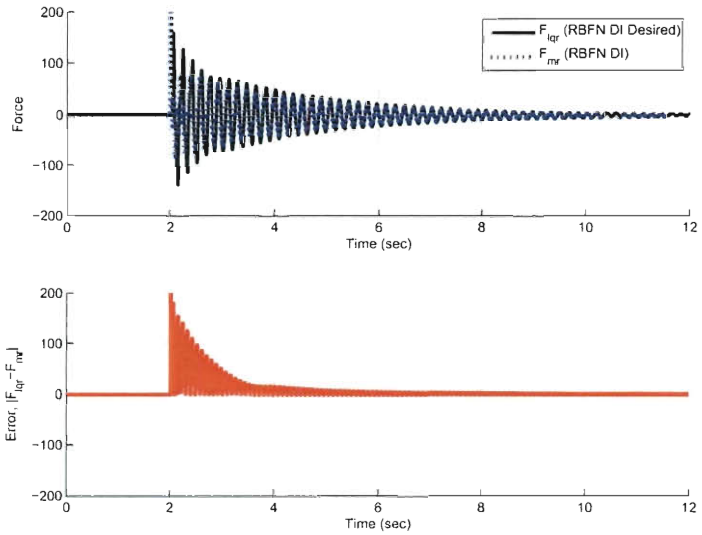

Figure 5.8 : Control Force Tracking and Error Convergence

5.5 Results for Earthquake Excitation

The two story base isolated system is subjected to six earthquake ground motions: the Kobe earthquake, both Fault Normal (FN) and Fault Parallel (FP) records, the El Centro earthquake, both FN and FP records, and the Sylmar earthquake, both FN and FP. The effect of the controller is displayed by graphical comparisons of (1) the passive-on condition in which the MR damper has constant voltage of zero, (2) the passive-off condition in which the MR damper has constant voltage of five, and (3) the application of H_2/LQR control with RBFN Dynamic Inversion. For selected quakes, comparison plots are shown in both the time domain for the 2^{nd} floor as well as force-displacement comparisons in the base floor. Each plot also shows a time history response of the open loop system (or system without any semiactive control) to provide an absolute reference point for performance comparison.

The second floor displacement time histories for the Sylmar FP, El Centro FN, and Kobe FP records shown in Fig. 5.9, Fig. 5.11, and Fig. 5.13 respectively. Also, the second floor acceleration time histories for the Sylmar FP, El Centro FN, and Kobe FP records shown in Fig. 5.10, Fig. 5.12, and Fig. 5.14 respectively. Computed RMS displacements and accelerations, in addition to peak displacements and accelerations, are printed and displayed graphically on the figures themselves to provide grounds for numerical comparisons of performance. It is also important to note that for the sake of quick reference each time history figure displays the control method that performed the worst (in terms of RMS response) at the top of the figure and best at the bottom.

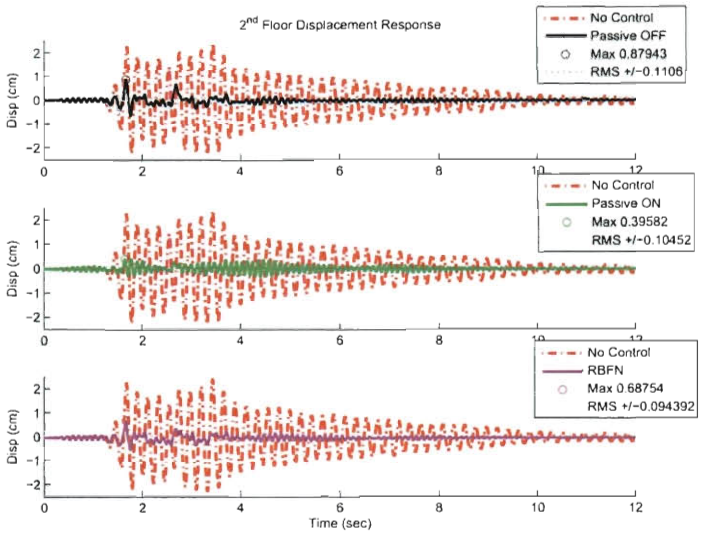

Figure 5.9 : Second Floor Displacement for Sylmar FP Ground Motion

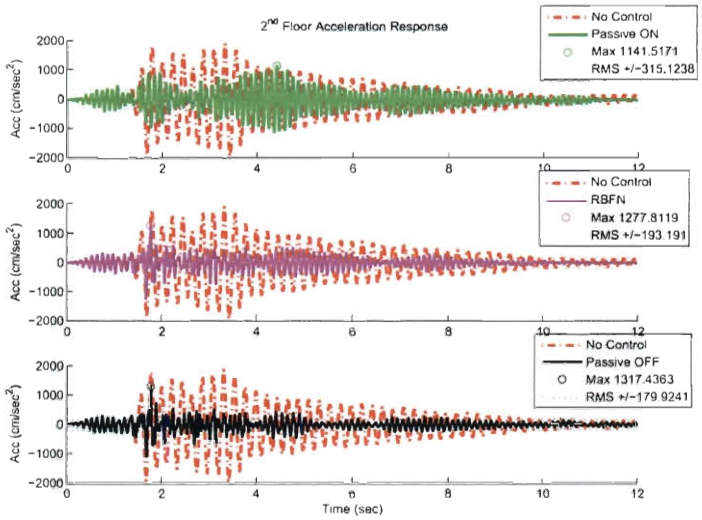

Figure 5.10 : Second Floor Acceleration for Sylmar FP Ground Motion

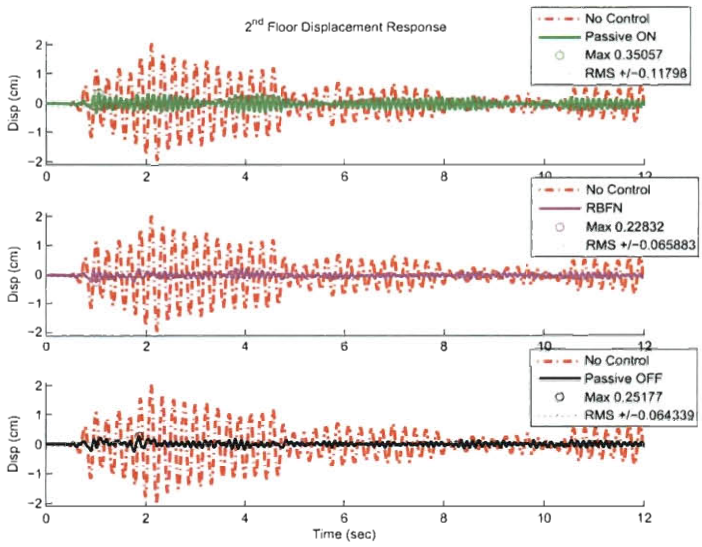

Figure 5.11 : Second Floor Displacement for El Centro FN Ground Motion

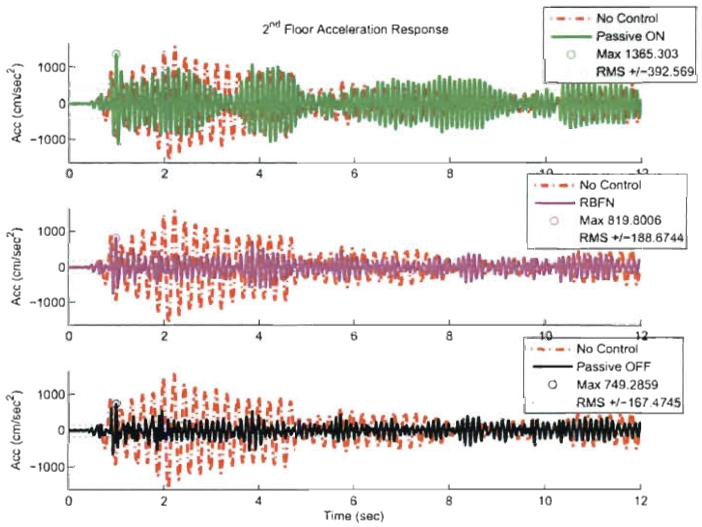

Figure 5.12 : Second Floor Acceleration for El Centro FN Ground Motion

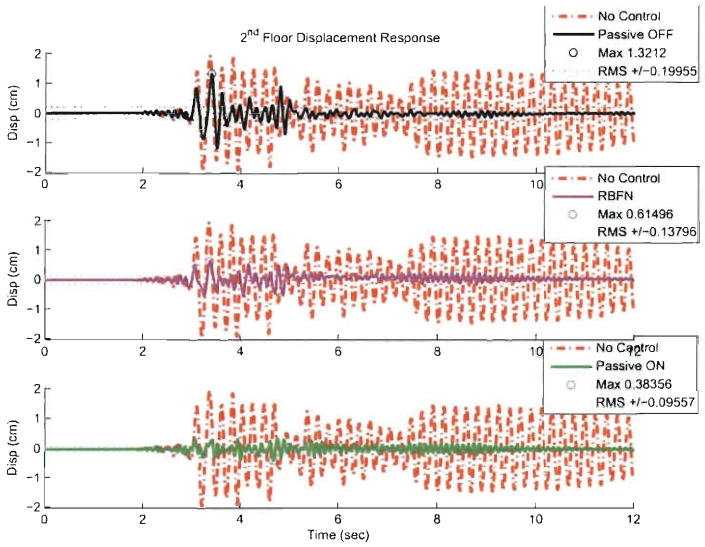

Figure 5.13 : Second Floor Displacement for Kobe FP Ground Motion

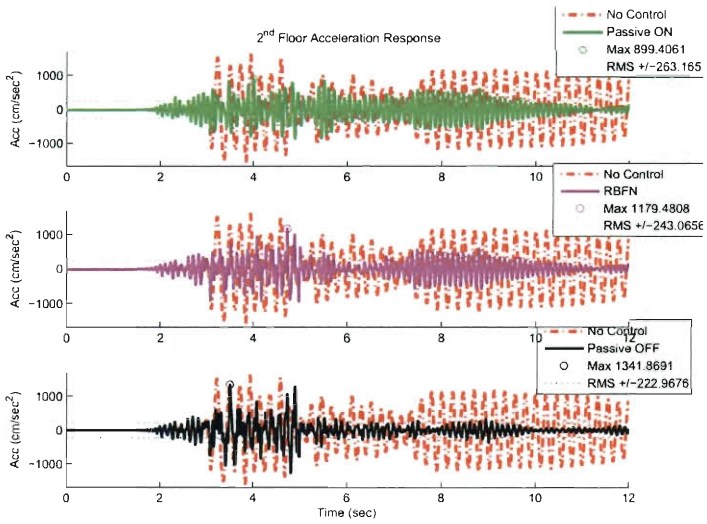

Figure 5.14 : Second Floor Acceleration for Kobe FP Ground Motion

The true benefit of the RBFN-DI controller is illustrated by the performance enhancements with respect to second floor displacement and acceleration. In two of the selected cases, Sylmar FP displacement and Kobe FP acceleration, the RBFN-DI method outperforms the passive-off and passive-on cases. This is feasible for two reasons. The first reason being that the base isolation induced by a static viscous damper can often induce higher than anticipated responses in the higher floors due to "over-performance" in the base. This topic will also be addressed when examining the force-displacement loops. Also, since the RBFN-DI methodology is based on driving the system toward active control, the disturbance of all the floors (not just the base) is accounted for in the control design. This is why the performance fluctuates but is never worse that the passive-off or passive-on condition at the second floor.

The force-displacement loops produced at the base of the structure are also shown in Fig. 5.15, Fig. 5.16, and Fig. 5.17 to show the efficacy of the MR damper as a base isolator. The general trend of the selected results is that the RBFN-DI method encompasses a larger loop without injecting extremely large sustained forces into the base of the building. The area encompassed by the RBFN-DI loops significantly dissipates more energy when compared to the passive-off implementation of the damper, but less than the passive-on condition. Although some slightly larger displacements are allowed by the RBFN-DI method, it can be argued that when considering the control performance over all floors of the structural system, the proposed RBFN-DI controller would be preferable over a passive-on damper. This can also be regarded

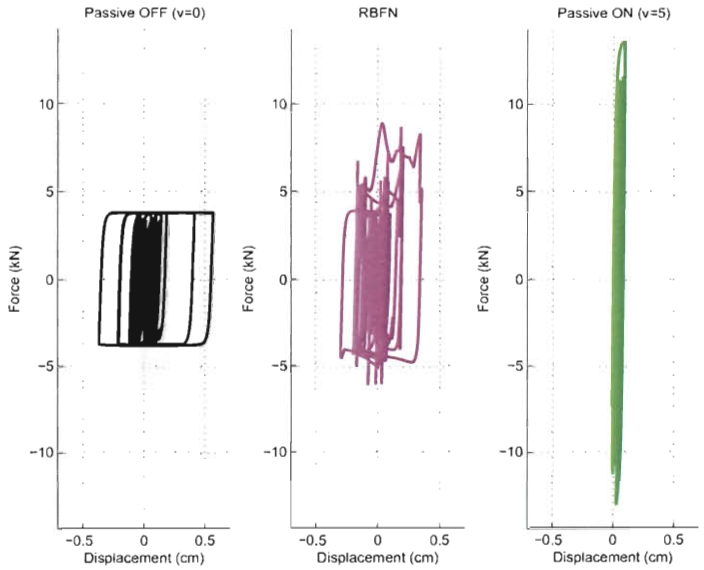

Figure 5.15 : Efficacy of MR Damper Control for Base Isolation: Sylmar FP Ground Motion

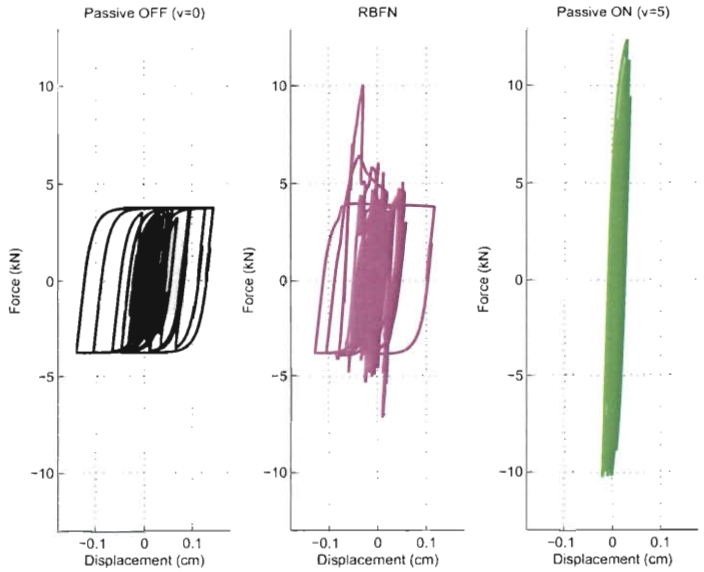

Figure 5.16 : Efficacy of MR Damper Control for Base Isolation: Sylmar FN Ground Motion

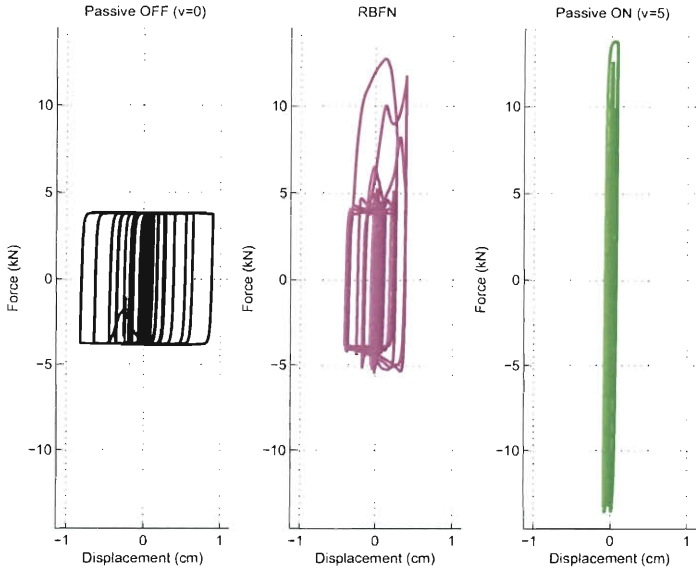

Figure 5.17 : Efficacy of MR Damper Control for Base Isolation: Kobe FP Ground Motion

as an example of a particular case where the passive-on damper over-performs.

Finally, Fig. 5.18, Fig. 5.19, and Fig. 5.20 highlights the ability of the RBFN-DI technique in tracking the desired H_2/LQR force. The figures show the evolution of the force tracking along with the amount of neurons in the hidden layer of the RBFN as a function of time. This force tracking is made possible because the RBFN is altering the dynamics of the closed loop system such that the MR damper can track the linear control force. Also, in Fig. 5.21 the voltage input from the RBFN is shown to fluctuate smoothly in between the maximum voltage values of the MR damper.

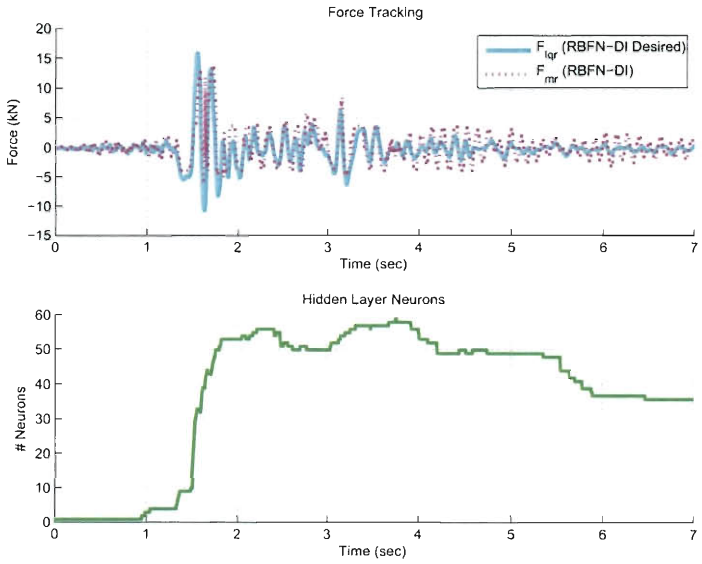

Figure 5.18 : RBFN-DI Force Tracking for Sylmar FN Ground Motion

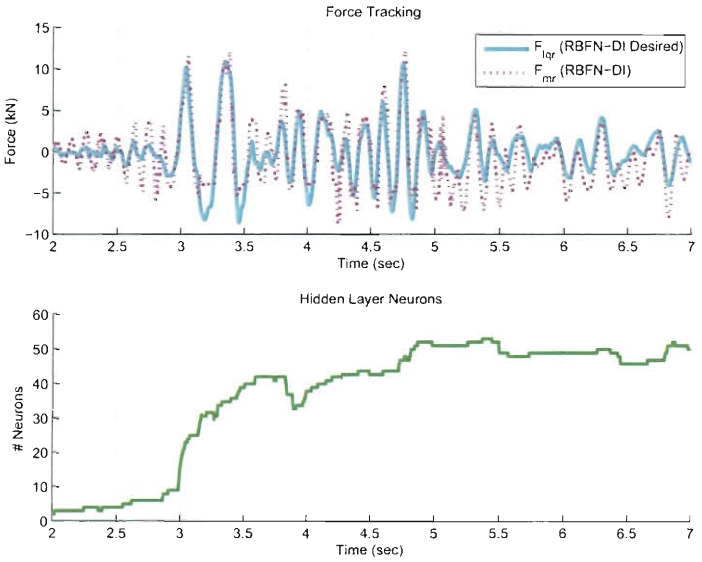

Figure 5.19 : RBFN-DI Force Tracking for Kobe FP Ground Motion

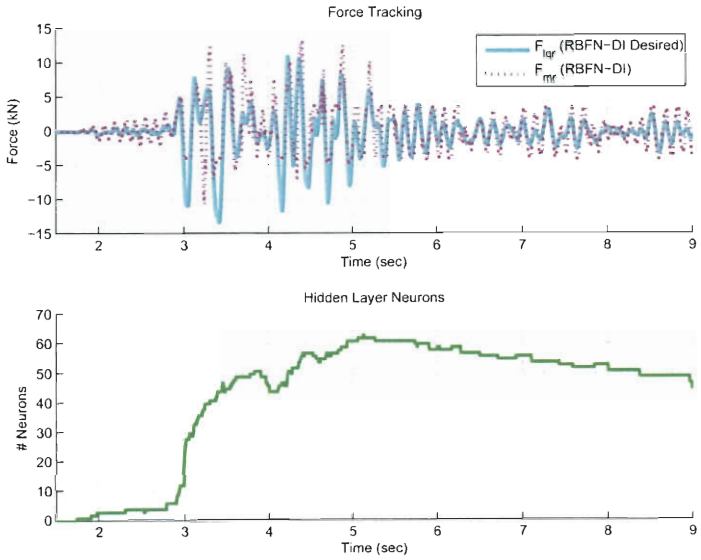

Figure 5.20 : RBFN-DI Force Tracking for Kobe FN Ground Motion

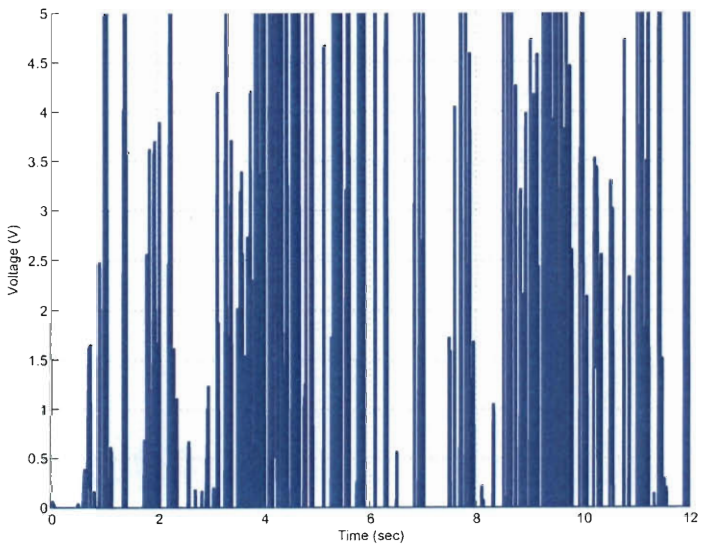

Figure 5.21 : RBFN-DI Voltage Input to MR Damper for El Centro FN Ground Motion

5.6 Summary

A neural network formulation is developed to perform real time, dynamic inversion for semiactive control of a MR damper. The MR damper, which was modeled and tested at Rice University, has a voltage to force relationship that is inversely modeled by an adaptive learning RBFN. This online linearization technique enables the implementation of an H_2/LQR control force that is not usually applicable for systems with nonlinearity. The method is validated on a scaled two story model that was fabricated and tested in the Rice laboratory with the MR damper acting as a base isolator. The control performance of the adaptive RBFN Dynamic Inversion method is a viable technique for semiactive control as evidenced from the comparisons to passive-off and passive-on control. Significant performance improvements were seen in the second floor with respect to RMS displacements/accelerations and peak displacement/accelerations while more flexibility was allowed in the base. The force tracking error was shown to converge for impulse excitation and shown graphically to be fairly small for quake excitations.

Chapter 6

ADAPTIVE LENGTH PENDULUM SMART TUNED MASS DAMPER PERFORMANCE IN THE PRESENCE OF STIFFNESS CHANGE

The preceding chapters focused on topics related to adaptive real time methods to *either* perform structural health monitoring or structural control. This final chapter, combines the themes of *both* structural health monitoring and structural control in an experimental study. The experiments implement the newly developed Adaptive Length Pendulum Smart Tuned Mass Damper (ALP-STMD) which was first introduced and developed by Nagarajaiah [92] and Nagarajaiah and Pasala [93]. The ALP-STMD employs a pendulum of variable length which can tune in real time to the parameters of the system using sensor feedback. The tuning action is made possible by applying a current to a shape memory alloy in a configuration capable of changing the effective length of the wire and mass assembly in real time.

6.1 Motivation

In Section 1.2.3, the benefits and limitations of different types of TMDs were discussed, particularly the Adaptive Passive Tuned Mass Dampers (APTMDs). Recalling that although APTMDs are capable of adaptive tuning to system parameters

based on mechanical and/or physical changes to their configuration, they do not benefit from the real time sensor feedback and actuation found in STMDs. The main motivation of this experimental study is to demonstrate that by using a shape memory alloy in an ALP configuration, an ALP-STMD attains an enhanced level of robust adaptivity with respect to traditional APTMDs. The enhanced merits of the ALP-STMD are displayed by performing structural control in the presence of stiffness change. Once a stiffness change in the structural system is detected, the ALP-STMD is retuned to the modified system parameters and successfully dissipates the base excitations. Significantly improved performance is illustrated for the stiffness modified system which undergoes the retuning adaptation when compared to the stiffness modified system without adaptive retuning.

6.2 Observer Error Formulation

An open loop observer formulation, similar to the formulation implemented by Nagarajaiah and Li [76], was used to adequately detect damage in real time. Since sensory data was observed at the second story degree of freedom, the observer formulation is sufficient to detect changes in first mode behavior. The sensory data was produced by a laser sensor. It is acknowledged that the open loop observer detection scheme focuses only on global changes in system parameters; however, for the demonstration of the ALP-STMD capabilities, the global detection is sufficient.

A block diagram of the open loop observer is illustrated in Fig. 6.1. The input

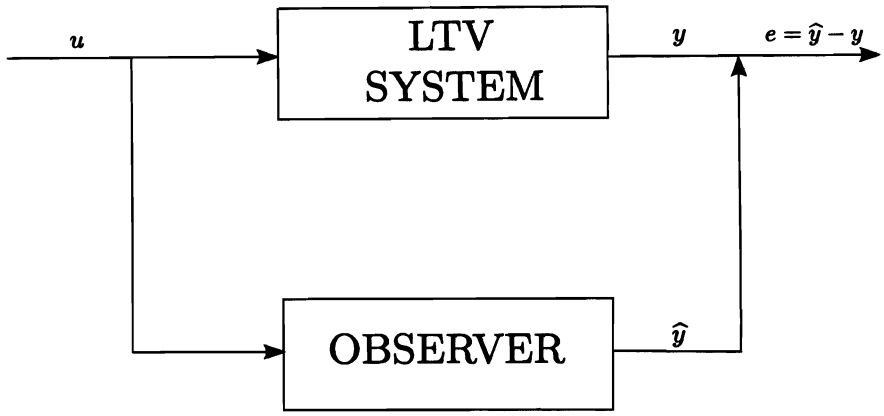

Figure 6.1 : Block Diagram for Open Loop Observer Error SHM

excitation is fed simultaneously to the plant and to the observer. The output of both the healthy observer and the plant are compared in real time and form a residual error signal, $e = \widehat{y} - y$. If the plant is modified in a time varying manner by a change in system stiffness and the model for the healthy observer is fairly accurate, then $e \neq 0$. If the plant remains unmodified in its nominal state, then the residual signal is zero, $e = 0$, for a system that is modeled perfectly, and close to zero for a system with bounded modeling errors.

The error function carefully monitors changes in the system. For the experiments performed in this study, if the error function increases to six times the nominal error bounds for a three second window of data, the frequency tracking controller proposed by Nagarajaiah and Pasala [93] is engaged. The effective length of the ALP-STMD is changed in a manner such that it matches the frequency of the dominant pulse in the response of the modified system. The tuned ALP-STMD is capable of absorbing

the energy of the response of the modified structure in real time based on the sensory feedback and the calculations of the observer.

6.3 Experimental Setup

A bench scale structural shear frame was selected for the experimental validations. The shear frame is similar to the laboratory specimen used in [65], but the differing dimensions of the floors and columns yield a slightly heavier and stiffer system. It is constructed of $1/8 \times 2$ in. aluminum columns and $1/2 \times 2$ in. steel floors assumed to be rigidly fixed by threaded screw joint connections in a 3:4 (floor:column) ratio. The system is excited at its base by a shaking table driven by a linear actuator controlled by dSPACE digital hardware and computer input. A laser displacement sensor is placed at the floor levels to capture the system response from base excitation. The laser sensor provides relatively noise free, high fidelity data that affords the application of the proposed feedforward observer based Structural Health Monitoring (SHM) algorithm. The ALP-STMD is placed at the second floor to have a significant impact on the first mode dynamics of the system.

The system is instrumented with SMAs in a crossed-braced, continuous configuration which allows the time varying stiffness change in the shear frame to be generated from an elongation/relaxation of the brace length. The unique, superelastic properties of the SMAs enable the experiments to be performed repetitively without any permanent deformation to the SMA brace. Fig. 6.2 displays the complete experimental

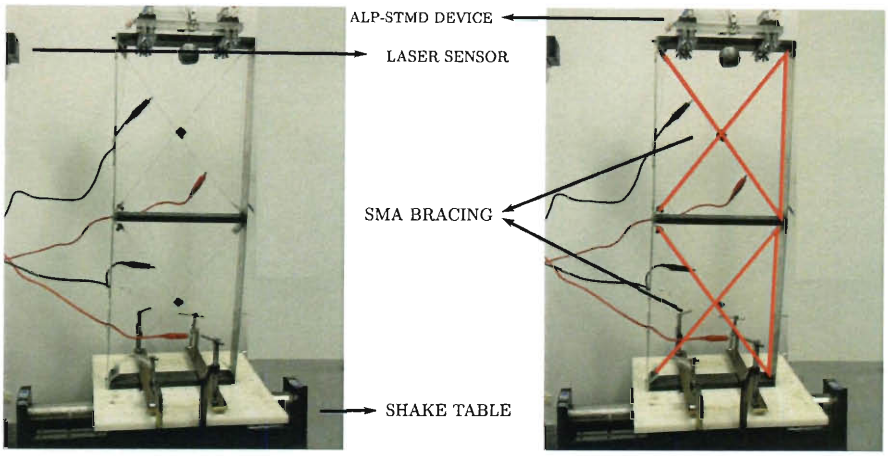

Figure 6.2 : Experimental Setup (left) and Experimental Setup with Braced Configuration Highlighted (right)

setup.

6.3.1 Device Overview

The original development of an ALP was demonstrated by Nagarajaiah [92] for a TMD which used a pulley system in combination with a rotary mechanical motor that could be controlled in real time. Nagarajaiah and Pasala [93] and Nagarajaiah *et al.* [94] later extended this idea to utilize the superelastic properties of the SMA wire and demonstrated its effectiveness in controlling first and second mode response for stationary, non-stationary, and impulse excitations. The pulley system developed by Nagarajaiah and Pasala [93] is composed of two rows of steel bearing, horizontal pulleys aligned in parallel that rest atop the second floor of the structure as shown in Fig. 6.3. The steel bearing, horizontal pulleys are secured using aluminum, conductive

holders which allow the SMA wire to coil back and forth eventually securing to an 8 *oz* mass at on end of the wire. Also shown in Fig. 6.3, the mass is suspended over a vertical pulley with a certain amount of overhang length. The ability to vary the overhang length strategically and with the use of feedback is what makes the ALP-STMD a unique device.

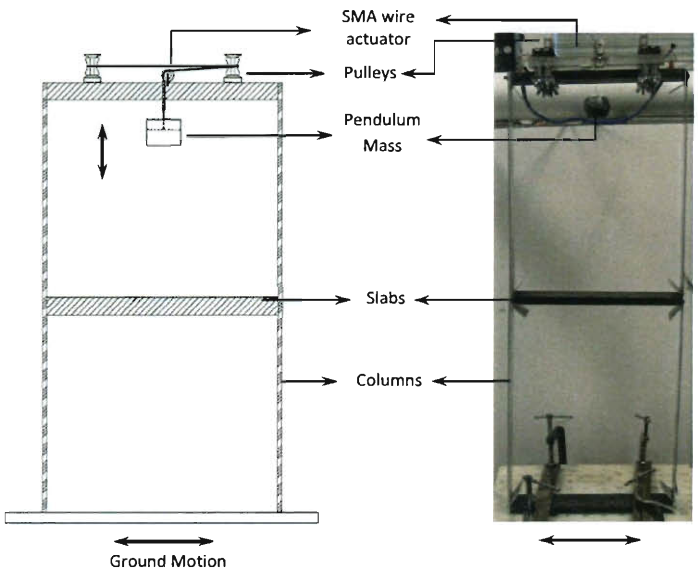

Figure 6.3 : ALP-STMD Device: Schematic (left) and Actual (right)

The ALP is made possible by the crystalline structure material transition of the SMA wire. This material transition occurs at a critical phase transformation temperature. By passing an electrical current through the SMA wire, the resistive nature of the material induces Joule heating which causes the temperature to rise. For this application, Nitinol (NiTi) SMA actuator wire with 0.010 mm diameter and a tran-

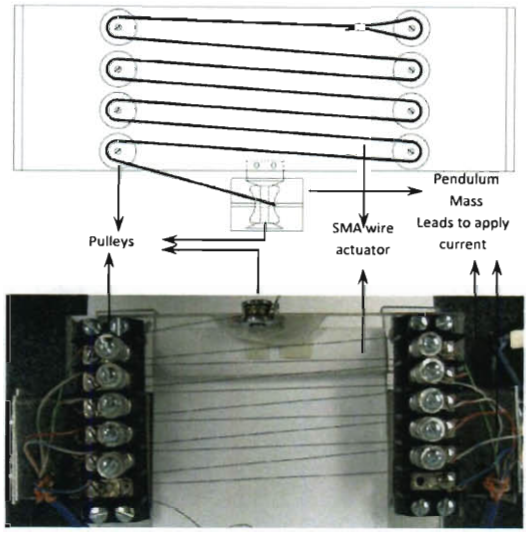

Figure 6.4 : Mechanism for Control of SMA Effective length

sition temperature of 90° C was used in both the pendulum device and floor braces. For the experiments, 0.80 A current was sufficient to raise the temperature of the SMA actuator beyond the transition temperature.

When the current is zero, Joule heating does not occur and the SMA is in a superelastic state in which it is elongated by the weight of the mass. Consequently, the ALP has its greatest overhang length in these conditions, and energy will be transfered to the pendulum mass for a base excited system. When the current is increased, Joule heating causes the temperature to rise in the SMA wire. Once the critical transformation temperature is exceeded, the crystalline structure changes and the SMA wire returns to its intrinsic, contracted shape reducing the overhang length of the pendulum mass. If the overhang length becomes zero, the ALP is not capable

of absorbing energy of a base excited system and may be considered as an added mass to the second floor.

A top view of the SMA pulley actuation device is shown in Fig. 6.4. This novel pulley configuration allows the user to vary the effective length of the pendulum by passing current and applying heat through discrete portions of the overall wire length. By changing the terminals through which the current is sent, different overhang lengths of the pendulum can be achieved. In general, the greater the portion of heated wire the greater the contraction of the overhang length.

6.3.2 Generating an Observer Model

Regarding system identification of the experimental setup, the nominal state of the structural system was defined to be the stiffened state where 1.5 A of current was infused into each floor's SMA bracing (recall Fig. 6.2). This level of current in the SMA wire causes the temperature of the wires to remain high and consequently the braces taught with tension. Using a sinesweep base excitation, the modes of the stiffened system are excited. Due to the objectives of the experimental study, special consideration is afforded to capturing first mode behavior. A transfer function, shown in Fig. 6.5, was produced describing the relationship between the response at the second floor and the input excitation.

Next, given the mass of the floors and natural frequencies of the nominal system and assuming standard physical assumptions when describing the dynamic motion of

a shear frame, the stiffness, mass, and damping matrices are realized. The physical assumptions mandate that stiffness is represented by assuming a banded matrix, $\mathbf{K}$ with units $\left(\frac{N}{m}\right)$, mass is signified by a diagonal mass matrix, $\mathbf{M}$ in (kg), and there exists a banded Rayleigh damping matrix, $\mathbf{C}^{damp}$ with units $\left(\frac{N-sec}{m}\right)$. The calculated matrices for the healthy model are listed below.

$$\mathbf{K} = \begin{bmatrix} 7056 & -3456 \\ -3456 & 3456 \end{bmatrix} \quad \mathbf{M} = \begin{bmatrix} 1.22 & 0 \\ 0 & 1.43 \end{bmatrix} \quad \mathbf{C}^{damp} = \begin{bmatrix} 39.85 & 4.62 \\ 4.62 & -4.62 \end{bmatrix} \tag{6.1}$$

assuming the forms:

$$\mathbf{K} = \begin{bmatrix} k_1 + k_2 & -k_2 \\ -k_2 & k_2 \end{bmatrix} \quad \mathbf{M} = \begin{bmatrix} m_1 & 0 \\ 0 & m_2 \end{bmatrix} \quad \mathbf{C}^{damp} = \begin{bmatrix} c_1 + c_2 & -c_2 \\ -c_2 & c_2 \end{bmatrix} \tag{6.2}$$

Once $\mathbf{M}$, $\mathbf{C}^{damp}$ and $\mathbf{K}$ are realized, the open loop observer can be constructed from the controllable canonical state space representation with output displacement observed at the second floor shown below in Eq. 3.

$$\begin{aligned} \dot{\widehat{\mathbf{x}}}_{4\times1}(t) &= \mathbf{A}_{4\times4}\widehat{\mathbf{x}}_{4\times1}(t) + \mathbf{B}_{4\times1}u(t) \\ \widehat{\mathbf{y}}_{1\times1}(t) &= \mathbf{C}_{1\times4}\widehat{\mathbf{x}}_{4\times1}(t) \end{aligned} \tag{3}$$

The observer estimate of the state variable, $\widehat{\mathbf{x}}_{4\times1}$, consists of a relative displacement vector for all degrees of freedom, $\widehat{\mathbf{x}}_{2\times1}$, stacked on top of a relative velocity vector for all degrees of freedom, $\dot{\widehat{\mathbf{x}}}_{2\times1}$. $u(t)$ is the input acceleration and $\mathbf{A}$, $\mathbf{B}$, $\mathbf{C}$, and are

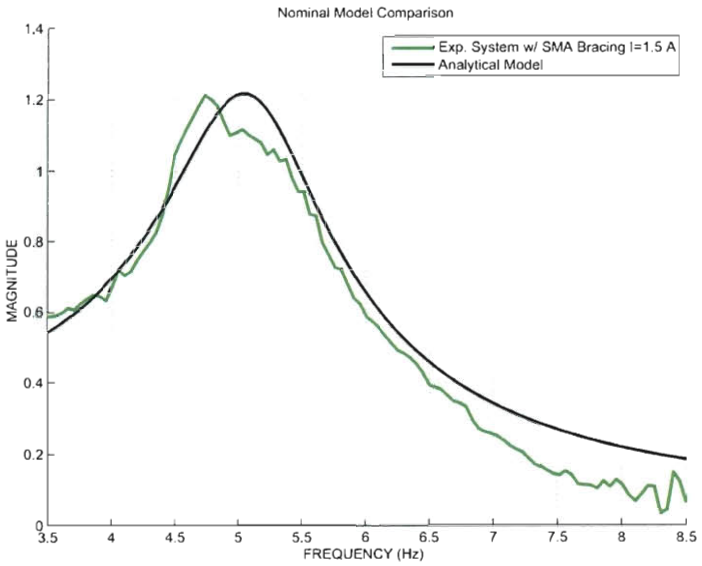

Figure 6.5 : Transfer Function Comparison of Nominal Experimental System and Nominal Analytical Model

state space matrices defined as follows:

$$\mathbf{A}_{4\times4} = \begin{bmatrix} \mathbf{0}_{2\times2} & \mathbf{I}_{2\times2} \\ -\mathbf{M}_{2\times2}^{-1}\mathbf{K}_{2\times2} & -\mathbf{M}_{2\times2}^{-1}\mathbf{C}_{2\times2}^{damp} \end{bmatrix}$$

$$\mathbf{B}_{4\times1} = \begin{bmatrix} \mathbf{0}_{2\times1} \\ \mathbf{\Gamma}_{2\times1} \end{bmatrix}$$

and

$$\mathbf{C}_{1\times4} = \begin{bmatrix} 0 & 1 & 0 & 0 \end{bmatrix}$$

where $\mathbf{\Gamma}$ is a vector of unity influence coefficients.

The analytical model generated from the calculated matrices is straightforward and compares sufficiently well given the objectives of the experimental study. Fig. 6.5

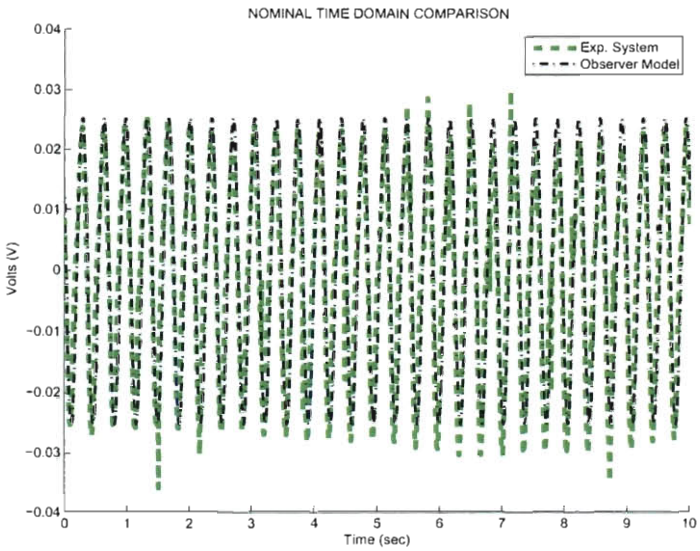

Figure 6.6 : Time Domain Comparison for 2^{nd} Floor Response of Nominal Experimental System and Nominal Observer Model

illustrates the comparison of the nominal experimental transfer function and the proposed nominal analytical model.

Since the nominal observer will be used in the time domain, a time history comparison is shown in Fig. 6.6. It is worth noting that although the model matches the phase behavior of the experimental output very well, there is some minor discrepancy in the approximation of magnitude. System noise and/or irregularities are most likely the cause of this phenomena; however, as long as the magnitude of the approximation error is small relative to the overall response, it is acceptable.

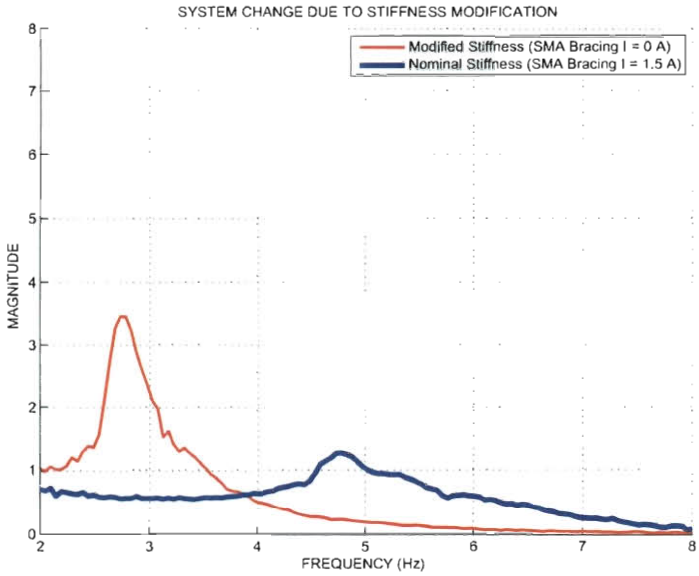

Figure 6.7 : Effect of Stiffness Modification on System Transfer Function

6.3.3 Using SMA to Produce Stiffness Change

When the current in the SMA bracing is set to 0 A, the SMA braces are relaxed and they are no longer taught with tension (recall Fig. 6.2). This is considered the modified state because each floor has a changed stiffness. When stiffness is changed in the floors simultaneously, the properties of the structure will change. The frame is susceptible to larger displacements pending the input excitation. The change in system behavior is illustrated by the transfer functions from input to 2^{nd} story displacement for both the nominal and modified state shown in Fig. 6.7.

The transfer functions produced in Fig. 6.7 were produced from chirp sine base excitation tests. The complete two story system with the ALP-STMD not engaged

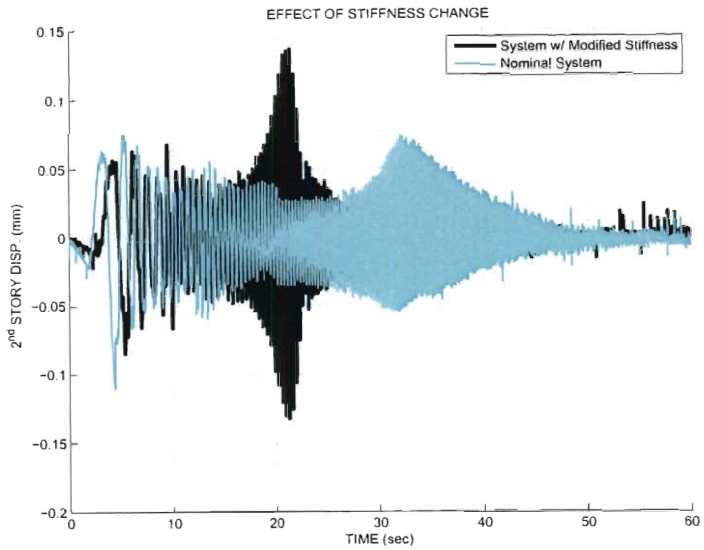

Figure 6.8 : Effect of Stiffness Modification: Time Domain Comparison

was excited with a nonstationary sinesweep input. The second floor displacement was captured by the laser sensor and the aforementioned transfer functions were produced for the nominal and modified systems. The time history displacements for the second floor are shown in Fig. 6.8 for the same chirp sine input. It is evident that the system experiences a resonant response at different frequencies for the nominal and modified systems.

The stiffness modified transfer function has a peak first mode response at 2.78 Hz and has a sharper peak in comparison to the nominal stiffness transfer function. The nominal system has a very broad, flattened first mode peak at 4.78 Hz. It is clear from the transfer function comparison data, that it is desirable to ensure that the structure remains in its nominal state for a first mode excitation. If the system is

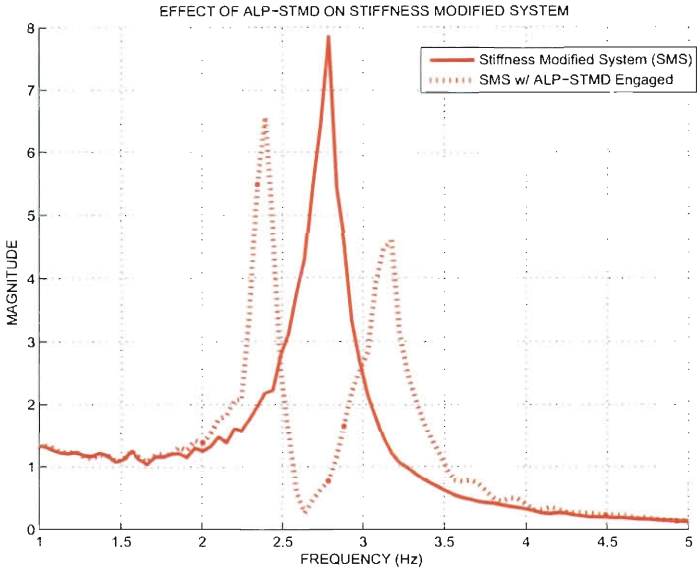

Figure 6.9 : Effect of ALP-STMD on Stiffness Modified System: FRF Comparison

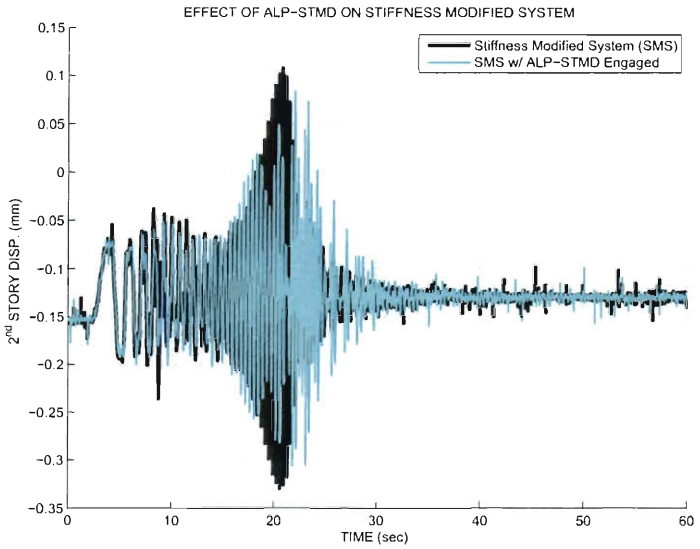

Figure 6.10 : Effect of ALP-STMD on Stiffness Modified System: Time Domain Comparison

modified, it is the primary objective of the ALP-STMD to ensure the system response is reduced.

To illustrate the effect of the ALP-STMD on the stiffness modified system Fig. 6.9 shows the transfer function from input to 2^{nd} story displacement of both the modified system and the modified system with the ALP-STMD engaged. The figure was produced from data captured by chirp sine input excitation tests which are shown in Fig. 6.10. In Fig. 6.9, it is apparent that the ALP-STMD successfully distributes the total peak energy of the damaged system into two separate peaks over the the frequency range of excitation. These two off-tuned peaks are still less significant in magnitude than the peak frequency response of the stiffness modified system without ALP-STMD compensation.

6.4 Experimental Results for Real Time Stiffness Modification Tests

The experimental procedure that validates the proposed control algorithm and demonstrates the benefits of implementing the ALP-STMD was straightforward. The structural system was excited with a stationary sinusoidal base excitation oscillating at 2.75 Hz. At time $t = 15$ sec, the SMA brace current was shut off/set to 0 A to induce a stiffness modification in the system. In real time, the system was being monitored by the error function introduced in Section 2 which utilized the analytical model presented in Section 3.2. When the error function threshold was exceeded, the ALP-

STMD was engaged in real time and tuned to the dominant frequency present in the response using the STFT control algorithm presented by Nagarajaiah and Pasala [93]. The error function results are displayed for 60 sec of experimental data in Fig. 6.11.

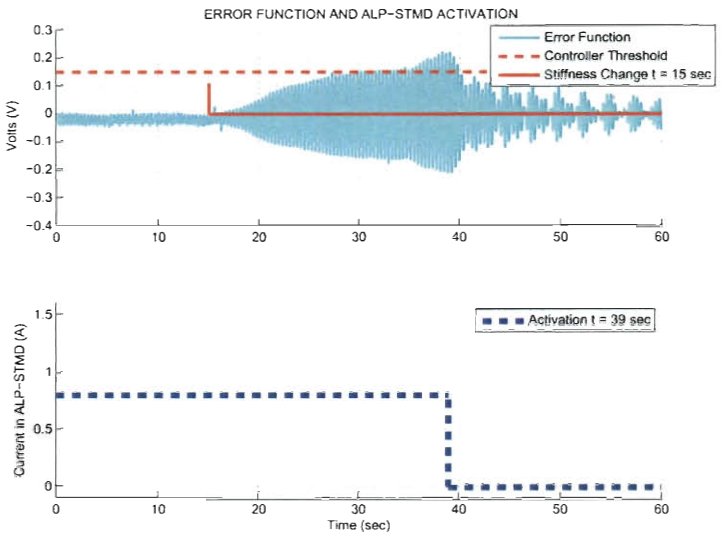

Figure 6.11 : Error and Ensuing ALP-STMD Activation in the Presence of Stiffness Change

From time $0-15$ seconds the error function oscillated between a nominal max/min value close to zero that is associated with the nominal system. After time 15 seconds the system passed through a short transition zone in which heat was dissipating from the SMA bracing and the tension decreased. After the SMA bracing had cooled to its modified stiffness state, the entire structural system experienced larger displacements which was evidenced by the error function exceeding the controller threshold of 0.15 V after 32 seconds. After the threshold had been exceeded for the duration of the proposed window length of 3 seconds, the ALP-STMD frequency tracking algorithm

was activated.

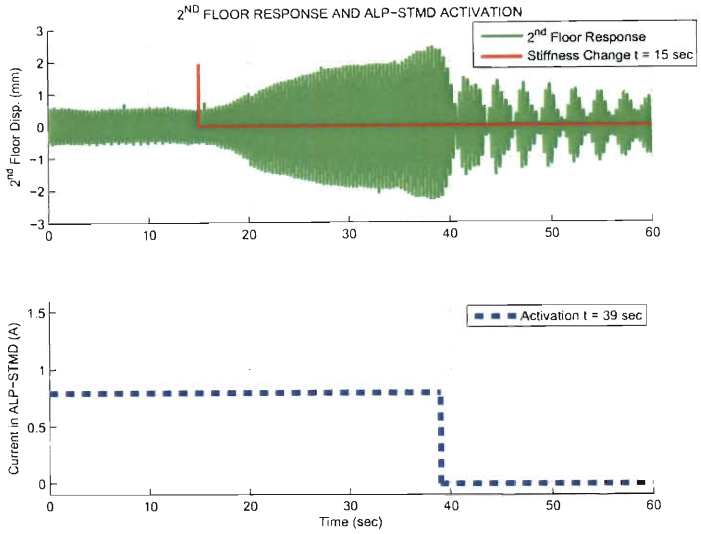

Figure 6.12 : Effect of ALP-STMD on 2^{nd} Floor Displacement

In Fig. 6.12 and Fig. 6.13 respectively, the 2^{nd} and 1^{st} floor displacement time history responses are displayed in the presence of the stiffness modification and ALP-STMD activation. The frequency tracking was triggered at 35 seconds. After 3 seconds of tracking the dominant vibration frequency, the current in the ALP-STMD device was set to 0 A at $\approx$ 39 seconds to match the optimal length required to match the dominant frequency of vibration. The response at both floors was reduced immediately as evident in the Fig. 6.11 to Fig. 6.13. The 2nd and 1st floor displacement was reduced by as much as 57 % and 47 % respectively. It is important to note that these reductions were still achieved despite a coarse tuning of the ALP-STMD. A finer tuned system would reduce the off frequency 'beating' that is evident in Fig. 6.12 and

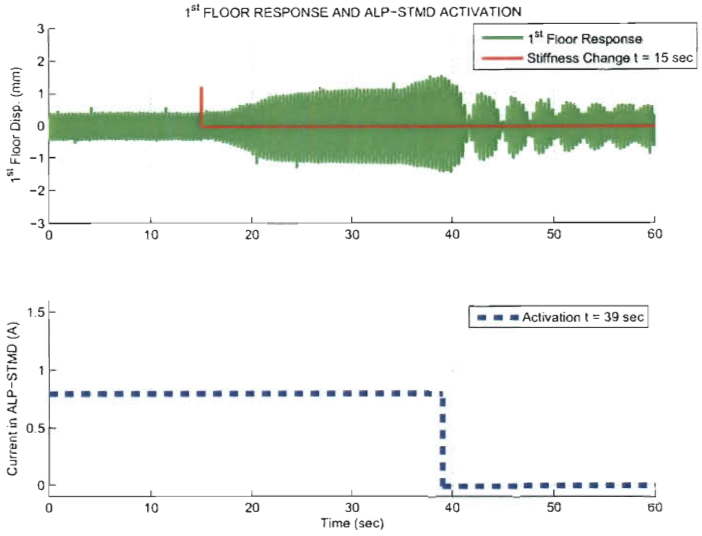

Figure 6.13 : Effect of ALP-STMD on 1^{st} Floor Displacement

Fig. 6.13.

Finally, in Fig. 6.14 open and closed loop response for each floor are shown. It is evident from the figure Fig. 6.14 that despite stiffness modification due to the SMA bracing in each floor, the structural frame experiences significantly reduced response due to deployment of the ALP-STMD when compared to a system without ALP-STMD and such adaptive benefits.

6.5 Summary

A proof of concept experimental study involving real time structural health monitoring and adaptive tuning of the newly developed ALP-STMD was undertaken. It was validated that an open loop observer formulation (1) was capable of monitoring the

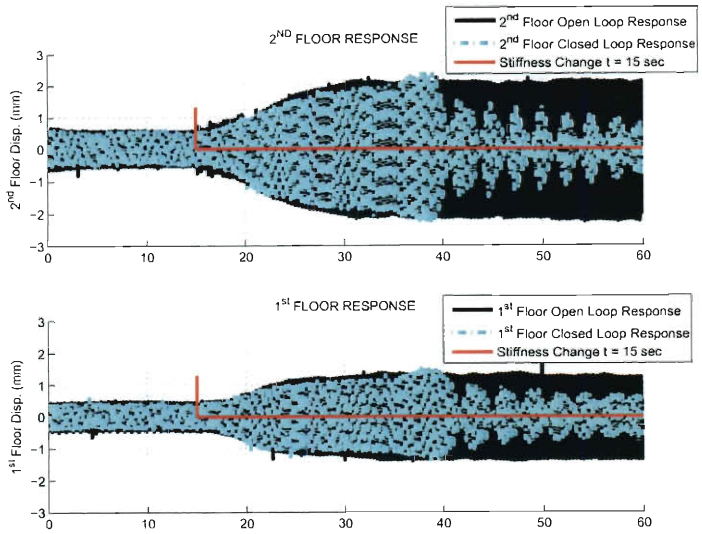

Figure 6.14 : Open Loop and Closed Loop Comparison Plots for Each Floor

structural integrity of the bench scale specimen in real time and (2) could be incorporated as an activation trigger for semi-active structural control of the ALP-STMD. A stiffness change was induced in real time to the system by regulating current flow to SMA brace wires in the first and second floor of the structure. This stiffness modification scenario utilized the superelastic nature of SMA materials so that the test could be performed repetitively without any yielding of the material. In the presence of stiffness change and base excitation, the ALP-STMD showed favorable performance with respect to magnitude of the 2^{nd} and 1^{st} floor response reduction.

Chapter 7

CONCLUSION

This body of work carried the general theme of approaching the structural health monitoring and control problem as being one of enhancing structural system intelligence. Computational strategies that mimic human learning and attempt to replicate human response to sensory feedback are implemented through the application of a variety of smart materials. This dissertation proposes several new methods which promote adaptive, intelligent decision making by smart structural systems. Four significant contributions can be found in this thesis study. The first method employs a RBFN for robust control in the presence of piezoelectric sensor failure and actuation. The second method augments an open loop observer formulation with a static RBF network to detect and isolate system faults which were experimentally produced in real time by the SAIVS device. The third algorithm utilizes an adaptive RBFN once more to effectively linearize the nonlinear actuator dynamics of an MR damper thereby improving control of the semiactive device. Lastly, an open loop observer is implemented experimentally to both detect damage and act as a trigger for control of the newly developed ALP-STMD.

7.1 Concluding Remarks

The adaptive fault tolerant neuro-controller is validated on two models. The first system being a standard shear frame model with collocated sensing and actuation. The Neuro-H_∞ controller has better performance for disturbance rejection than the baseline H_∞ controller with respect to the five selected performance measures. When the sensors are completely healthy the Neuro-H_∞ controller is capable of bettering performance up to a maximum of approximately 37% when compared to the baseline H_∞ controller. When the sensors are damaged, the maximum improvement seen when implementing the Neuro-H_∞ control formulation is approximately 41%. The second system, a bench scale laboratory specimen, possessed a unique placement of piezoelectric sensors and small amount of noise in the input/output voltage. It was fitted with a low order system identification model that was well suited for experimental implementation. In all healthy and sensor failure cases for the laboratory system, the Neuro-H_∞ controller has better first mode disturbance rejection than a baseline H_∞ controller with respect to energy dissipation (PSD plots) and damping ratio. The Neuro-H_∞ controller was responsible for upwards of 20% improvement in first mode damping ratio while only moderate improvements were made in damping ratio of the second mode.

A novel health monitoring formulation capable of isolating coupled and uncoupled stiffness variation, damage and recovery, has been proposed. It is also illustrated that for the generalized training procedure described in this study, coupled and uncoupled

damage cases could be sufficiently detected and isolated for systems with up to ten degrees of freedom. Some of the merits of the formulation include real time detection and a generalized offline training scheme. The algorithm has been validated for systems experiencing damage during earthquake excitations, larger systems with non-collocated input and output with damage in only a few members, and experimental data from stiffness variation tests in the presence of harmonic excitation performed using the SAIVS device at Rice University. The developed method has significant potential as evident from the numerical and experimental validations.

A neural network formulation is developed to perform real time, dynamic inversion for semiactive control of an MR damper actuator. The MR damper, which was modeled after a laboratory specimen, has a voltage to force relationship that is characterized by Bouc-Wen hysteresis and is not readily invertible. This online adaptive inverse technique essentially linearizes the actuator dynamics of the MR damper enabling the implementation of an H_2/LQR optimal control force. It does this by using a RBFN to minimize the error between the desired optimal control force, which is designed assuming linear actuation, and the real MR damper actuator control force that is imparted to the system. Without the use of the linearization technique, H_2/LQR control theory would not be applicable. The method is validated by simulations based on a scaled two story model that was fabricated and tested in the Rice laboratory with the MR damper acting as a base isolator. The control performance of the adaptive RBFN Dynamic Inversion method is a viable technique for

semiactive control as evidenced from the comparisons to passive-off and passive-on control. Significant performance improvements were seen in the second floor with respect to RMS displacements/accelerations and peak displacement/accelerations.

A proof of concept experimental study involving real time structural health monitoring and adaptive tuning was performed on the ALP-STMD, a recently developed device at Rice University. It is validated that an open loop observer formulation (1) is capable of monitoring the structural integrity of a bench scale specimen in real time and (2) could be incorporated as an activation trigger for semi-active structural control of the ALP-STMD. Damage was induced in real time to the system by regulating flow of current to SMA brace wires in the first and second floor of the structure. This damage scenario utilizes the superelastic nature of SMA materials so that the tests could be performed repetitively without any yielding of the material. In the presence of stiffness loss and base excitation, the ALP-STMD showed favorable reductions in magnitude of up to 57% and 47% in the 2^{nd} and 1^{st} floor repectively.

7.2 Future Research

Future research directions for methods developed in this dissertation are addressed by the following bulleted list:

- Although the adaptive control simulation results are favorable, the performance of the baseline controller and, consequently, the augmented neuro-controller relies heavily on the fidelity of the model. For standard, shear frame type build-

ings this is straightforward; however, for piezoelectric sensors and actuators, two items need improved understanding in order to attain better mathematical models for control design. The first is the issue of the piezoelectric sensor not being collocated with the input. This non-collocated arrangement is a challenging research direction because the effect of piezoelectric strain actuation on the lateral motion of the floors has not been adequately mathematically characterized. A combination of models based on physics and advanced system identification techniques would benefit future research greatly. Secondly, since the piezoelectric sensor/actuator is attached to the structure, the input voltage to output strain relationship is highly dependent on the quality of bonding. There is little research in this arena, and the bonding issue could potentially affect full scale application with nonmetallic surfaces.

- The proposed RBFN augmented observer framework adequately performed FDI for a variety of different systems. Its training procedure is quite general, and it showed promise for higher degree of freedom systems (up to ten DOFs). Being able to quantify the extent of damage present in addition to FDI would make it a complete method. This is challenging because damage quantification requires a greater number of hidden layer neurons, thus increasing computational time. Future research directions ideas may include applications of high power, high speed computing to perform not only FDI, but damage quantification.

- The adaptive RBFN Dynamic Inversion method enables enhanced control per-

formance for semiactive systems. Other applications could include modeling the inverse of the nonlinear relationship of the SMA behavior in the ALP-STMD device. The inverse model describing the change in SMA length to electrical current input could be used to improve control performance of the ALP-STMD device in real time. An analogous technique to Ch. 5 could be used where a desired optimal length for the ALP-STMD could be calculated from linear control theory, and with the use of the RBFN linearization technique, the proper current could be injected into the wire such that the optimal length is achieved. This would allow for more fine tuned, smoothly varying control of the SMA overhang length than the existing discrete/effective length pulley system. The RBFN-DI method has performed well in the simulation study in Ch. 5 and is ready for experimental verification for a variety of nonlinear smart materials, or materials whose input-output relationships are not readily invertible.

- The proof of concept study is the first validation of its kind for ALP-STMD systems. Consequently, there are many future research directions of interest. An existing limitation of the ALP-STMD can be found in the adequate tuning of the SMA wire. In the experiments presented, reductions were observed after some time only when the proper tuning frequency was determined. This could potentially be a handicap for applications in which the frequency of system response varies rapidly. Another area for development is in reducing the power and current consumption of the ALP-STMD device. Current of 0.8 A was

used in the study. This current requirement was feasible for such a small scale system; however, at this ratio current values may become too large for full scale implementation of the ALP-STMD. One possible remedy for the large current requirement can be found in utilizing applications of power electronics to improve the existing current amplification capabilities of the device setup.

Bibliography

[1] J. C. Doyle, "Synthesis of robust controllers and filters," in *Proc. IEEE Conf. Decision Contr.*, (San Antonio, TX), pp. 109–114, 1983.

[2] R. E. Skelton, T. Iwasaka, and K. Grigoriadis, *A Unified Algebraic Approach to Linear Control Design.* Bristol, PA: Taylor & Francis, 1998.

[3] S. F. Masri, A. G. Chassiakos, and T. K. Caughey, "Identification of nonlinear dynamic systems using neural networks," *J. Appl. Mech.*, vol. 60, no. 1, pp. 123–34, 1993.

[4] J. Ghaboussi and A. Joghataie, "Identification of nonlinear dynamic systems using neural networks," *J. Appl. Mech.*, vol. 121, no. 4, pp. 555–67, 1995.

[5] S. Narasimhan, S. Suresh, S. Sundararajan, and S. Nagarajaiah, "On-line learning failure-tolerant neural-aided controller for earthquake excited structures," *Journal of Engineering Mechanics*, vol. 134, no. 3, pp. 258–68, 2008.

[6] S. Suresh, S. Narasimhan, S. Nagarajaiah, and S. Sundararajan, "Fault-tolerant adaptive control of nonlinear base-isolated buildings using emran," *Engineering Structures*, vol. 32, no. 8, pp. 2477–87, 2010.

[7] L. Wang, "Positive position feedback based vibration attenuation for a flexible aerospace structure using multiple piezoelectric actuators," in *Proceedings of the IEEE 22nd Digital Avionics Systems Conference*, vol. 2, pp. 7.C.1–1 – 7.C.1–10, 2003.

[8] G. Song, V. Sethi, and H. N. Li., "Vibration control of civil structures using piezoceramic smart materials: a review," *Engineering Structures*, vol. 28, no. 11, pp. 1513–1524, 2006.

[9] T. Kamada, T. Fujita, T. Hatayama, T. Arikabe, N. Murai, and S. Aizawa, "Active vibration control of frame structures with smart structures using piezoelectric actuators (vibration control by control of bending moments of columns)," *Smart Materials and Structures*, vol. 6, no. 4, pp. 448–456, 1997.

[10] K. Duerig and T. Melton, "Designing with the shape memory effect," in *Proceedings of MRS International Meeting on Advanced Materials*, (Tokyo, Japan), pp. 581–597, 1989.

[11] J. Humbeeck and S. Kustov, "Active and passive damping of noise and vibrations through shape memory alloys: Applications and mechanisms," *Smart Materials and Structures*, vol. 14, no. 5, pp. S171–S185, 2005.

[12] B. F. S. Jr, J. D. Carlson, M. K. Sain, and G. Yang, "On the current status of magnetorheological dampers: seismic protection of full-scale structures," in

Proceedings of 1997 American Control Conference, (Albuquerque, NM), pp. 458–62, 1997.

[13] B. F. Spencer, S. J. Dyke, M. K. Sain, and J. D. Carlson, "Phenomenological model for magnetorheological dampers," *Journal of Engineering Mechanics*, vol. 123, no. 3, pp. 230–8, 1997.

[14] S. J. Dyke, B. F. Spencer, M. K. Sain, and J. D. Carlson, "Modeling and control of magnetorheological dampers for seismic response reduction," *Smart Materials and Structures*, vol. 5, no. 5, pp. 565–75, 1996.

[15] S. J. Dyke, B. F. Spencer, M. K. Sain, and J. D. Carlson, "On the efficacy of magnetorheological dampers for seismic response reduction," in *Proceedings of 1997 ASME Design Engineering Technical Conferences*, (Sacramento, CA), 1997.

[16] S. J. Dyke, B. F. Spencer, M. K. Sain, and J. D. Carlson, "An experimental study of magnetorheological dampers for seismic hazard mitigation," in *Proceedings of Structures Congress XV*, (Portland, OR), pp. 1358–62, 1997.

[17] W. S. L. (Ed.), *The Control Handbook*. CRC-IEEE Press, 1996.

[18] B. F. S. Jr and S. Nagarajaiah, "State of the art of structural control," *Journal of Structural Engineering*, vol. 129, no. 7, pp. 845–856, 2003.

[19] T. T. Soong, A. M. Reinhorn, Y. P. Wang, and R. C. Lin, "Full-scale imple-

mentation of active control. I: Design and simulation," *Journal of Structural Engineering*, vol. 117, no. 11, pp. 3516–36, 1991.

[20] T. T. Soong and M. C. Constantinou, *Passive and Active Structural Vibration Control in Civil Engineering.* New York: Springer, 1994.

[21] T. T. Soong, *Active Structural Control: Theory and Practice.* New York: Longman, 1990.

[22] T. T. Soong, S. F. Masri, and G. W. Housner, "An overview of active structural control under seismic loads," *Earthquake Spectra*, vol. 7, no. 3, pp. 483–505, 1991.

[23] T. T. Soong, Y. Fujino, and B. F. S. Jr, "Structural control: basic concepts and applications," in *Proceedings of Structures Congress XIV*, (Chicago, IL), pp. 1277–87, 1996.

[24] R. I. Skinner, W. H. Robinson, and G. H. McVerry, *An Introduction to Seismic Isolation.* Chichester: Wiley, 1993.

[25] M. D. Symans and M. C. Constantinou, "Semi-active control systems for seismic protection of structures: A state-of-the-art review," *Eng. Struct.*, vol. 21, no. 6, pp. 469–487, 1999.

[26] B. F. S. Jr. and M. K. Sain, "Controlling buildings: A new frontier in feedback," *IEEE Control Syst. Mag.*, vol. 17, no. 6, pp. 19–35, 1997.

[27] B. F. S. Jr, "Civil engineering applications of smart damping technology," in *Proc., 5th Int. Conf. on Vibration Engineering*, (Nanjing, China), pp. 771–782, 2002.

[28] D. Hrovat, P. Barak, and M. Rabins, "Semi-active versus passive or active tuned mass dampers for structural control," *J. Eng. Mech.*, vol. 109, no. 3, pp. 691–705, 1983.

[29] S. Nagarajaiah and N. Varadarajan, "Novel semiactive variable stiffness tuned mass damper with real time tuning capability," in *Proc., 13th Engineering Mechanics Conf. - CD ROM*, (Reston, VA), 2000.

[30] N. Varadarajan and S. Nagarajaiah, "Wind response control of building with variable stiffness tuned mass damper using empirical mode decomposition/hilbert transform," *Journal of Engineering Mechanics*, vol. 130, no. 4, pp. 451–458, 2004.

[31] M. Abe and T. Igusa, "Semi-active dynamic vibration absorbers for controlling transient response," *J. Sound Vib.*, vol. 1998, no. 5, pp. 547–569, 1996.

[32] T. K. Caughey and M. P. Karyeaclis, "Stability of semi-active impact damper, Part I-Global behavior; Part II-Periodic solutions," *J. Appl. Mech.*, vol. 56, no. 4, pp. 926–940, 1989.

[33] J. Y. K. Lou, L. D. Lutes, and J. J. Li, "Active tuned liquid damper for structural

control," in *Proc., 1st World Conf. on Structural Control*, (Los Angeles, CA), pp. TP1: 70–79, 1994.

[34] S. Yalla, A. Kareem, and C. Kantor, "Semiactive tuned liquid dampers for vibration control of structures," *Eng. Struct.*, vol. 23, no. 11, pp. 1469–1479, 2001.

[35] N. P. Peterson, "Design of large scale tuned mass dampers," *Structural Control*, 1980.

[36] Y. Koike and K. Tanida, "Application of v-shaped hybrid mass damper to high rise buildings and verification of damper performance," in *Proceedings of the Structural Engineers World Congress*, (San Francisco, CA), pp. T198–4, 1998.

[37] A. Rytter, *Vibration Based Inspection of Civil Engineering Structures.* PhD thesis, Aalborg University, Denmark, 1993.

[38] B. Basu, S. Nagarajaiah, and A. Chakraborty, "Online identification of linear time-varying stiffness of structural systems by wavelet analysis," *International Journal of Structural Health Monitoring*, vol. 7, no. 1, pp. 21–36, 2008.

[39] S. Nagarajaiah and B. Basu, "Output only modal identification and structural damage detection using time frequency and wavelet techniques," *Earthquake Engineering and Engineering Vibration*, vol. 8, no. 4, pp. 583–605, 2009.

[40] P. Dharap, B. H. Koh, and S. Nagarajaiah, "Structural health monitoring using ARMarkov observers," *Journal of Intelligent Material Systems and Structures*,

vol. 17, no. 6, pp. 469–481, 2006.

[41] B. H. Koh, P. Dharap, S. Nagarajaiah, and M. Q. Phan, "Real-time structural damage monitoring by input error function," *Journal of American Institute of Aeronautics and Astronautics*, vol. 43, no. 8, pp. 1808–1814, 2005.

[42] B. Chen and S. Nagarajaiah, "H_-/H_∞ structural damage detection filter design using iterative lmi approach," *J. of Smart Materials and Structures*, vol. 17, no. 3, pp. 1–9, 2008.

[43] B. Chen and S. Nagarajaiah, "Linear matrix inequality based robust fault detection and isolation using the eigenstructure assignment method," *Journal of Guidance, Control, and Dynamics*, vol. 30, no. 6, pp. 1831–35, 2007.

[44] B. Koh, S. Nagarajaiah, and M. Q. Phan, "Direct identification of structural damage through kronecker product method," *Journal of Mechanical Science and Technology*, vol. 22, no. 1, pp. 103–12, 2008.

[45] B. H. Koh, Z. Li, P. Dharap, S. Nagarajaiah, and M. Q. Phan, "Actuator failure detection through interaction matrix formulation," *Journal of Guidance, Control and Dynamics*, vol. 28, no. 5, pp. 895–901, 2005.

[46] Z. Li, B. H. Koh, and S. Nagarajaiah, "Detecting sensor failure via decoupled error function and inverse input-output model," *Journal of Engineering Mechanics*, vol. 133, no. 11, pp. 1222–1228, 2007.

[47] R. V. Beard, *Failure accommodation in linear system through selfreorganization.* PhD thesis, Massachussets Institute of Technology, Boston, MA, 1971.

[48] H. L. Jones, *Failure Detection in Linear Systems.* PhD thesis, Massachussets Institute of Technology, Boston, MA, 1973.

[49] S. J. Kranock, *Real Time Structural Damage Detection using Model-based Observers.* PhD thesis, University of Colorado, Boulder, CO, 2000.

[50] S. Liberatore, *Analytical Redundancy, Fault Detection and Health Monitoring for Structures.* PhD thesis, University of California Los Angeles, Los Angeles, CA, 2002.

[51] S. Seibold and K. Weinert, "A time domain method for the localization of cracks in rotors," *Journal of Sound and Vibration*, vol. 195, no. 1, pp. 57–73, 1996.

[52] S. Seibold, "Identification of physical parameters using and instrumental variable technique," *Mechanical Systems and Signal Processing*, vol. 11, no. 3, pp. 425–39, 1997.

[53] M. Q. Feng and E. Y. Bahng, "Damage assessment of jacketed rc columns using vibration tests," *J. of Structural Engineering*, vol. 125, no. 3, pp. 265–71, 1999.

[54] C. Zhang, M. I. Friswell, and M. Imregun, "Structural damage detection using independent component analysis," *Structural Health Monitoring*, vol. 3, no. 1, pp. 69–83, 2004.

[55] J. L. Zapico, K. Worden, and F. J. Molina, "Vibration based damage assessment in steal frames using neural networks," *Smart Materials and Structures*, vol. 10, no. 3, pp. 553–559, 2001.

[56] F. Yakuwa, S. Satoh, and Y. Dote, "Combination of radial basis function (rbf) and time delayed neural networks (tdnn) for fault diagnosis of automobile transmission gears using general parameter learning and adaptation," in *Proceedings of the IEEE International Conference on Systems, Man and Cybernetics*, vol. 2, pp. 1457–62, 2003.

[57] S. Suresh, S. N. Omkar, R. Ganguli, and V. Mani, "Identification of crack location and depth in a cantilever beam using modular neural network approach," *Smart Materials and Structures*, vol. 13, no. 4, pp. 907–15, 2004.

[58] R. R. K. Reddy and R. Ganguli, "Structural damage detection in a helicopter rotor blade using radial basis function neural networks," *Smart Materials and Structures*, vol. 12, no. 2, pp. 232–31, 2003.

[59] J. Platt, "A resource allocating network for function interpolation," *Neural Computation*, vol. 3, no. 2, pp. 213–25, 1991.

[60] V. Kadirkamanathan and M. Niranjan, "A function estimation approach to sequential learning with neural network," *Neural Computation*, vol. 5, no. 6, pp. 954–75, 1993.

[61] M. Powell, "Radial basis function for multivariable interpolation: A review," in *Clarendon Press Institute Of Mathematics and Its Applications Conference Series*, pp. 143–67, 1987.

[62] D. Broomhead and D. Lowe, "Radial basis functions, multivariable functional interpolation and adaptive networks," *Complex System*, vol. 2, pp. 321–55, 1988.

[63] J. Moody and C. J. Darken, "Fast learning in network of locally-tuned processing units," *Neural Computation*, vol. 1, pp. 281–94, 1989.

[64] K. Warwick, "A critique of neural networks for discrete-time linear control," *International Journal of Control*, vol. 61, no. 6, pp. 1253–64, 1995.

[65] M. Contreras, S. Nagarajaiah, and S. Narasimhan, "Fault tolerant neural aided controller for multi degree of freedom structures experiencing online sensor failure," *Advances in Science and Technology*, vol. 56, pp. 247–52, 2008.

[66] M. Contreras, S. Nagarajaiah, and S. Narasimhan, "Real time damage detection in buildings using filter based radial basis function network mapping," in *Proceedings ASCE Structural Engineering Institute*, vol. 341, (Austin, TX), pp. 121–130, 2009.

[67] H. Holland, *Adaptation in natural and artificial systems.* Ann Arbor, MI: University of Michigan Press, 1975.

[68] Y. W. Lu, N. Sundararajan, and P. Saratchandran, "A sequential learning scheme

for function approximation using minimal radial basis neural networks," *Neural Comput.*, vol. 9, no. 2, pp. 1–18, 1997.

[69] L. Yan, N. Sundararajan, and P. Saratchandran, "Analysis of minimal radial basis function network algorithm for real-time identification of nonlinear dynamic systems," in *IEEE Proc. on Control Theory and Applications*, vol. 147, pp. 476–84, 2000.

[70] L. Yan, N. Sundararajan, P. Saratchandran, and Z. Wang, "Robust neuro-h_∞ controller design for aircraft auto-landing," in *IEEE Transactions on Aerospace and Electronic Systems*, vol. 40, pp. 158–67, 2004.

[71] J. E. White, *Detection filter design by eigensystem assignment.* PhD thesis, The University of Texas at Austin, Austin, TX, 1985.

[72] M. A. Massoumnia, *A geometric approach to failure detection and identification in linear systems.* PhD thesis, Massachussets Institute of Technology, Boston, MA, 1986.

[73] R. K. Douglas, *Robust fault detection filter design.* PhD thesis, The University of Texas at Austin, Austin, TX, 1993.

[74] B. Chen and S. Nagarajaiah, "Structural damage detection using decentralized controller design method," *J. of Smart Structures and Systems*, vol. 4, no. 6, pp. 779–94, 2008.

[75] P. Dharap, *Real-Time Structural Damage Detection Using Interaction Matrix Formuation and Observers.* PhD thesis, Rice University, Houston, TX, 2006.

[76] S. Nagarajaiah and Z. Li, "Time segmented least squares identification of base isolated buildings," *Soil Dynamics and Earthquake Engineering Journal*, vol. 24, no. 8, pp. 577–86, 2004.

[77] P. M. Frank, "Fault diagnosis in dynamic systems using analytical and knowledge-based redundancy - a survey and some new results," *Automatica*, vol. 26, no. 3, pp. 459–74, 1990.

[78] T. M. Cover, "Geometrical and statistical properties of systems of linear inequalities with applications in pattern recognition," in *IEEE Transactions on Electronic Computers*, vol. EC-14, pp. 326–34, 1965.

[79] S. Nagarajaiah and D. Mate, "Semi-active control of continuously variable stiffness system," in *Proc. 2nd World Conf. Structural Control*, vol. 1, pp. 397–405, 1998.

[80] S. Narasimhan and S. Nagarajaiah, "A STFT semiactive controller for base isolated buildings with variable stiffness isolation systems," *Engineering Structures*, vol. 27, no. 4, pp. 514–23, 2005.

[81] S. Nagarajaiah and S. Saharabudhe, "Seismic response control of smart sliding isolated buildings using variable stiffness systems: An experimental and numer-

ical study," *Earthquake Engineering and Structural Dynamics*, vol. 35, no. 2, pp. 177–97, 2006.

[82] S. Sahasrabudhe, *Semi-active Control of Sliding Isolated Buildings and Bridges with Variable Stiffness and Damping Systems.* PhD thesis, Rice University, Houston, TX, 2002.

[83] J. Reiner, G. J. Balas, and W. L. Garrad, "Robust dynamic inversion for control of highly maneuverable aircraft," *Journal of Guidance, Control, and Dynamics*, vol. 18, no. 1, pp. 18–24, 1995.

[84] R. J. Adams and S. S. Banda, "Robust flight control design using dynamic inversion and structured singular value synthesis," *IEEE Transactions on Control Systems Technology*, vol. 1, no. 18, pp. 80–92, 1993.

[85] G. Looye and H. D. Joos, "Design of robust dynamic inversion control laws using multiobjective optimization," in *AIAA Guidance, Navigation, and Control Conference and Exhibition*, (Montreal Canada), 2001.

[86] D. Enns, D. Bugajski, R. Hendrick, and G. Stein, "Dynamic inversion: An evolving methodology for flight control design," *International Journal of Control*, vol. 59, no. 1, pp. 71–91, 1994.

[87] D. Ito, D. Ward, and J. Valasek, "Robust dynamic inversion controller design and analysis for the x-38," in *AIAA Guidance, Navigation, and Control Conference and Exhibition*, (Montreal Canada), 2001.

[88] S. F. Ali and A. Ramaswamy, "Optimal dynamic inversion-based semi-active control of benchmark bridge using mr dampers," *J. Structural Control and Health Monitoring*, vol. 16, no. 5, pp. 564–85, 2009.

[89] S. F. Ali and R. Padhi, "Active vibration suppression of non-linear beams using optimal dynamic inversion," *Journal of Systems and Control Engineering*, vol. 223, no. 5, pp. 657–72, 2009.

[90] S. Sahasrabudhe and S. Nagarajaiah, "Semi-active control of sliding isolated bridges using mr dampers: an experimental and numerical study," *Earthquake Engineering and Structural Dynamics*, vol. 34, pp. 965–83, 2005.

[91] S. Sahasrabudhe and S. Nagarajaiah, "Experimental study of sliding base-isolated buildings with magnetorheological dampers in near-fault earthquakes," *Journal of Structural Engineering*, vol. 131, no. 7, pp. 1025–34, 2005.

[92] S. Nagarajaiah, "Adaptive passive, semiactive, smart tuned mass dampers: Identification and control using empirical mode decomposition, hilbert transform, and short-term fourier transform," *Structural Control and Health Monitoring*, vol. 16, no. 7-8, pp. 800–41, 2009.

[93] S. Nagarajaiah and D. T. R. Pasala, "Adaptive length pendulum dampers," in *Proc. ASCE Structures Congress*, vol. CD-ROM, 2010.

[94] S. Nagarajaiah, D. T. R. Pasala, and C. Huang, "Smart tmd: Adaptive length

pendulum damper," in *Proc. 5th World Conference on Structural Control and Monitoring*, 2010.